A Study of the Reaction $e^+e^-\rightarrow\mu^+\mu^-$ Around the Z^0 Pole

Christine Jane Beeston
Magdalen College, Oxford

A thesis submitted for the degree of Doctor of Philosophy
at the University of Oxford

4th August, 1992

A Study of the Reaction $e^+e^-\to\mu^+\mu^-$ Around the Z^0 Pole

Christine Jane Beeston
Magdalen College, Oxford

Submitted for the degree of Doctor of Philosophy
at the University of Oxford
4th August, 1992

ABSTRACT

This thesis contains an analysis of the reaction $e^+e^-\to\mu^+\mu^-$ at centre of mass energies of between 88 and 95GeV, using data taken with the DELPHI detector between April 1990 and June 1991. Firstly, the theory behind this reaction is introduced, and the extraction of electroweak parameters from experimental measurements is briefly described. The DELPHI detector is then described, and a trigger algorithm written for the barrel muon chambers of DELPHI is discussed.

After this introduction, the choice of selection criteria for $\mu^+\mu^-$events, and the calculation of backgrounds and efficiencies is described. The events selected are then used to calculate values for the cross section σ_μ, forward-backward asymmetry A_{FB}, and cross section as a function of $\cos\theta$, $\Delta\sigma/\Delta\cos\theta$.

Finally, fits to the σ_μ, A_{FB} and $\Delta\sigma/\Delta\cos\theta$ results are performed, assuming lepton universality. From a fit to the cross section measurements alone, a value of the leptonic width Γ_l of $(84.22\pm0.69(stat)\pm0.56(syst))$MeV is extracted. A combined fit to the cross section and asymmetry results yields values for the squares of the leptonic vector and axial vector couplings of $\bar{v}_l^2 = (0.0017\pm0.0009(stat)\pm0.0001(syst))$ and $\bar{a}_l^2 = (0.2517\pm0.0023(stat)\pm0.0016(syst))$, or equivalently, $\rho_{eff} = (1.007\pm 0.011\ (stat+syst))$ and $\sin^2\theta_W{}^{eff} = (0.229\pm0.009\ (stat+syst))$. Using the results of other experiments to determine the sign of $\bar{v}_l$, the coupling constants are found to be $\bar{v}_l = (-0.042^{+0.014}_{-0.010}(stat)\pm0.001(syst))$ $\bar{a}_l = (-0.5017\pm0.0023(stat)\pm0.0016(syst))$.

The $\Delta\sigma/\Delta\cos\theta$ measurements are observed to agree well with the predicted angular distribution of $\mu^+\mu^-$events, and fits to the data give values for the vector and axial vector coupling constants consistent with the results from the combined fit to the cross sections and asymmetries.

All of the results obtained are consistent with the predictions of the Minimal Standard Model, and assuming that this model is valid, they restrict the mass of the top quark to be between 50 and 310 GeV, at 90% confidence.

ACKNOWLEDGEMENTS

At last it's all over and I can write the acknowledgements. First thanks to the Oxford DELPHI group, in particular to my supervisors Peter Renton, for his continual interest and consistently good advice, and Louis Lyons, for his kindness and for many helpful discussions. I have also worked closely with Stig Topp-Jorgensen, who showed endless patience and good humour in the face of all my idiot T3 questions. Thanks also to Ruby and Marge for tea, chocolate and entertainment.

I couldn't have written this thesis without being able to get well away from it from time to time, and I've had a lot of fun over the last four years. First many thanks to Liz, Andrew and Nigel, for welcoming me to the group, and for all the good times discovering Geneva, skiing and walking, and Martin Bates, for being such good company for such a long time. In Oxford and in Geneva I've been privileged to work with many Vrai Hommes, not a nerd among them. Most Vrai has to be the unfeasibly broad shouldered Guy Wilkinson, with runners up the amazingly talented Cliffy, (just don't let me catch you talking to my children), amiable Alien Tim, that smooth talking hero Gazza on the Box, bendy blyth, the beautiful (if not very bright) Stevie, the great Zuberi, gorgeous pouting Paul Dauncey (21), and of course S. de Veau. Special thanks to Paula and Mary for being positively tropical, what would I have done without you. Thanks to all my friends outside the lab, to Dave and Simon for keeping me so well fed and cultured, and to John, Jennifer, Buster and Mark for great friendship and support (and eating my shoelaces).

I am grateful to the Science and Engineering Research Council for financial support.

This thesis is dedicated to my parents – try not to read it all at once!

Contents

List of Figures

List of Tables

Chapter 1

Theory

In this chapter, the theory behind Z^0 decays into pairs of muons is briefly described. Measurements of the total and differential cross section, and forward-backward asymmetry $A_{FB}^{\mu^+\mu^-}$ of Z^0 decays into $\mu^+\mu^-$, are shown to be useful in determining some parameters of the standard electroweak model to a high precision.

Thorough descriptions of the Standard Model may be found in many places [1], so only an outline of it is given here. An alternative view may be found in [2], starting with Fermi interactions and resulting in the Standard Model by introducing new gauge bosons to prevent cross sections exceeding the unitarity limit.

1.1 Gauge Theories

Before describing the Standard Model, we will take a look at one of the most fundamental concepts involved - gauge theories. In these theories, we start with a Lagrangian describing the known components of the system with which we are concerned. We then require this Lagrangian to be invariant under certain **local** gauge transformations, that is, transformations which are a function of position in space-time[1] x. For example in electromagnetism, we require the Lagrangian, which is constructed out of the field ψ, to be invariant under local phase transformations (members of the U(1) group).

$$\psi' = e^{ie\alpha(x)}\psi$$

This requirement can only be satisfied by the introduction of a new term in the Lagrangian, which represents a gauge field, the form and interactions of which are

---

[1] In contrast to a **global** gauge transformation, which is the same everywhere in space-time.

determined by the symmetry requirement imposed. Taking the electromagnetic case again, the requirement that the Lagrangian should be invariant under U(1) transformations leads to the introduction of the 4-vector field A_μ.

The U(1) invariance of electromagnetism is an **Abelian** symmetry, as the generators of U(1) (the phase transformations) commute. This means that the photon is not self interacting. In general, however, we deal with **non-Abelian** symmetries, in which the generators do not commute, and this means that the gauge bosons involved do have self interactions.

The first application of local gauge invariance to a non-abelian symmetry was due to Yang and Mills [3], who formed a gauge theory for rotations in a strong isospin space, to account for the symmetry between the proton and the neutron in strong interactions (interactions involving only hadrons). The gauge group in this case was SU(2), and three gauge fields were necessary to maintain the invariance of the Lagrangian.

1.2 The Standard Model

The Standard Model is a gauge theory unifying strong, weak and electromagnetic interactions. The full gauge group is $SU(3)_c \times SU(2)_L \times U(1)$.

Quantum ChromoDynamics (QCD) is the gauge theory describing the strong force, which is responsible for the binding of quarks into hadrons. Invariance of the Lagrangian under the gauge group $SU(3)_c$ (c for colour) [4] leads to the introduction of eight gauge fields, corresponding to eight massless vector particles called gluons.

The Standard Electroweak Model, which describes the weak and electromagnetic interactions, was developed by Glashow, Salam and Weinberg [5]. As QCD is not directly relevant to the physics of $Z^0 \rightarrow \mu^+\mu^-$, from now on the Standard Model shall be taken to be the Standard Electroweak Model only.

Firstly, local gauge invariance under $SU(2)_L$ transformations (rotations in a weak isospin space analogous to the strong isospin space postulated by Yang and Mills) results in three gauge fields of massless vector bosons labelled $W_\mu^i (i = 1,2,3)$. The subscript L indicates that the W_μ^i only couple to the left handed fermions.

Secondly, local gauge invariance under U(1) transformations, associated with a weak hypercharge y, results in an additional gauge field of massless vector bosons B_μ The weak hypercharge y, electric charge q and the third component of weak isospin t^3 are connected by the relation $y = 2(q - t^3)$.

At this stage, we have massless vector bosons W_μ^i, coupling with coupling constant g to all particles with weak isospin t - that is, the left handed leptons and quarks. One of the bosons is neutral, the others have $q = \pm 1$. We also have a neutral massless vector boson B_μ, coupling with coupling constant g' to all particles with weak hypercharge y - the leptons and quarks.

To complete the model, a mechanism called spontaneous symmetry breaking [1] is used to break the $SU(2)_L \times U(1)$ symmetry and give masses to three of the four vector bosons, and the leptons and quarks. One boson (the photon) must remain massless to preserve the U(1) invariance of electromagnetism. At least one scalar particle - the Higgs boson [6] - is needed to do this. Tables 1.1 and 1.2 give the fermions (particles with half integer spin) and bosons (particles with integer spin) which are the constituents of the Standard Model, with their t, t_3, q, and y assignments. The d', s', b' quarks are the weak eigenstates of the charge $-\frac{1}{3}$ quarks, which are not the same as their mass eigenstates d, s and b. The weak and mass eigenstates are related by the Cabibbo-Kobayashi-Maskawa (CKM) mixing matrix [7] [2]. The top quark t and Higgs boson (or bosons) have yet to be discovered.

---

[2] Mixing could also occur among the leptons and neutrinos, unless the neutrinos are massless, which is assumed to be the case for most purposes

Generation						
1.	2.	3.	t_f	t^3_f	y_f	q_f
$\begin{pmatrix} \nu_e \\ e \end{pmatrix}_L$	$\begin{pmatrix} \nu_\mu \\ \mu \end{pmatrix}_L$	$\begin{pmatrix} \nu_\tau \\ \tau \end{pmatrix}_L$	$+1/2$	$+1/2$ $-1/2$	-1	0 -1
e_R	μ_R	τ_R	0	0	-2	-1
$\begin{pmatrix} u \\ d' \end{pmatrix}_L$	$\begin{pmatrix} c \\ s' \end{pmatrix}_L$	$\begin{pmatrix} t \\ b' \end{pmatrix}_L$	$+1/2$	$+1/2$ $-1/2$	$+1/3$	$+2/3$ $-1/3$
u_R	c_R	t_R	0	0	$+4/3$	$+2/3$
d'_R	s'_R	b'_R	0	0	$-2/3$	$-1/3$

Table 1.1: Quantum numbers for the elementary fermions.

Vector Boson	t	t^3	y	q
$\begin{pmatrix} W^+ \\ Z^0 \\ W^- \end{pmatrix}$	$+1$	$+1$ 0 -1	0	$+1$ 0 -1
γ	0	0	0	0
Scalar Boson				
H	0	0	0	0

Table 1.2: Quantum numbers for gauge bosons and Higgs in the Standard Electroweak Model

The physical gauge fields are formed from the four fields W_μ^i, B_μ as follows:

$$W_\mu^\pm = \frac{1}{\sqrt{2}}\left(W_\mu^1 \mp iW_\mu^2\right) \tag{1.1}$$

$$Z_\mu = \cos\theta_W W_\mu^3 - \sin\theta_W B_\mu \tag{1.2}$$

$$A_\mu = \sin\theta_W W_\mu^3 + \cos\theta_W B_\mu \tag{1.3}$$

where θ_W is the Weak mixing angle (sometimes called the Weinberg angle). We also have the relations

$$g\sin\theta_W = g^{'}\cos\theta_W = e \tag{1.4}$$

$$M_Z = M_W/\cos\theta_W \tag{1.5}$$

$$G_F = \frac{\pi\alpha}{\sqrt{2}M_Z^2\sin^2\theta_W\cos^2\theta_W} \tag{1.6}$$

where M_W and M_Z are the masses of the W and Z bosons, G_F is the Fermi coupling constant, which is obtained from measurements of the muon lifetime and mass, e is the electric charge, and α is the fine structure constant. Table 1.3 gives recent values of M_Z, M_W, α and G_F.

Parameter	Value	Source
M_Z	91.175 ± 0.021	LEP average
M_W	79.91 ± 0.39	CDF
α	1/128 (at $Q^2 \sim M_Z^2$)	[39]
$G_F/(\hbar c)^3$	$1.16637 \times 10^{-5} GeV^{-2}$	[39]

Table 1.3: Recent values of M_Z, M_W, α and G_F.

The Feynman vertex factors [1] for the three diagrams in figure 1.1 are

$$ie\gamma^\alpha \tag{1.7}$$

$$\frac{-ig}{2\sqrt{2}}\gamma^\alpha\left(1-\gamma_5\right) \tag{1.8}$$

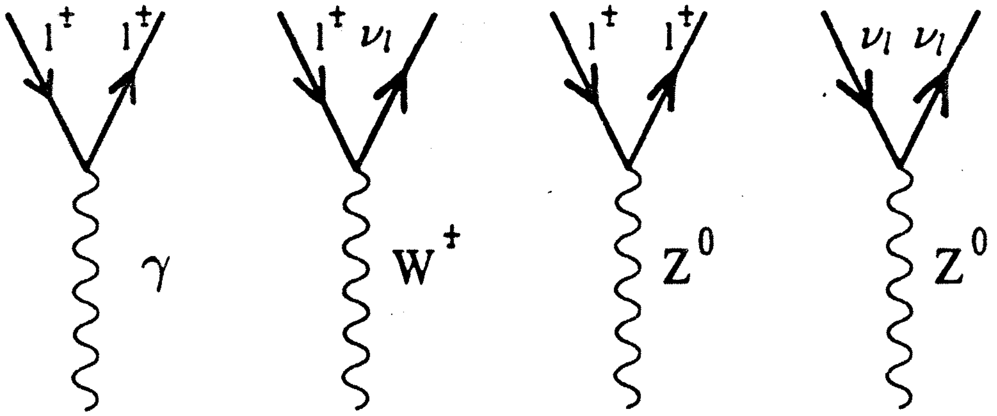

Figure 1.1: Gauge boson interactions with leptons

$$\frac{-ig}{4\cos\theta_W}\gamma^\alpha\left(v_f - a_f\gamma_5\right) \tag{1.9}$$

where v_f and a_f, the vector and axial vector coupling constants for a fermion f are given by

$$v_f = t_f^3 - 2q_f\sin^2\theta_W \tag{1.10}$$

$$a_f = t_f^3 \tag{1.11}$$

Note that the $W^\pm$ interactions are pure $V - A$, which means that only left handed fermions can take part. The term $\frac{1}{2}(1 - \gamma_5)$ is in fact a helicity projection operator, which when acting on a spinor, projects out the left handed component. The photon interactions are purely vector in nature, and the Z^0 interactions are a mixture of $V + A$ and $V - A$, parametrised by vector and axial vector coupling constants v_f and a_f. The values of v_f and a_f for the different fermions are given in table 1.4.

1.3 Choice of Renormalisation Scheme

Before outlining the derivation of expressions for the cross section and asymmetry of $e^+e^-\rightarrow\mu^+\mu^-$, a brief discussion of choice of renormalisation scheme is

Fermion f	q_f	v_f	a_f	$v_f(\sin^2\theta_W = 0.225)$
e^-, μ^-, τ^-	-1	$-\frac{1}{2} + 2\sin^2\theta_W$	$-\frac{1}{2}$	-0.05
ν_e, ν_μ, ν_τ	0	$\frac{1}{2}$	$\frac{1}{2}$	0.5
d, s, b	$-\frac{1}{3}$	$-\frac{1}{2} + \frac{2}{3}\sin^2\theta_W$	$-\frac{1}{2}$	-0.35
u, c, t	$\frac{2}{3}$	$\frac{1}{2} - \frac{4}{3}\sin^2\theta_W$	$\frac{1}{2}$	0.2

Table 1.4: Values of the vector and axial vector coupling constants v_f and a_f for the elementary fermions

appropriate. The Standard Model is a renormalisable theory, that is, observables may be calculated to any order of perturbation theory in terms of a finite number of input parameters. The choice of these input parameters, and the energy at which they are defined, is a choice of renormalisation scheme.

The most basic choice of input parameters consists of the coupling constants g and g', two constants μ^2 and λ to describe the Higgs potential, and coupling constants g_f of the Higgs to each fermion. However, none of these are directly physically measurable, and a more convenient choice of input parameters is

$$\alpha, M_Z, M_W, M_H, m_f \tag{1.12}$$

where the W and Z^0 masses are defined on their mass shells[3], and the m_f are the fermion masses and quark mixing angles.

1.4 The Reaction e$^+$e$^-$$\rightarrow$$\mu^+\mu^-$

To lowest order, this process is described by the Feynman diagrams in figure 1.2. The Feynman amplitude is given by $\mathcal{M} = \mathcal{M}_\gamma + \mathcal{M}_{Z^0}$, where

$$\mathcal{M}_\gamma = ie^2 \left(\bar{u}_\mu \gamma^\alpha w_\mu\right) \frac{1}{k^2} \left(\bar{w}_e \gamma_\alpha u_e\right) \tag{1.13}$$

---

[3] The physical mass of a particle is defined to be the point at which the real part of the denominator of its propagator disappears

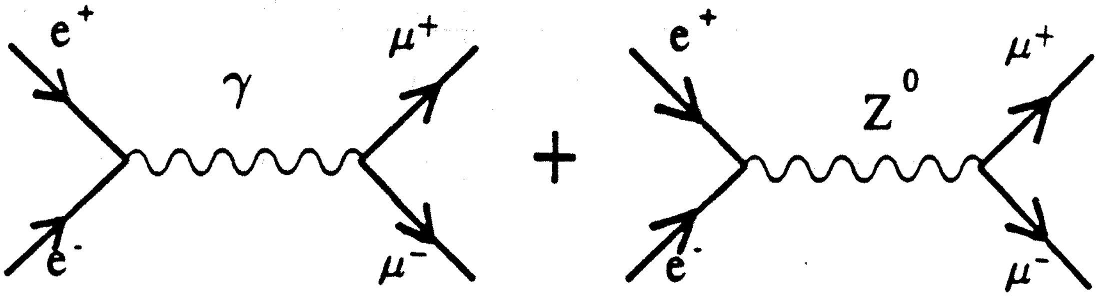

Figure 1.2: Lowest order Feynman diagrams for $Z^0 \rightarrow \mu^+\mu^-$

$$\mathcal{M}_{Z^0} = \frac{ig^2}{4\cos^2\theta_W}\left[\bar{u}_\mu\gamma^\alpha\left(v_\mu - a_\mu\gamma_5\right)w_\mu\right]\frac{1}{k^2 - M_Z^2 + iM_Z\Gamma_Z}\left[\bar{w}_e\gamma_\alpha\left(v_e - a_e\gamma_5\right)u_e\right] \tag{1.14}$$

Here v_e, v_μ, and a_e, a_μ are the vector and axial vector coupling constants for electrons and muons, and $\bar{w}_e$, u_e w_μ, $\bar{u}_\mu$ are the spinors for the initial e^+e^- pair and final $\mu^+\mu^-$ pair respectively. The part of the Z^0 propagator which gives rise to terms dependent on the lepton masses has been omitted, and the inclusion of the $iM_Z\Gamma_Z$ term in the propagator accounts for the effect of the Z^0 width Γ_Z.

The expression for the differential cross section for the process $Z^0 \rightarrow \mu^+\mu^-$ may be derived using the above amplitudes, giving

$$\frac{d\sigma}{d\Omega} = F(s)(1 + \cos^2\theta) + G(s)\cos\theta \tag{1.15}$$

where

$$F(s) = \frac{\alpha^2}{4s}[1 + 2v_e v_\mu \Re e(\chi) + (v_e^2 + a_e^2)(v_\mu^2 + a_\mu^2)|\chi|^2] \tag{1.16}$$

$$G(s) = \frac{\alpha^2}{4s}(4a_e a_\mu \Re e(\chi) + 8v_e v_\mu a_e a_\mu |\chi|^2) \tag{1.17}$$

and

$$\chi = \frac{1}{4\sin^2\theta_W\cos^2\theta_W}\frac{s}{(s - M_Z^2 + iM_Z\Gamma_Z)} \tag{1.18}$$

where $\sqrt{s}$ is the centre of mass energy, θ is defined in figure 1.3, and terms in $|\chi|^2$ are due to Z^0 exchange, terms independent of χ are due to γ exchange, and terms in $\Re e(\chi)$ are due to Z^0 - γ interference.

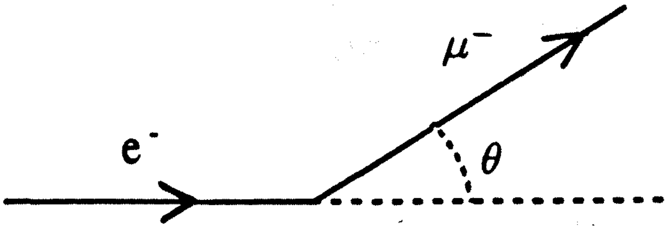

Figure 1.3: Definition of θ for A_{FB}

1.5 Cross sections and Asymmetries

The total cross section and forward-backward asymmetry are obtained from the differential cross section as follows:

$$\sigma_T = \sigma_F + \sigma_B \tag{1.19}$$

$$A_{FB} = \frac{\sigma_F - \sigma_B}{\sigma_T} \tag{1.20}$$

$$\sigma_F = 2\pi \int_0^1 \frac{d\sigma}{d\Omega} d\cos\theta \tag{1.21}$$

$$\sigma_B = 2\pi \int_{-1}^0 \frac{d\sigma}{d\Omega} d\cos\theta \tag{1.22}$$

Substituting 1.15 in the above we obtain

$$\sigma_T = \frac{16\pi}{3} F(s) \tag{1.23}$$

and neglecting the pure electromagnetic term and the $\gamma - Z$ interference term, the following expression for the cross section around the Z^0 peak is obtained.

$$\sigma_T = \frac{\pi\alpha^2}{12} \frac{(v_e^2 + a_e^2)(v_\mu^2 + a_\mu^2)}{\sin^4\theta_W \cos^4\theta_W} \frac{s}{[(s - M_Z^2)^2 + M_Z^2\Gamma_Z^2]} \tag{1.24}$$

so the peak cross section $\sigma_T^{s=M_Z^2}$ is proportional to $(v_e^2 + a_e^2)(v_\mu^2 + a_\mu^2)$.

The forward-backward asymmetry may also be calculated, giving

$$A_{FB} = \frac{3}{8} \frac{G(s)}{F(s)} \tag{1.25}$$

using 1.16,1.17 and 1.18, and assuming $s \sim M_Z^2$ and that $v_l^2 << a_l^2$ the following expression is obtained

$$A_{FB} = \frac{3}{4}\left[1 + \frac{2\sin^2\theta_W\cos^2\theta_W}{v_e v_\mu}(1 - M_Z^2/s)\right] A_e A_\mu \tag{1.26}$$

where

$$A_l = \frac{2v_l a_l}{v_l^2 + a_l^2} \tag{1.27}$$

Thus the peak asymmetry is proportional to $A_e A_\mu$, and around the peak A_{FB} varies as the square of the centre of mass energy.

From the above two results, it can be seen that as $v_l^2 << a_l^2$ the peak cross section is mainly determined by a_l, and the peak asymmetry by v_l/a_l.

1.6 Partial Widths

The total width Γ_Z of the Z^0 is related to its lifetime τ_Z by $\Gamma_Z = \hbar/\tau_Z$. Γ_Z may also be expressed as the sum of the partial widths of the Z^0 to each possible decay channel, i.e. $\Gamma_Z = \Gamma_{\nu_e} + \Gamma_e + \Gamma_u + \Gamma_d \ldots$, where the leptonic widths are given by

$$\Gamma_l = \frac{\alpha M_Z^2}{12\sin^2\theta_W\cos^2\theta_W}(v_l^2 + a_l^2) \tag{1.28}$$

Using this expression for Γ_l, the expression for the cross section for $e^+e^- \rightarrow \mu^+\mu^-$, near $s = M_Z^2$ and for the Z^0exchange term, may be rewritten as

$$\sigma_T = \sigma_0 \frac{M_Z^2\Gamma_Z^2}{[(s - M_Z^2)^2 + M_Z^2\Gamma_Z^2]} \tag{1.29}$$

where σ_0 is the peak cross section, given by

$$\sigma_0 = 12\pi \frac{\Gamma_e\Gamma_\mu}{M_Z^2\Gamma_Z^2} \tag{1.30}$$

To summarise the above two sections, we have arrived at lowest-order expressions for the Z^0 cross section and asymmetry in the $\mu^+\mu^-$ channel, assuming that the electron and muon masses are negligible. These may be parametrised in terms of α, $\sin^2\theta_W$, M_Z, M_W, G_F, which are related by equations 1.5 and 1.6. Real life, however, is not so simple - many more Feynman diagrams than those in figure 1.2 must be taken into account when calculating σ and A_{FB}. The next section shows how this is done at LEP by some simple modifications to the lowest order equations.

1.7 Radiative Corrections

Radiative corrections at LEP can be divided into two classes - QED corrections, and weak corrections [11, 8, 13].

QED corrections involve, in the first order of the perturbation series, one photon either as initial or final state bremsstrahlung, or in a loop, as shown in figure 1.4. Since these corrections depend on experimental cuts (for example, in the $\mu^+\mu^-$ channel, selection cuts involve a requirement for the muon tracks to be above a certain momentum, and initial or final state bremsstrahlung reduces the muon momenta), and are large at LEP energies, they need to be carefully taken into account, although they do not provide an insight into new physics.

Weak Corrections consist of:

1. Propagator corrections, as shown in fig 1.5. These corrections are flavour independent and independent of experimental cuts. They contain contributions from both the top quark and Higgs boson, and so have some dependence on their masses, m_t and M_H . They form the largest contribution to the weak corrections.

2. Vertex corrections, as shown in the top of fig 1.6, which are flavour dependent and independent of experimental cuts. For light final state fermions (all but b and t) the important vertex corrections are those containing virtual W and Z bosons. For $b\bar{b}$ final states, however, there are large vertex corrections from loops involving b, t and W as shown in fig 1.7 [4].

3. Box corrections, as shown in the bottom of fig 1.6, which are also flavour dependent. They are non resonant and so small near the Z^0 peak, but do depend on the fermion scattering angle, and so the experimental cuts need to be considered in the calculation of the correction.

The next two sections describe how these corrections are taken into account.

---

[4] Indeed, if the top quark does not exist, then the standard model would be in serious trouble.

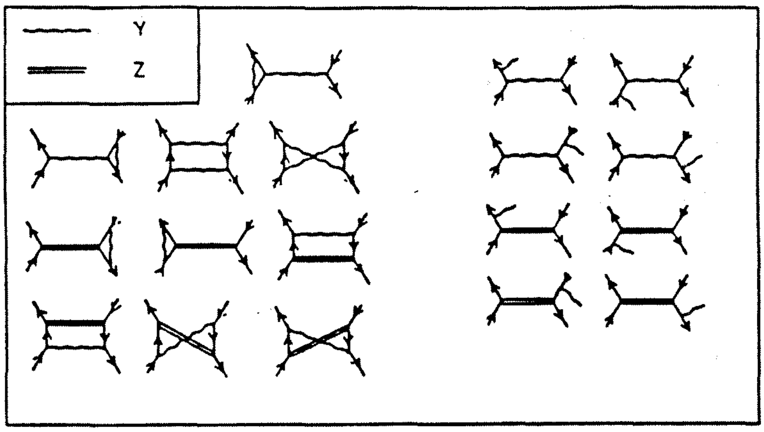

Figure 1.4: QED corrections to $e^+e^- \rightarrow \mu^+\mu^-$ (from [11])

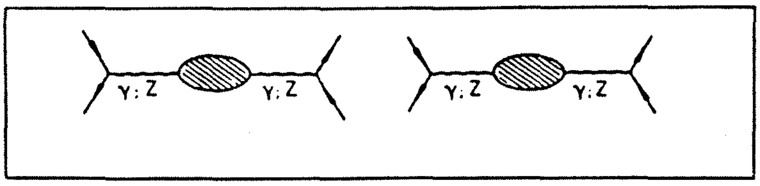

Figure 1.5: Propagator corrections to $e^+e^- \rightarrow \mu^+\mu^-$ (from [11])

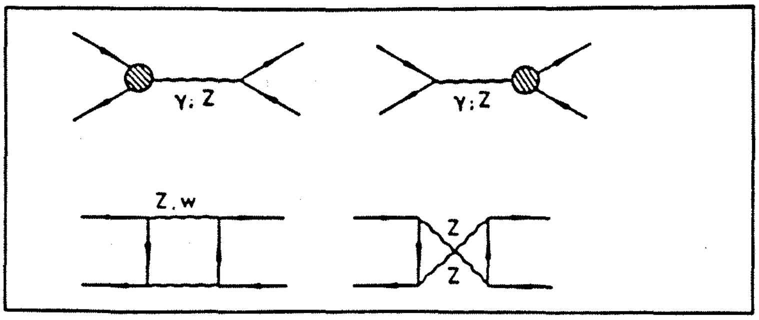

Figure 1.6: Vertex and Box corrections to $e^+e^- \rightarrow \mu^+\mu^-$ (from [11])

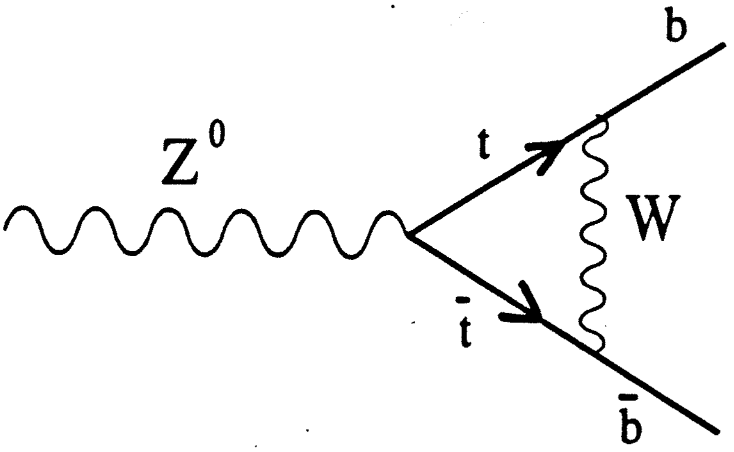

Figure 1.7: Vertex Correction to $e^+e^- \rightarrow b\bar{b}$ involving the top quark, t

1.7.1 Improved Born Approximation

The weak corrections are dealt with as follows:

Firstly, the flavour independent parts and flavour dependent vertex corrections are absorbed in a redefinition of the weak mixing angle to be an effective weak mixing angle $\sin^2\theta_W{}^{eff}$, and the introduction of an effective rho parameter ρ_{eff} [5] [6], so that equations 1.5 and 1.6 become equations 1.31 and 1.32.

$$M_Z = M_W/\sqrt{\rho_{eff}}\cos\theta_{W_{eff}} \tag{1.31}$$

$$G_F = \frac{\pi\alpha(M_Z^2)}{\sqrt{2}\rho_{eff}M_Z^2\sin^2\theta_W{}^{eff}\cos^2\theta_W{}^{eff}} \tag{1.32}$$

The fine structure constant α is replaced by its renormalised value at $s = M_Z^2$[7], and the expression for χ given in equation 1.18 should be replaced by equation 1.33 [10, 11](4.6).

$$\chi = \frac{1}{4\sin^2\theta_W{}^{eff}\cos^2\theta_W{}^{eff}}\frac{s}{(s - M_Z^2 + is\Gamma_Z/M_Z)} \tag{1.33}$$

Effective vector and axial vector coupling constants $\bar{a}_f$ and $\bar{v}_f$ are also defined in terms of ρ_{eff} and $\sin^2\theta_W{}^{eff}$, as shown in equations 1.34, and 1.35.

$$\bar{a}_f = t_f^3\sqrt{\rho_{eff}} \tag{1.34}$$

---

[5] ρ at lowest order is equal to 1.

[6] This is only one choice of $\sin^2\theta_W{}^{eff}$, many other parametrisations are possible, but they will not be considered here.

[7] $\alpha(s = M_Z^2) = 1/128.8 \pm 0.1$.

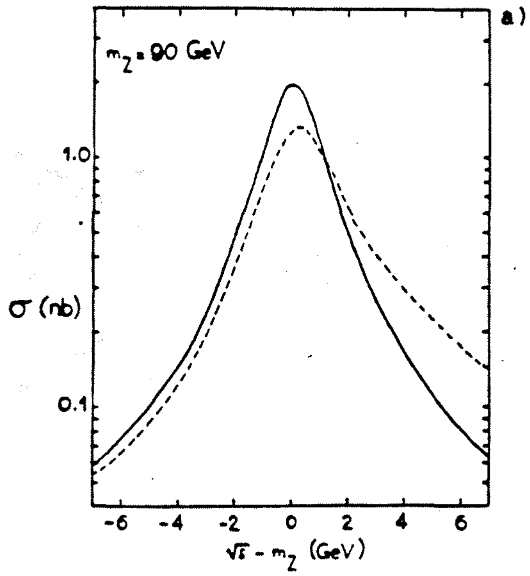

Figure 1.8: Total cross section for $e^+e^- \rightarrow \mu^+\mu^-$ in Born approximation (solid line) and including the complete first order QED corrections (dashed line), from [12]

$$\bar{v}_f = \sqrt{\rho_{eff}}(t_f^3 - 2q_f \sin^2\theta_W{}^{eff}) \tag{1.35}$$

The remaining weak corrections, i.e. box corrections and corrections due to the imaginary part of the Z^0 propagator, together with terms due to photon exchange, are collected together into flavour dependent residual terms when the cross sections and asymmetries are calculated.

The above parametrisation is called the Improved Born Approximation (IBA), and gives expressions for the cross sections and asymmetries which maintain their Born level structure, absorbing the most significant weak corrections in the modified parameters.

1.7.2 QED Corrections

The dominant QED corrections, which are due to initial state Bremsstrahlung, are included by convoluting IBA expressions for the cross section with a radiator function H. These corrections are particularly significant for the Z^0 line shape, as they lead to a 30% reduction in the Born level peak cross section and an alteration of the shape of the resonance, shifting it upwards slightly and giving it a radiative tail above $s = M_Z^2$, as illustrated in figure 1.8. Equation 1.36 [9] gives the expression for the observed cross section for $e^+e^- \to \mu^+\mu^-$.

$$\sigma^{\mu}_{obs}(s) = \int_0^s \left[\sigma^{\mu}_W(s').H(s,s') + F_{int}\right] ds' \tag{1.36}$$

where F_{int} describes the interference of initial and final state radiation, and QED box diagrams, and s' is the square of the invariant mass of the muons. σ^{μ}_W is given in equation 1.37, and is the IBA expression for the cross section.

$$\sigma^{\mu}_W = \frac{\sigma_0}{\left(1+\frac{3\alpha}{4\pi}\right)} \frac{s\Gamma_Z^2}{\left[(s-M_Z^2)^2 + \frac{s^2\Gamma_Z^2}{M_Z^2}\right]} \tag{1.37}$$

where the peak cross section may again (see equation 1.30) be written as

$$\sigma_0 = 12\pi \frac{\Gamma_e \Gamma_\mu}{M_Z^2 \Gamma_Z^2} \tag{1.38}$$

provided we use the IBA expressions for the partial widths in terms of effective vector and axial vector coupling constants.

$$\Gamma_l = \frac{G_F M_Z^3}{6\pi\sqrt{2}} \left(\bar{v}_l^2 + \bar{a}_l^2\right) \left(1 + \frac{3\alpha}{4\pi}\right) \tag{1.39}$$

In the expressions for σ^{μ}_{obs} and Γ_l there is a QED correction factor $\left(1+\frac{3\alpha}{4\pi}\right)$ which takes into account final state radiation - this appears in the expression for σ^{μ}_{obs} in order to avoid double counting since only one of the Γ_l (in our case Γ_μ) should bring in a final state correction.

The new expression for the muon forward-backward asymmetry at $s = M_Z^2$ is

$$A^{\mu}_{FB} = \frac{3}{4}\bar{A}_e \bar{A}_\mu + \Delta A^{\mu,res}_{FB} \tag{1.40}$$

where $\bar{A}_e$ and $\bar{A}_\mu$ are given as in equation 1.27, but with the Born level vector and axial vector coupling constants replaced by $\bar{v}_e, \bar{v}_\mu$ and $\bar{a}_e, \bar{a}_\mu$. $\Delta A^{\mu,res}_{FB}$ is the contribution to the asymmetry from weak corrections not absorbed in the IBA, and photon exchange, and is about 0.002, with a small dependence on the top quark and Higgs masses. A similar expression to 1.36 may be written for the observed forward-backward asymmetry [8].

To summarise the above two sections, we have arrived at expressions for the observed cross section and forward-backward asymmetry in $e^+e^- \to \mu^+\mu^-$ at LEP, by

1. absorbing most significant weak radiative corrections into a redefinition of the weak mixing angle and introduction of a ρ parameter - this is called the Improved Born Approximation

2. convoluting the IBA expressions with a radiator function to include the effect of initial state bremsstrahlung.

Less significant radiative corrections are collected together in residual terms.

1.8 Extraction of electroweak parameters from experimental measurements

For the comparison of Standard Model predictions for cross sections and asymmetries with their experimentally determined values, a program called ZFITTER [16] is used. ZFITTER calculates cross sections and asymmetries essentially as described above, and has the useful feature that experimental cuts, for example cuts on the production angle θ and acolinearity, may be input to the program. To extract $\bar{v}_l$ and $\bar{a}_l$ (or $\sin^2\theta_W{}^{eff}$ and ρ_{eff}) from measurements of σ and A_{FB} three types of fit are performed, all the fits assume lepton universality.

1. A **lineshape fit** to the cross section data.

2. A **combined fit** to both the cross section and asymmetry measurements, where the asymmetries are extracted from the data using the maximum likelihood method.

3. A fit to the cross section as a function of production angle θ of the negative muon.

1.8.1 Lineshape Fits

For a lineshape fit, the measured cross section of $e^+e^-\rightarrow\mu^+\mu^-$ at 8 centre of mass energies are used. ZFITTER is used to calculate the expected cross section at each point as a function of the lineshape parameters (see equations 1.36,1.37,1.38) M_Z, Γ_Z, Γ_l, and the square of the centre of mass energy s, which is provided by the LEP operations group.

The first fit is a three parameter fit to M_Z, Γ_Z and Γ_l. This fit is performed purely as a check for consistency between the $\mu^+\mu^-$data and the hadronic data, as the precision obtained on M_Z and Γ_Z is much lower than that given by a fit to the hadronic data, and a much more precise value of Γ_l will be obtained in the next fit.

In the second fit to the cross section data, M_Z and Γ_Z are obtained from the DELPHI hadronic data, and a one-parameter fit to determine the best value for Γ_l is performed, from which $(\bar{v}_l^2 + \bar{a}_l^2)^2$ may be obtained.

1.8.2 Combined Fit

Since measurement of the cross section is a measurement of $(\bar{v}_l^2 + \bar{a}_l^2)$, and the asymmetry measurements are sensitive to the value of $\bar{v}_l^2/\bar{a}_l^2$, a combined fit to both cross section and asymmetry measurements can give values for both $\bar{v}_l^2$ and $\bar{a}_l^2$. The cross section and asymmetry measurements at 8 centre of mass energies are used, giving 16 measurements in total. ZFITTER calculates σ as a function of M_Z, Γ_Z, s and $\bar{v}_l^2$ and $\bar{a}_l^2$. A_{FB} is calculated as a function of s, $\bar{v}_l^2$ and $\bar{a}_l^2$. M_Z, Γ_Z and s are again provided by the DELPHI hadronic results and the LEP group, and we perform two-parameter fit to obtain values for $\bar{v}_l^2$ and $\bar{a}_l^2$.

1.8.3 Differential Cross Section

An alternative to the combined fit is a fit to the cross section as a function of $\cos\theta$ - at each centre of mass energy, the cross section in several $\cos\theta$ bins is calculated, the number of bins depending on the amount of data at that energy. While the maximum likelihood method of calculating asymmetries[8] combined with a measurement of total cross section gives a very accurate measurement of $\bar{v}_l$ and $\bar{a}_l$ within the standard model, the differential cross section measurement gives a more model independent measurement, since it makes no assumptions about the angular distribution of events. It thus has the potential to be used as a tool for looking for new physics (compositeness, for example, would cause deviations in the angular distributions expected from elementary particles).

---

[8] See Chapter 4

Chapter 2

LEP and DELPHI

2.1 The LEP Collider

LEP, the Large Electron Positron collider at CERN, is currently producing electron - positron collisions at centre of mass energies of $90 - 95 GeV/c$, and luminosities of order $5 \times 10^{30} cm^{-2} s^{-1}$.[1]

The LEP tunnel is $26.7 km$ in circumference, and consists of 8 straight sections, two of which house RF accelerating cavities, and 8 arcs containing bending magnets. LEP currently operates with four evenly spaced bunches of electrons, and four bunches of positrons, which means that there could be e^+e^-collisions at eight points around the ring. These interaction regions are positioned in the middle of each of the straight sections, four of which house the large LEP detectors. At the other four interaction regions the e^+ and e^- beams are prevented from colliding by electrostatic separators. A plan of LEP is shown in fig 2.1, with the positions of each detector, the RF accelerating cavities and the injection points all indicated.

The electrons and positrons used in LEP are produced using almost the whole of CERN's system of accelerators, as summarised below. Figure 2.2 shows the LEP injector chain.

1. Positrons are produced by an intense electron beam from a 200MeV LINAC incident on a tungsten target - this beam is produced by a high intensity electron gun. Electrons are produced by a low intensity electron gun near the target.

2. Another LINAC then accelerates the electrons or positrons to 600MeV.

---

[1] $1 nb = 10^{-33} cm^2$. The design luminosity is $1.7 \times 10^{31} cm^{-2} s^{-1}$.

3. The Electron Positron Accumulator ring (EPA) accumulates the 600MeV positrons or electrons.
4. The beams are then injected into the Proton Synchrotron (PS), where they are accelerated to 3.5GeV.
5. From the PS they are injected into the Super Proton Synchrotron (SPS) to be accelerated to 20GeV.
6. From the SPS the 20GeV beams are injected into LEP, where they are accumulated until there is sufficient luminosity.
7. The acceleration to the final energy of around 45GeV takes place in LEP, followed by 'squeezing' of the beams to optimise the luminosity.

The main LEP design parameters are given in table 2.1, and a summary of LEP's performance in 1989-1991 is given in table 2.2. A good general description of LEP may be found in [17], and [18] covers the design of LEP in great detail.

Future upgrades planned for LEP include:

- The introduction of 8 bunches of both electrons and positrons, to increase the available luminosity. This has already been attempted, and it is planned that this will be introduced in September 1992.
- An increase of the beam energy to around 100GeV, to allow the production of W^+W^- pairs. Superconducting RF cavities will be installed in the LEP tunnel to increase the accelerating power with minimal increase in power consumption.
- Longitudinal polarisation of the LEP beams - 50% longitudinal polarisation would allow electroweak parameters to be measured with significantly greater precision than is achieved with unpolarised beams. The LEP beams have a natural tendency to become transversely polarised, and it is planned to speed up this polarisation using 'wiggler' magnets, and then produce longitudinally polarised beams using spin rotators.
- A further phase of running with significantly higher luminosity is also under consideration. This could involve running with even more bunches, subject of course to a better understanding of the machine.

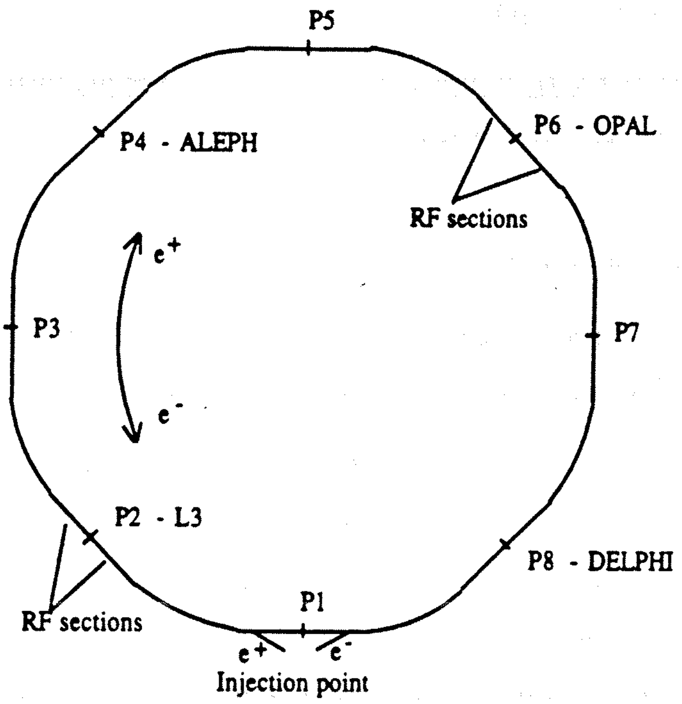

Figure 2.1: Plan of the LEP ring

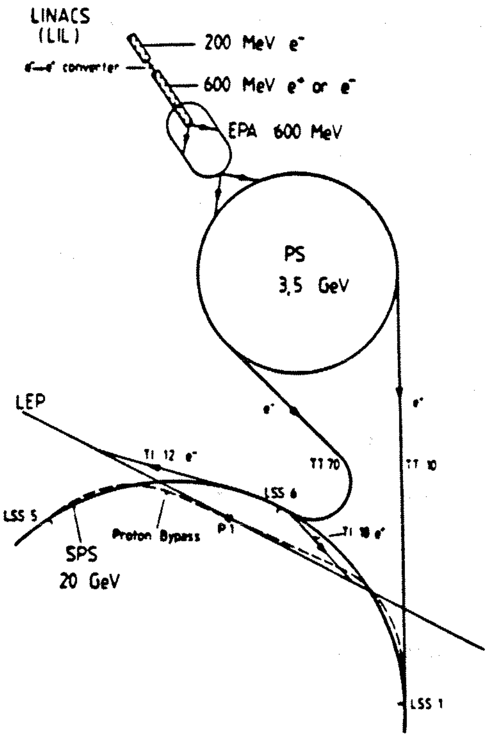

Figure 2.2: The LEP injector chain

Circumference	$26658.883m$
Average Radius	$4243.893m$
Bending Radius	$3096.175m$
Phase advance/period	60 or 90 degrees
Horizontal betatron wave number	70.35 or 94.35
Vertical betatron wave number	78.20 or 98.20
Momentum compaction factor	3.866×10^{-4}
Number of bunches per beam	4
Number of interaction points	$4+4$
Equipped experimental areas (2,4,6,8)	4
Ratio horizontal/vertical β-values at the interaction point	25
RF frequency	$352.20904MHz$
Revolution time	$88.92446\mu s$
Harmonic number	31320
Nominal klystron output power (total)	$16MW$
Active RF structure length	$272.377m$
RF gradient	$1.474MV/m$
Injection energy	$20GeV$
Maximum beam energy (at zero luminosity)	$\sim 60GeV$
Peak luminosity	$1.6 \times 10^{31} cm^{-2}s^{-1}$
Beam energy at peak luminosity	$55GeV$

Table 2.1: Main design parameters of LEP

	Integrated lumi. (pb^{-1})/Hadronic Z^0(1000s)			
Experiment	1989	1990	1991	Total
ALEPH	1.7/29	9.7/170	17.4/321	28.8/520
DELPHI	1.4/13	8.0/125	17.2/277	26.6/415
L3	1.7/19	7.8/117	17.6/304	27.1/440
OPAL	1.7/29	8.9/144	16.9/350	27.5/524
Total	6.5/91	34.4/556	69.1/1252	110.0/1899

Table 2.2: Performance of the LEP collider in 1989-1991

2.2 LEP Energy Measurement

A description of the LEP energy measurement for 1990 and 1991 may be found in [19].

For the 1990 data, the energy measurement relied upon continuous measurement of the magnet currents, using a reference magnet connected in series with the main ring magnets. This is called the Field Display system - the energy E_{FD} thus estimated is used as a reference for all other measurements. Regular flux loop measurements (using flux loops embedded in the magnets, which were calibrated before the magnets were installed) were also performed, and one calibration using protons was made. The estimated systematic error on the centre of mass energy for the 1990 data is $20MeV$. The energies quoted in this thesis are slightly different from the 1990 energies already published by DELPHI, as they include certain corrections recommended by the LEP group in [19], in the light of their greater understanding of the energy calibration in 1991.

The data taken before 14th August 1991 (which includes all of the 1991 data used in this thesis) is also assumed to have a systematic error in the centre of mass energy of $20MeV$, almost completely correlated with that of the 1990 data. After this date, the cooling system for the LEP dipoles was improved, to make the magnet temperatures more stable, but this caused a systematic shift in the flux loop measurements. This means that although the systematic error after the 14th of August was reduced to 7MeV by the introduction of a new method of calibration (resonant depolarisation), this improvement could not be used to improve the systematic error on data taken before the 14th of August.

2.3 DELPHI

DELPHI (Detector with Lepton, Photon and Hadron Identification) is one of four experiments that have been built to study the products of high energy electron -positron collisions in LEP. It was designed and built between 1982 and 1989[3] by an international collaboration of around 520 physicists and engineers, from 39 institutes[4]. The UK institutes involved in DELPHI are Oxford University, Liverpool University, and the Rutherford Appleton Laboratory.

Figures 2.3 and 2.4 give an impression of the size and layout of DELPHI - the detector can be separated into three sections, the central barrel through which the LEP beam pipe passes, and two endcaps which plug into the ends of the barrel, ensuring coverage of almost the full solid angle. The standard DELPHI coordinate system is shown in fig 2.5, in which x points towards the centre of LEP and y points upwards. The endcaps are labelled A and C, and the sides of the barrel are labelled B and D as shown.

DELPHI was designed with the following requirements in mind:

- Particle identification (identification of electrons and muons, and separation of pions, kaons and protons over a wide energy range) over almost 90% of solid angle, using a combination of standard techniques (electromagnetic and hadron calorimetry, muon chambers and dE/dx measurement in the TPC) with Ring Imaging CHerenkov detectors (RICHes).
- Precise vertex determination with a Silicon Microvertex Detector.
- Fine granularity in most components, giving precise three-dimensional information on particle tracks and energy deposits.

The next two sections contain brief descriptions of those components of DELPHI relevant to the $\mu^+\mu^-$analysis. More information about DELPHI, and in particular about the ring imaging cherenkov detectors, may be found in [20] and [21]. Tables 2.3 and 2.4 give the specifications (acceptance, resolution etc) of each detector.

---

[3] The first letter of intent was in 1982, and the first physics run was in August 1989.

[4] These numbers are from the first DELPHI paper - many more people than this have been involved in DELPHI.

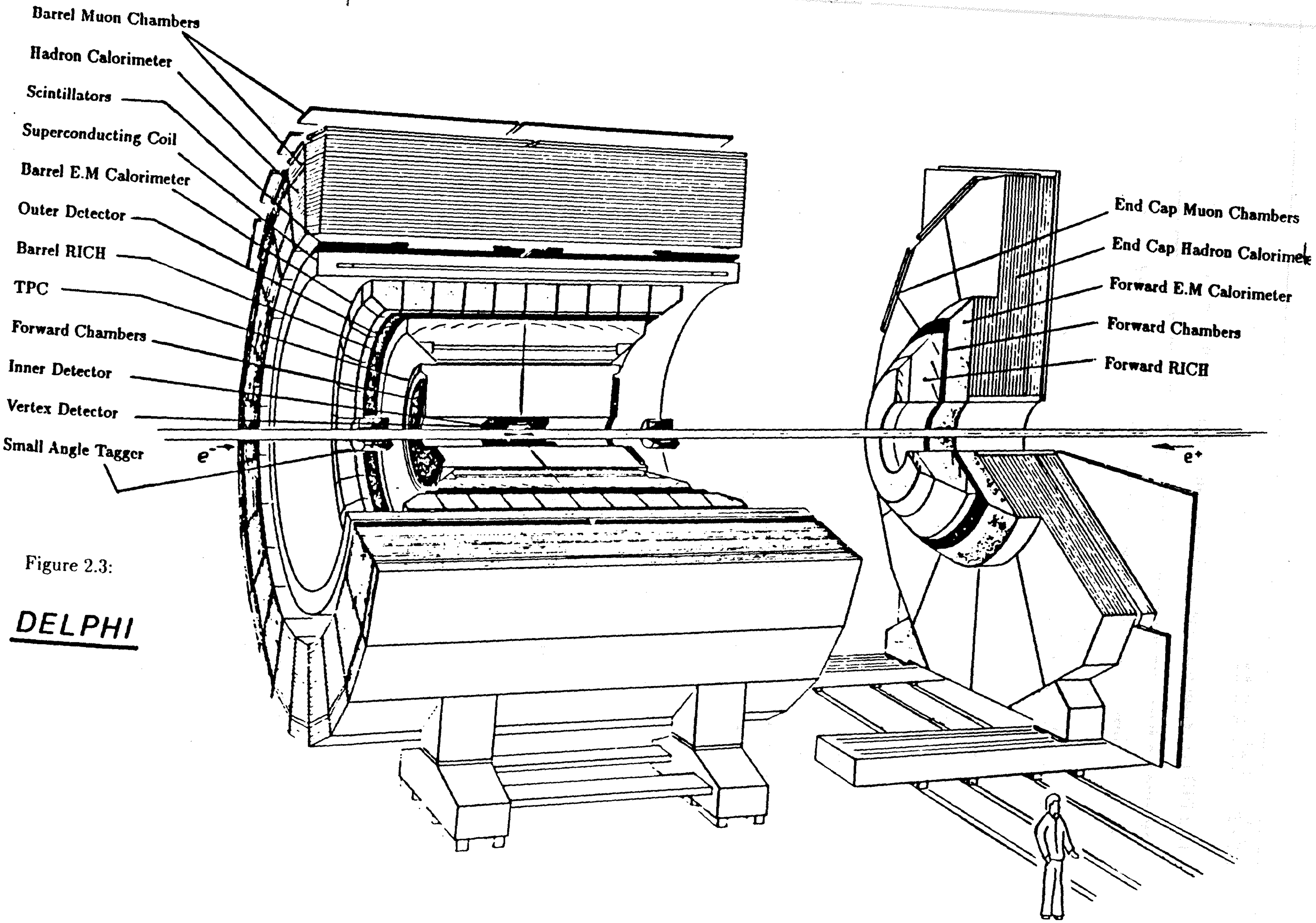

Figure 2.3:

DELPHI

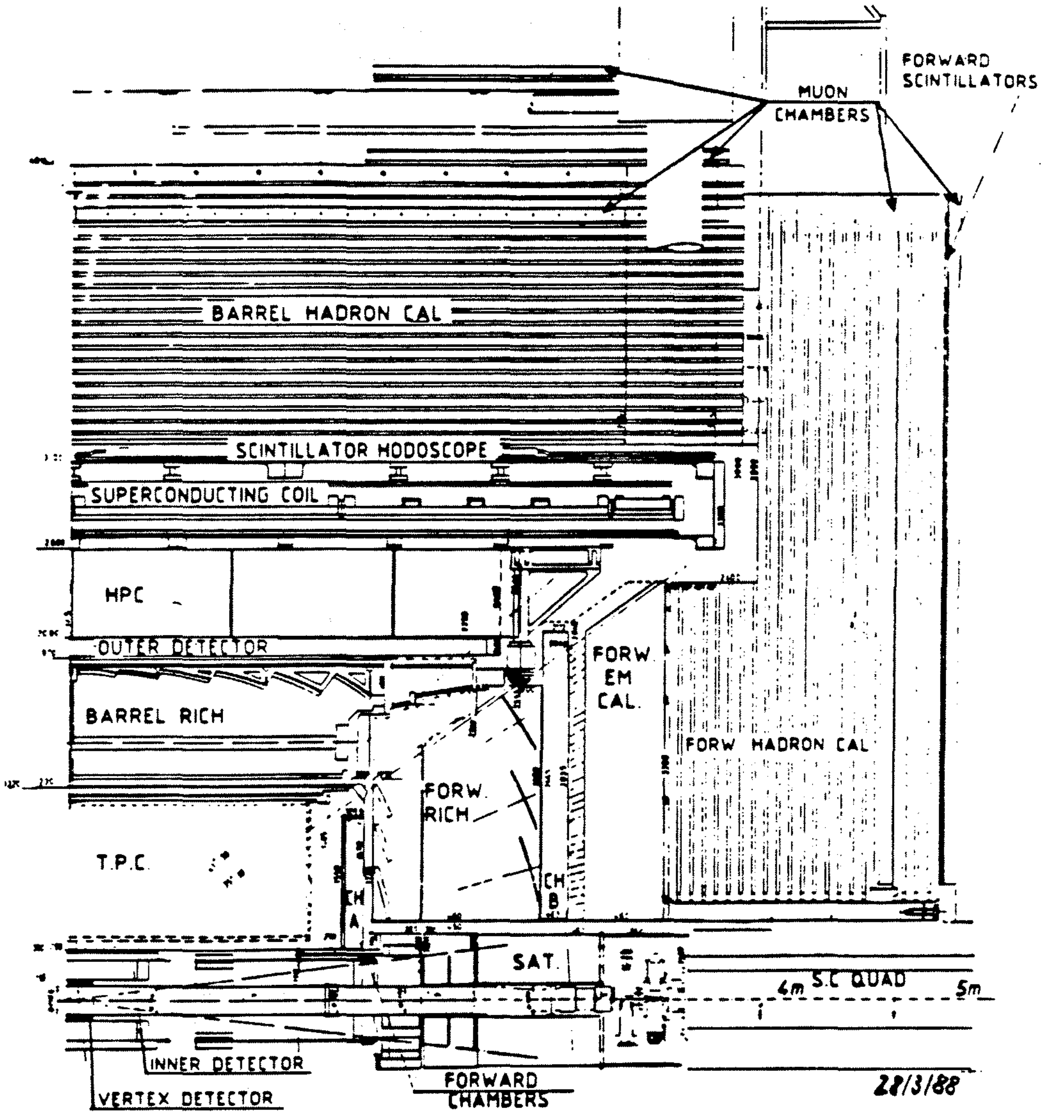

Figure 2.4: Longitudinal section through DELPHI

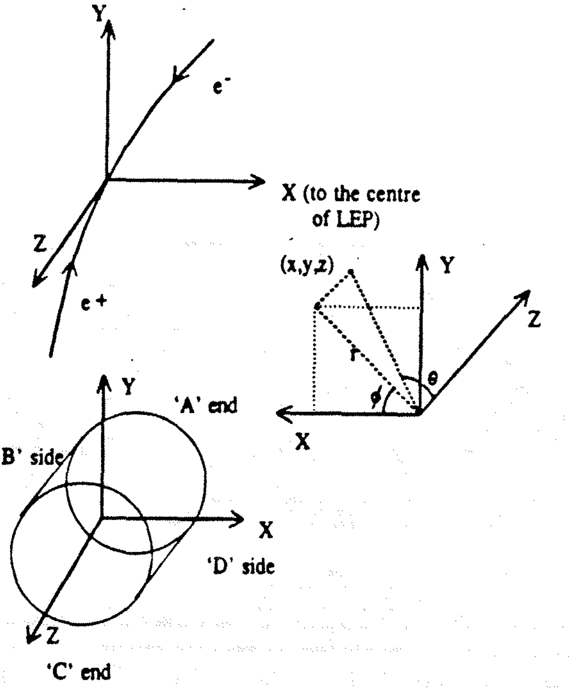

Figure 2.5: The DELPHI coordinate system

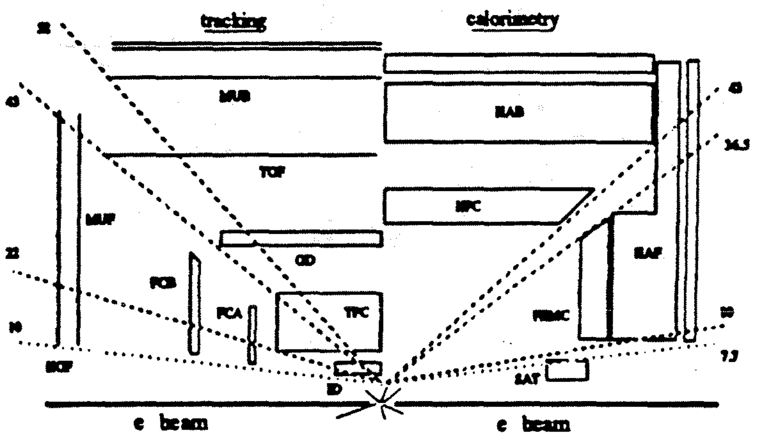

Figure 2.6: Relative Positions of DELPHI's Tracking Detectors

2.3.1 Tracking Detectors

The measurement of the momentum and direction of charged particles in DELPHI is performed by a combination of its main tracking detector, which is a Time Projection Chamber , with the inner and outer detectors in the barrel region, and forward chambers A and B in the endcap regions. Figure 2.6 shows the relative positions of the tracking detectors, and indicates the regions of θ in which they lie.

Vertex Detector

The **Vertex Detector (VD)** consists of three (two in 1990) concentric cylinders of Silicon strip detectors at radii of 6.3, 9 and 11 cm, each covering $\pm 12cm$ in z. The cylinders are made up of 24 overlapping modules, each carrying 4 detectors along z. The Silicon strips are parallel to the beam direction, so the coordinate we obtain from the VD is $R\phi$, and the pitch is $50\mu m$. The effective resolution obtained was $\sigma_{R\phi} = 14\mu m$ in 1990.

Inner Detector

The **Inner Detector (ID)** is a jet chamber surrounded by five layers of Multi-Wire Proportional Chambers (MWPCs) with circular cathode strips concentric with the beampipe. The jet chamber provides up to 24 $R\phi$ points per track, and the cathode strips give z information. Information from the outer layers contributes to DELPHI's trigger.

Time Projection Chamber

The **Time Projection Chamber (TPC)** consists of a cylindrical volume of gas, divided in two by a plane at $\theta = 90^\circ$. The drift electric field (of about $150V/cm$) is axial so that ionisation produced by charged tracks drifts towards planes of sense wires and circular cathode pads at the outer ends of the TPC. The endcaps are divided into six 60° sectors, the first sector boundary being at $\phi = 30^\circ$. The momentum resolution obtained for $45GeV$ muons was $\sim 9\%$ in 1991.

Forward Chamber A

Forward Chamber A (FCA) is a wire chamber which extends the central tracking into the endcaps. Three chambers, each with two planes of sense wires and cathode strips (rotated by 60° with respect to the wires), are sandwiched together, with the wires in the different chambers rotated by 120° with respect to one another, to aid pattern recognition.

Outer Detector and Forward Chamber B

The presence of the **Outer Detector (OD)** and **Forward Chamber B (FCB)** is made necessary by the existence of DELPHI's unique feature, the RICHes, which occupy space that in other detectors (e.g. ALEPH) is filled entirely by a central tracking detector. These tracking detectors provide measurement of charged tracks at larger distances from the interaction vertex than those covered by the TPC and FCA, resulting in an improvement in momentum resolution by a factor of at least four for the Outer Detector.

The Outer Detector consists of 24 modules, each made up of five staggered layers of drift tubes. The drift tubes provide excellent $R\phi$ information, and some z information (from the differences in signal arrival times at both ends of tubes in three of the layers) is also provided. FCB has a similar construction to that of FCA, except in that it is larger in diameter.

2.3.2 Calorimetry

Measurement of the energy of photons, electrons and hadrons takes place in DELPHI's calorimeters.

High Density Projection Chamber

The **High Density Projection Chamber (HPC)** is the electromagnetic calorimeter in the barrel region of DELPHI. The converter consists of lead supported by fibreglass, the drift field being produced by a voltage gradient between neighbouring lead ribbons. Time projection techniques are used to reconstruct the positions of the energy deposits, the z coordinate coming from the drift time, and the $R\phi$ information coming from cathode pads. Trigger information is provided by a layer of scintillators placed in one of the sampling gaps behind about 1/4 of the converter (at about the shower maximum). The calorimeter consists of 144 identical modules, forming 24 sectors in ϕ each divided into 6 in z, and 18 radiation lengths deep.

Forward Electromagnetic Calorimeter

The **Forward Electromagnetic Calorimeter (FEMC)** is the electromagnetic calorimeter in the endcaps of DELPHI. It is a lead glass calorimeter, each endcap having 9064 lead glass blocks 20 radiation lengths deep which are constructed so as to point roughly towards the interaction vertex.

Hadron Calorimeter

The **Hadron Calorimeter (HCAL)** has a similar construction in both the barrel and endcaps of DELPHI. 21 layers (20 in the endcaps) of 5cm thick iron plates alternate with layers of limited streamer mode detectors, giving a total depth of 6 interaction lengths. The detector is segmented into 24 sectors in ϕ, and each sector has a read-out board along its side, on which the pads that pick up the ionisation in the streamer tubes are shaped so that they point toward the interaction vertex. The granularity obtained is 3.75° in ϕ, and 3.0° in θ in the barrel region and 2.62° in the endcaps.

2.3.3 Scintillator Counters

Most of the solid angle in DELPHI is covered by a layer of scintillator counters, which provide fast triggering, in particular for cosmic ray muons and beam halo muons, which are useful for detector studies and alignment. In the barrel region, the **Time of Flight counters (TOF)** are a layer of scintillators just outside the solenoid. As is suggested by the name, timing information from the TOF counters can be used to identify cosmic ray muons, which will have a distinct time of flight across the detector. The **Forward Hodoscope (HOF)** is a single layer of scintillators placed just before the final layer of muon chambers in the endcaps.

2.3.4 Muon Chambers

DELPHI's principal muon identification detectors are drift chambers positioned around the outside of the detector, with one set of modules within the outer part of the Hadron Calorimeter to help distinguish hadronic punch through from genuine muons. The barrel muon chambers will be described in some detail as this is necessary for an understanding of their third level trigger (see Chapter 3).

Barrel Muon Chambers

The **barrel muon detector (MUB)** consists of three layers of muon chamber modules, called the inner, outer and peripheral modules, concentric around the DELPHI z axis. The inner modules have 14 chambers, five of which form a layer of spare chambers, and the outer and peripherals each have seven chambers. The chambers are typically 365cm in length, except where a module has to be cut away for cable or cryogenics ducts, or to make way for the legs of the magnet. The positions of the modules, and chambers within modules are shown in Figure 2.7 Each 15^0 sector is split into two in z - there are two sets of modules, one at positive z and one at negative z. The geometry of the barrel muon chambers is described in detail in [22].

Two views of a typical barrel muon chamber are shown in Figure 2.8 The chambers are drift chambers, using a gas mixture of 88% argon, 5% carbon dioxide and 7% methane and operating in proportional mode. The 50μm anode wire is positioned along the longitudinal axis of the chamber, and has a characteristic impedance of 500Ω, and a signal propagation speed of about $20cm/ns$. The anode is usually held at a voltage of about $6150V$. The cathode consists of long thin copper strips, running along the top and bottom inner surfaces of the chamber. There are thirteen strips on each surface - the central strip takes the full cathode voltage ($\sim 4000V$) and the other strips carry a voltage that is graded to produce a uniform electric field within the chamber. One of the central strips forms a delay line, which is composed of an insulated copper winding with characteristic impedance 600Ω and signal propagation speed of typically $0.5cm/ns$. Signals arriving at the anode cause signals to be induced on the delay line, which propagate to both ends of the delay line. Thus for every hit in the chamber

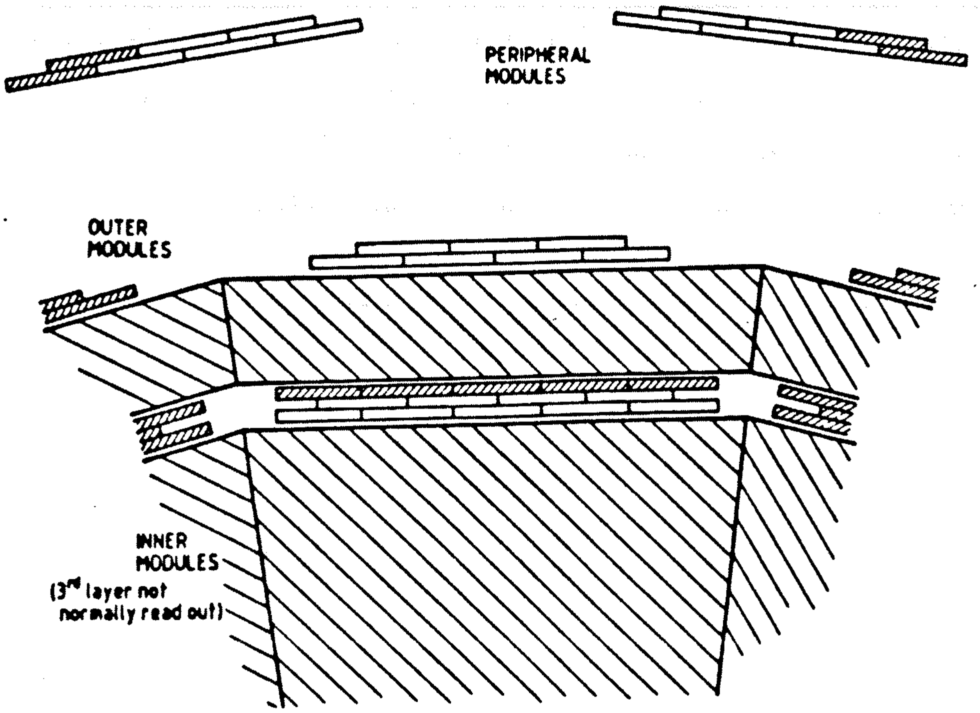

Figure 2.7: A sector of the barrel muon chambers

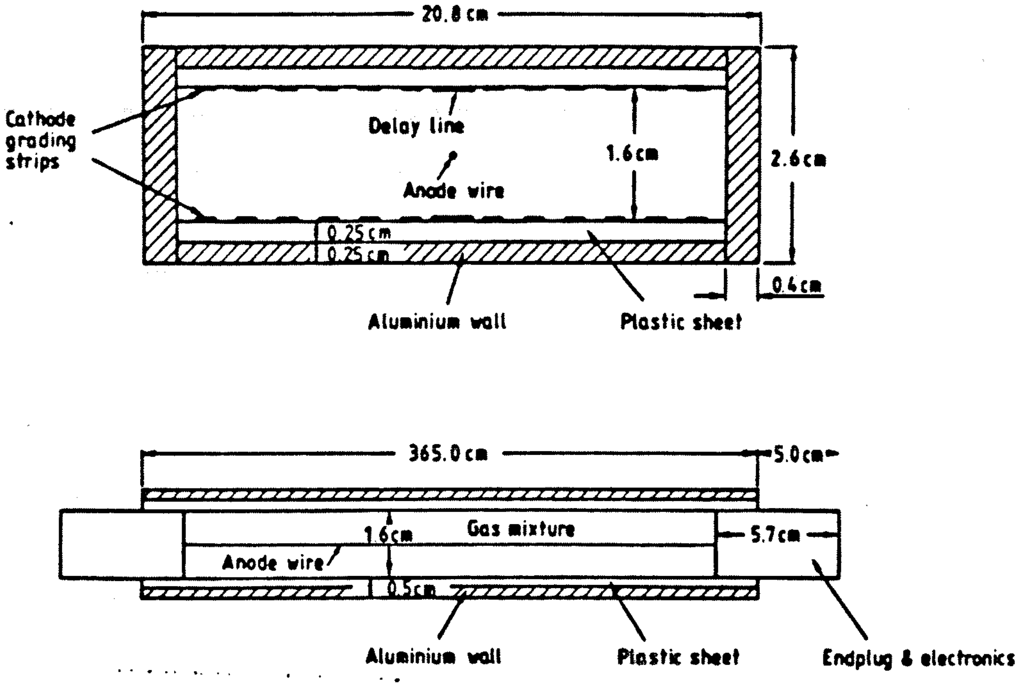

Figure 2.8: Sections through the muon chambers (not to scale).

we should obtain three signals from the chamber - one from the anode, and two from the delay line. When all three signals are present the hit is referred to as a **triplet**, and when one of the delay line signals is missing the hit is referred to as a **doublet**. If there is no anode signal, or no signals from the delay line, no attempt will be make to reconstruct the hit.

For a triplet hit, the times t_n, t_f and t_a should satisfy:

$$t_n + t_f - 2 \times t_a \approx t_{dl}$$

and for a doublet hit:

$$t_{n,f} - t_a < t_{dl}$$

where t_a, t_n and t_f are the arrival times of pulses from the anode wire and near and far ends of the delay line, respectively, and the far end of a chamber is defined to be the end at $z = 0$. t_{dl} is the time taken for a signal to propagate from one end of the delay line to the other. These relationships are used to determine which combinations of times recorded from the chambers correspond to genuine muon hits.

Forward Muon Chambers

The **Forward Muon Chambers (MUF)** are composed of two planes of chambers in each endcap, each plane consisting of two orthogonal layers of drift chambers. The drift chambers operate in limited streamer mode[4], and their overall structure is very similar to that of the barrel muon chambers, though they have both slower drift and delay line velocities, and consequently can not be used in the first level trigger.

---

[4] For more detail on the operation of drift chambers, see [50]

2.3.5 Tables of Detector Characteristics

	Acceptance			No. Points along Track	Resolution per point (σ) (mm)
	R (cm)	$\lvert z \rvert$ (cm)	θ(deg)		
VD (1990)	9/11	12	$37 - 143$	2	$R\phi$: 0.007
VD (1991)	6.3/9/11	12	$28 - 152$	3	
ID:					
jet chamber	$11.8 - 22.3$	40	$17 - 163$	24	$R\phi$: 0.11
trigger layer	$23 - 28$	≤ 50	$30 - 150$	5	$z :< 1$
TPC	$35 - 111$	≤ 134	$20 - 160$	16	$R\phi$: 0.23
				192	z: 0.9
OD	$198 - 206$	≤ 232	$43 - 137$	5	$R\phi$: 0.11
				3	z: 44
MUB	~ 445	≤ 385	$52 - 128$	$2 - 6$	$R\phi$: 1.5
					z: 10
FCA	$30 - 103$	$155 - 165$	$11 - 33$	$2 \times (x, u, v)$	x, u, v: 0.3
FCB	$53 - 195$	$267 - 283$	$11 - 35$	$2 \times (x, u, v)$	x, u, v: 0.25
MUF	$70 - 460$	463	$9 - 43$	$(2 + 2) \times (x, y)$	x, y: 1.0
		500			

Table 2.3: Specifications and performance of tracking detectors.

	Acceptance			Depth
	$R(cm)$	$\lvert z \rvert (cm)$	θ (degrees)	
HPC	$208 - 260$	≤ 254	$43 - 137$	$18X_0$
FEMC	$46 - 240$	$284 - 340$	$10 - 36.5$	$20X_0$
SAT	$10 - 36$	$233 - 285$	$2.5 - 7.7$	$28X_0$
VSAT	$\sim 6 - 9$	770	$5 - 7mrad$	$24X_0$
HCAL (barrel)	$320 - 479$	< 380	$10 - 170$	6λ
HCAL (forward)	$65 - 460$	$340 - 489$		

Table 2.4: Specifications and performance of calorimeters.

2.4 Luminosity Measurement

The **Small Angle Tagger (SAT)** is the principal detector used for measurement of the luminosity in DELPHI. It is a calorimeter composed of cylinders of lead sheet and plastic scintillating fibres concentric with the LEP beam, covering the region between 43.5 and 120mrad. In one endcap, a lead mask 12 radiation lengths deep covering the inner region of the SAT calorimeter was used to define the acceptance of the detector. For the last three-quarters of 1990, and all of 1991, another mask covering the vertical junction between the two half barrels of the SAT (the 'ϕ mask') was also installed. The outer surface of the lead mask was conical, pointing to the nominal interaction point. The dimensions of the ring and ϕ mask were known to better than $100\mu m$, and the position of the SAT relative to the TPC was known to better than 1mm. A tracking detector (the SAT tracker) positioned in front of the SAT is used to help understand the systematics of the detector. The geometry of the lead masks is shown in fig 2.9.

The luminosity analysis was performed by the DELPHI SAT group, and is described briefly below. A good description of the luminosity measurement on DELPHI may be found in [23].

To measure the luminosity, the SAT calorimeter was used to observe the number of small angle Bhabha events N_B. At small angles the cross section for this process is almost entirely dominated by well understood QED processes, with only a small ($\sim 1\%$) electroweak correction. If N_{Bck} is the number of background events, and σ_B is the expected Bhabha cross section within the angular range of the SAT, then the luminosity is given by:

$$\mathcal{L} = \frac{N_B - N_{Bck}}{\sigma_B} \tag{2.1}$$

σ_B was calculated by using the event generator BHLUMI to generate Bhabha events, which were then passed through a detailed detector simulation. The events were generated at the Z^0peak, and then extrapolated to the required energy points assuming the QED $1/s$ dependence of σ_B, and including electroweak corrections.

The efficiency of the SAT trigger was determined to be 100%, using a single arm trigger having a higher threshold than the normal trigger, downscaled to a reasonable rate.

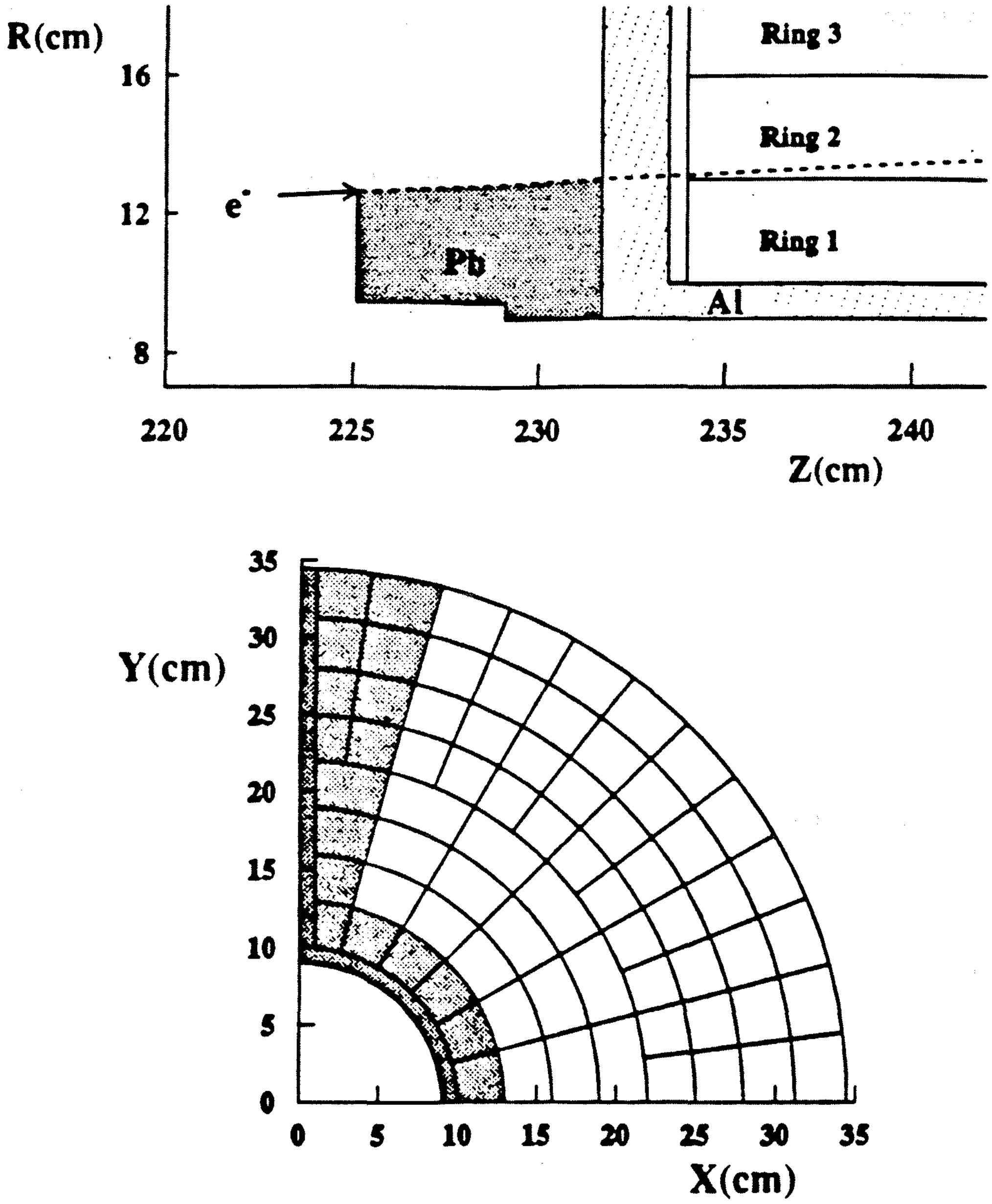

Figure 2.9: The SAT calorimeter - (a) Side view showing the lead mask over the inner ring of the calorimeter, (b) One quadrant of the masked calorimeter, showing the ϕ mask.

The acceptance of the detector was well defined by the lead masks, as electrons passing through the mask could easily be separated from those hitting the SAT directly, as those passing through the mask lost on average 85% of their energy by so doing.

The Bhabha event selection criteria include an energy and acoplanarity cut, and a requirement that the cluster centroids of the two energy clusters were within the fiducial region of the SAT, which was defined by the lead mask at the inner radius, the inner surface of the outer ring of the SAT at the outer radius, and by the ϕ mask. There were also cuts to reject events with abnormally high energy deposits, in regions where this was likely to be due to photons and MIPS from partially contained showers hitting the readout system.

All these cuts introduce small systematic errors into the luminosity measurement, giving a total experimental systematic error in the luminosity determination of 0.6% in 1990, and 0.5% in 1991.

Contributions to the theoretical uncertainty add up to 0.3%, giving a total systematic uncertainty on the luminosity measurement of 0.7% in 1990 and 0.6% in 1991.

2.5 Overview of the DELPHI Trigger System

DELPHI's trigger system was designed to have four levels, to cope with high luminosity and expected high background rates at LEP. For 1990 and 1991 only the first two levels have been used, though for much of 1991, the third and fourth level triggers were running as spectators, producing results which were not used to veto positive second level trigger decisions. During 1991, the first and second level trigger rates were around $500 - 1000Hz$ and $2 - 5Hz$ respectively.

The triggering and data acquisition electronics all conforms to the FASTBUS standard, with one exception called 'The B1 Trigger' which was built for the 1989 run, and is a NIMS trigger handling signals from the scintillators and wire chambers (TOF, HPC scintillators, HOF, ID, OD, FCA, FCB). A full description of the trigger system may be found in [24].

2.5.1 First and Second Level Triggers

The first and second level trigger (T1 and T2) are hardware triggers. Each detector participating in the trigger has a subtrigger module which provides information to the central trigger supervisor module (PYTHIA). This information consists of the number of tracks (0, 1, 2 or more than 2) for tracking detectors, or number of energy clusters above a certain threshold for the calorimeters. One of the inputs to PYTHIA is the B1 trigger. The components of T1 are detectors which can produce trigger decisions within a short space of time, such as the scintillators (TOF, HOF, and HPC scintillators) and wire chambers (ID, OD, FCA, FCB). There are also contributions from HCAL and the TPC FW-BW trigger (see section 2.7.2 for trigger definitions), which provides a low angle track trigger. The T2 decision is made later, when more information from the calorimeters and TPC is available (the longest drift time being $23\mu s$, the maximum drift time of the TPC).

Both T1 and T2 decisions are synchronous with the beam crossover (BCO), i.e. for every BCO, both decisions have to be completed before data from another BCO can be taken. The time between BCOs is $22\mu s$. The T1 decision is taken about $3\mu s$ after BCO - if it is negative, then data acquisition stops, and is started again at the next BCO. If the T1 decision is positive then data acquisition continues and a T2 decision is made $39\mu s$ after BCO, and two BCOs are missed[4]

If the T2 decision is negative, data acquisition is stopped and the electronics is made ready in time for the next BCO, only two having been missed. If T2 is positive then there is a deadtime of about $3.5ms$ (around 160 BCOs) while the front end electronics are freed of the data from this event and prepared for the next.

2.5.2 Third and Fourth Level Triggers

The third and fourth level triggers (T3 and T4) are both software triggers, working asynchronously with the BCO, i.e. there is no holdup in data taking as long as the second level trigger rate does not exceed the rate at which these

---

[4] This was improved to only one BCO after an upgrade of the VSAT electronics in the 1991/1992 shutdown.

triggers can process data, and there is sufficient space to store data from events which are waiting to be processed. T3 and T4 are expected to take around 30ms and 300-500ms respectively for each event.

T3 aims to reduce the trigger rate before data is written to tape, by using all the data from the detectors to make a rough reconstruction of the event, and repeat the T2 logic using this more detailed information - it could also help to prepare information for T4. The MUB contribution to T3 will be described in more detail in Chapter 3.

T4 runs online on IBM 3081 emulators, using results from the previous triggers and consists of a fast event reconstruction to classify events. So far, T4 has been used at the pit to provide an online event display.

2.6 The Data Acquisition System

The data acquisition system is, in principle, very simple - each detector has its own front end electronics modules (time digitisers, multiplexers etc), and one or more Crate Processors (CPs)[6], which control the readout of these modules via FASTBUS in the case of a positive T2 decision, and format the data in an area of memory called the Crate Event Buffer (CEB). Local T3 processing can also take place in the CP. The CPs are controlled by a Local Event Supervisor (LES)[7], which transfers the CEB data into a Multi Event Buffer (MEB), which can store data from up to four events. All the LESs are under the control of a Global Event Supervisor (GES), which transfers the data from each MEB into a Global Event Buffer (GEB), in the case of a positive T3 decision. From the GEB, data is transferred to a VAX 8700 via an optical link, and copied to IBM 3820 cassettes. This transfer is controlled by the CHI (Cern Host Interface). The T4 emulators are between the GES and CHI.

2.7 Triggers for $\mu^+\mu^-$Events

In this section the components of the second level DELPHI trigger which are significant for the $\mu^+\mu^-$channel are briefly described. A general description of

---

[6] Usually the CP is a FIP (Fastbus Intersegment Processor)

[7] The LES software also runs in a FIP

Trigger	θ region covered (degrees)
ID	22-158
IDOD	42-138
TPC CT	29-88, 92-151
TPC RZ	20-43, 137-160
OD	42-138
TOF	41-139
FCA/B	11-33, 147-169
MUB	50-89, 91-130
MUF	15-41, 139-165
HCAL	10-170

Table 2.5: Effective θ regions of the various trigger components relevant to the $\mu^+\mu^-$analysis

the DELPHI trigger can be found in [25], and other useful and more detailed descriptions of individual triggers can be found in [26]. Note that all detectors provide their own first level trigger, except for the TPC Contiguity trigger (CT), which takes any one track in the ID or OD as a first level trigger, and the forward muon chambers, for which HOF provides a first level trigger. The effective θ regions of the trigger components mentioned here are given in table 2.5

2.7.1 B1 triggers

The B1 trigger was the original DELPHI trigger. It was retained in 1991 as a useful cross check of new trigger components, but will be discarded for the 1992 run. In the following descriptions, '$*$' indicates a logical 'AND', and where signals are described as coming from 'back to back' components of the detector, this means back to back through the interaction point.

- IDOD: $\geq$ 1 ID sector $*$ $\geq$ 2 OD sectors. (For the first part of 1990, two back to back OD sectors were required.)
- TOMJ: $\geq$ 2 TOF octants. (For 1990, two back to back octants were required.)
- SCOD: $\geq$ 1 TOF octant $*$ $\geq$ 1 OD sector.

- FWMJ: A Double Majority[8] of single track FEMC, FCA*FCB and ID*OD triggers. (In 1990 HOF was also a component of FWMJ.)
- HOBB: Back to back HOF quadrants.

2.7.2 PYTHIA triggers

The following triggers are sufficient to fire DELPHI alone (They are inputs to Single Majority decision functions of PYTHIA). The prefix 'i' to a trigger name denotes the multiplicity - $i = 1$ for one track, $i = 2$ for ≥ 2 tracks.

- The B1 trigger.
- iIDOD: A barrel single track trigger from correlations between an OD plank, and any of the corresponding three ID sectors.
- iCT0, iCT1: a barrel single track trigger using TPC pad information and a sophisticated track finding algorithm to trigger on tracks with $p_t > 1GeV/c$.
- OD_MJ2_GEO: Two OD planks which are back to back through the interaction point (in the x-y projection) fired.
- TOF_MJ2: ≥ 2 TOF octants fired.
- MUFW2 or MUBW2: ≥ 2 quadrants of MUF firing in one endcap. T1 is HOF.
- TRFW_MJ1 * TRBW_MJ1: Coincidence between the forward and backward single track triggers, each of which triggers on tracks with $p_t > 1.6GeV/c$, for coincidences between FCA and FCB.

The following signals are components of Double Majorities. Only trigger signals with reasonable efficiency for muons are described. Some correlations were not allowed as their rate was too high.

Barrel Majority 2 - any two of components from MUB, TOF, HPC, ID/OD, HAB, where the components are:

---

[8] A Double Majority (majority 2) decision is made when at least two different components of the majority fire. A Single Majority is a simple OR of its components.

- MUB_LLC_MJ1: ≥ 2 hits in any sector of MUB. (Masked with OD and HCAL)
- TOF_MJ1: ≥ 1 TOF octant fired.
- OD_MJ1: ≥ 1 OD sector fired. (Masked with ID_AND_OD and HCAL.)
- ID_MJ1: ≥ 1 ID sector fired. (Masked with everything but MUB.)
- ID_AND_OD: ≥ 1 ID sector $* \geq 1$ OD sector.
- HAMU_BL_MJ1: HCAL trigger with muon threshold corresponding to a charge deposition of 25pC.

Forward Majority 2 - any two of components from TPC, FCA/B, MUF, HAF, FEMC, where the components are:

- TPCFW(BW)_MJ1: a forward single track trigger using a track finding algorithm in the Rz projection.
- TRFW(BW)_MJ1: a forward single track trigger, triggering on tracks with $p_t > 1.6GeV/c$, which is a coincidence between FCA and FCB.
- MUFW(BW)_MJ1: ≥ 1 MUF quadrant fired.
- HAMU_FW(BW): HCAL trigger with muon threshold corresponding to a charge deposition of 25pC.

There is another double majority called the Cross Majority, which correlates forward and barrel trigger signals, but this does not contribute significantly to the $\mu^+\mu^-$trigger efficiency, and so will not be described here.

The Cosmic Trigger is used to take cosmic ray muon data when there is no beam in LEP. This consists of:

- ID_AND_OD: ≥ 1 ID sector $* \geq 1$ OD sector.
- TOMJ2 - ≥ 2 TOF octants, with a 100ns gate.

- TOBB - Back to back TOF octants, with a $2.7\mu s$ gate.

One other important DELPHI trigger remains to be mentioned, and that is **the SAT trigger**, which requires an energy deposit of 10GeV in each SAT calorimeter, the energy deposits being coplanar. To measure the efficiency of this trigger, another trigger requiring 30GeV to be deposited in one endcap alone was also used, downscaled to a reasonable rate.

Chapter 3

Barrel muon chamber Third Level Trigger, and a noise rate calculation for the barrel muon chambers

This chapter contains a brief description of the DELPHI third level trigger (T3), and the MUB local third level trigger algorithm. Following this is a calculation of the noise rate in the Barrel muon chambers. Sections 2.5 and 2.6 may be found useful while reading this chapter.

3.1 DELPHI's Third Level Trigger

The third level trigger (T3) is a software trigger running asynchronously with the BCO (Beam CrossOver), - i.e. unlike T1 and T2, datataking is not stopped while a decision is made. The aim of T3 is to repeat the second level trigger decision using the increased information and time avaliable at third level. Most of the T3 processing takes place in the Crate Processors (CPs), giving one results CEB per CP. These results CEBs are transferred with the rest of the data to the LES FIP, where the Local Trigger 3 Process (LT3P) performs any remaining processing, and produces two output blocklets, one containing only the information necessary for the central third level trigger decision, and one containing more information, for offline monitoring. The decision blocklet (LT3R, for results) is sent to the central third level trigger process, T3, which makes DELPHI's third level trigger decision, and the other blocklet (LT3D, for data) is added to the rest of the detector's data.

The amount of time allowed for T3 processing has been set to be 20ms, assuming a T2 rate of 20Hz. In fact the T2 rate in 1991 was between 2 and 5Hz, so this is a very safe estimate of the amount of time available.

3.1.1 Inputs to the MUB LT3

A simplified diagram of the MUB electronics is shown in figure 3.1. There are two identical sets of electronics, one on the B side and one on the D side of DELPHI, handling signals from the B and D side of the detector.

Each chamber can produce up to 3 signals, one from the anode wire and one from each end of the delay line, as described in Chapter 2. These signals pass from the chambers to the multiplexing unit, which 'ORs' its input channels together in groups of 6, making sure that two signals from the same chamber, or adjacent chambers, are not ORed together into the same output channel. A 6 bit word is produced for each output channel, which indicates on which input channels there were pulses, and this information is passed to the hit latch buffer (HLB), and forms part of the data recorded for each event. Before the multiplexing unit, the anode signals are picked off for use in the first and second level MUB triggers.

The multiplexed signals are fed into the LEP Time Digitisers (LTDs), of which there are 7 in each counting room, and their arrival time is recorded with a resolution of 2.1ns.

The HLB and LTDs sit in a FASTBUS crate, together with a module called the Fastbus Intersegment Processor (FIP), which controls the readout of data from the LTDs and HLB, and the first and second level MUB trigger. When all the data from an event is present in the FIP, the local third level trigger processing takes place. More detailed descriptions of the MUB electronics chain may be found in [27] and [26].

The information available for the third level trigger process is thus:

- The LTD times for any hits that occurred, together with a reference time produced by the LEP BCO signal, recorded for every event.
- Information from the HLB - 6 bits for every LTD channel recording a time, marked with the LTD channel and LTD number, allowing the chamber and signal responsible for the pulse to be deduced.
- The First and Second level MUB trigger decisions, and information on which sectors passed the First and Second level triggers.

Full descriptions of the data formats provided, may be found in [28, 29, 26].

3.1.2 The MUB Second Level Trigger Decision

The MUB first and second level triggers [26] consist of programmable hardware look-up tables, the inputs to which are the anode signals from the chambers. A positive trigger decision occurs if there are two or more anode signals in a sector of the muon chambers as defined in fig 2.7. The look up tables are programmed so that blatantly unphysical combinations of hits are discarded. Signals from one octant (6 sectors - as described in Appendix A) are ORed together, giving a word containing 4 result bits from each side of the detector, available for use by T3. The information on which sector (or sectors) fired T2 is also available for T3.

3.1.3 Overview of the MUB Local Third Level Trigger algorithm (LT3)

The aim of the MUB third level trigger algorithm is to repeat the MUB T2 decision using all the MUB raw data. The extra information available at third level enables MUB T3 to distinguish between noise in the second level trigger (for example noise pulses on an anode channel, which can fire T2 but which have no corresponding delay line pulses) and physical hits in the muon chambers. This is achieved by checking firstly that every anode signal has at least one corresponding delay line signal, and secondly that when such a combination of signals is found, the anode and delay line times satisfy the appropriate timesum test, as described in section 2.3.4. Another possibility is to use the improved resolution provided by the rough Z reconstruction to try and distinguish cosmic ray muons from muons which are produced at the interaction vertex, by looking at the agreement in θ of points within a sector.

Almost all of the MUB T3 processing takes place in the two MUB CPs, the MUB LT3 just combines the results from the two CPs into one blocklet. The MUB T3 process is coded in 'c', a test version is currently running online, producing results but not being used to veto events.

A brief outline of the MUB T3 algorithm is given below, information about the look up tables, numbering systems and data format are given in Appendix A

1. Check the Second level trigger decision - if no sectors passed the T2 logic, the T3 decision is automatically negative.

2. Loop over the LTD data, saving pointers to any times.
3. Loop over the HLB data, where hits are found, demultiplex and store the pointers to the LTD times (from above) for each chamber.
4. Loop over the chambers, if the anode time and at least one of the delay line times is present, perform the appropriate test (see section 2.3.4) and set a hit flag for the chamber if it appears to contain a physical hit.
5. At this point a list of good hits is available, with pointers to the LTD data corresponding to each hit.
6. For each T3 sector, count the number of good hits - if this is ≥ 2, set the appropriate bit in the T3 result word, perform a rough reconstruction of each hit position in θ and ϕ in mrad, and record θ, ϕ, the chamber number and whether the hit was a doublet or a triplet[1].

It is important that T3 reconstructs at least as many muon chamber hits as the offline software, and figure 3.2 shows that this is so.

3.1.4 Rough reconstruction of space points

The ϕ position of each hit point is taken to be the ϕ position of the chamber wire, obtained from a look up table.

The θ position is obtained by first reconstructing Z assuming a linear delay line velocity, and then obtaining θ from a look up table. The entries to the table are

- $Z/4+1$, where Z is the absolute value of Z in cm in the DELPHI coordinate system. The Z bins are thus 4cm wide, θ being given at the midpoint of each bin.
- The module (inner, outer or peripheral) of the chamber, which refers to the approximate radius of the chamber.

---

[1] A hit is called a doublet if the anode time and one of the delay line times are present, and a triplet if all three times are present

- The end of DELPHI at which the chamber is situated - A, C or between the magnet legs. This refers to whether the centre of the chamber is at positive Z, negative Z or Z=0.

Figure 3.3 shows the resolution of this rough reconstruction in θ and ϕ, by taking $\mu^+\mu^-$ events and comparing the reconstructed T3 hits with the track direction. The difference in ϕ between the tracks and T3 hits has been plotted separately for positively and negatively charged tracks. The full width of the $\Delta\phi$ distributions is about 50mrad (corresponding to about 20cm at 445cm, the radius of the inner modules), as would be expected from chambers with a maximum drift distance of 10cm. The σ of the $\Delta\Theta$ distribution is 13mrad, corresponding to a Z resolution of about 5.8cm at 445cm.

3.1.5 The trigger decision

The T3 trigger decision is currently simply a repetition of the T2 decision (two or more hits per sector). However, since T3 regards a 'hit' as a doublet or triplet of signals from a chamber which satisfy the timesum test, and T2 regards a 'hit' as just an anode signal, T3 has the potential to reject events which are just caused by electronics noise. At the moment this would cause a reduction of the T2 rate by a factor of two. Provided the T2 rate does not increase too much, including T3 should keep the MUB trigger rate quite stable.

3.1.6 Future Possibilities

In this section, the use of the improved resolution provided by the rough Z reconstruction will be considered. It might be possible to reduce the trigger rate due to cosmic ray muons by making some requirement on the agreement in θ between points reconstructed by T3, since muons from Z^0decays are produced at the interaction vertex, whereas cosmic ray muons are not. Two possible methods of making such a cut are considered, one using the minimum difference in θ, $\Delta\theta_{min}$, between any two hits in a sector, and one using the total θ range, $\Delta\theta_{max}$, covered by all the hits in a sector. These quantities are defined in fig 3.4, and their distributions are shown in fig 3.5.

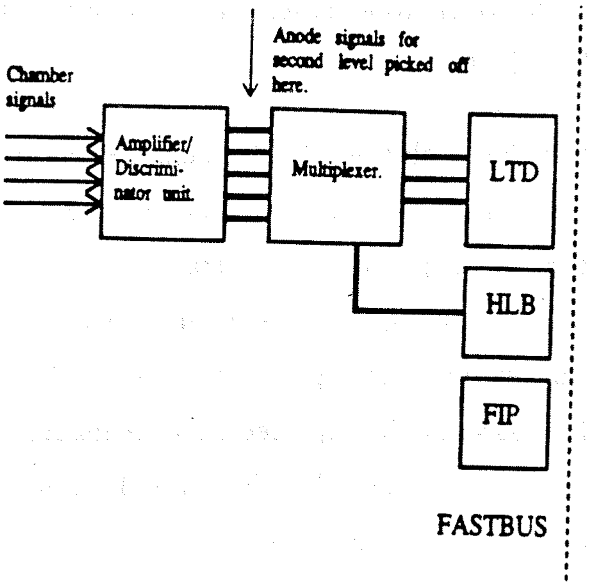

Figure 3.1: Simplified diagram of the MUB electronics

To study the effect of cutting on $\Delta\theta_{min}$ and $\Delta\theta_{max}$, two samples of events were used. The first sample consisted of the raw and TANAGRA data from ~ 500 $\mu^+\mu^-$events selected from the 1990 data, and the second consisted of the raw and TANAGRA data from ~ 500 cosmic ray muon events, taken in a dedicated cosmic ray run with the cosmic trigger (described in chapter 2). Only those events in which there was a positive MUB T2 decision on one or both sides of DELPHI are considered here, so the efficiencies and rejection powers obtained are all relative to the T2 efficiency.

The first plot in figure 3.6 shows the $\mu^+\mu^-$efficiency and the percentage of cosmics failing T3, versus a cut on $\Delta\theta_{min}$. The second plot shows the same quantities versus a cut on $\Delta\theta_{max}$. The efficiency is the percentage of events for which there was a positive T3 decision on one or both sides of DELPHI. A fairly loose cut of 100mrad on $\Delta\theta_{min}$ can be seen to give a reasonable cosmic rejection of $\sim 65\%$, while maintaining the $\mu^+\mu^-$efficiency at $\sim 96\%$. A cut on $\Delta\theta_{max}$ reduces the $\mu^+\mu^-$efficiency by an unacceptable amount for even a small amount of cosmic rejection, and so is not useful.

In conclusion, it can be seen that there is some potential for using the T3 θ reconstruction to reduce the cosmic rate from the MUB triggers.

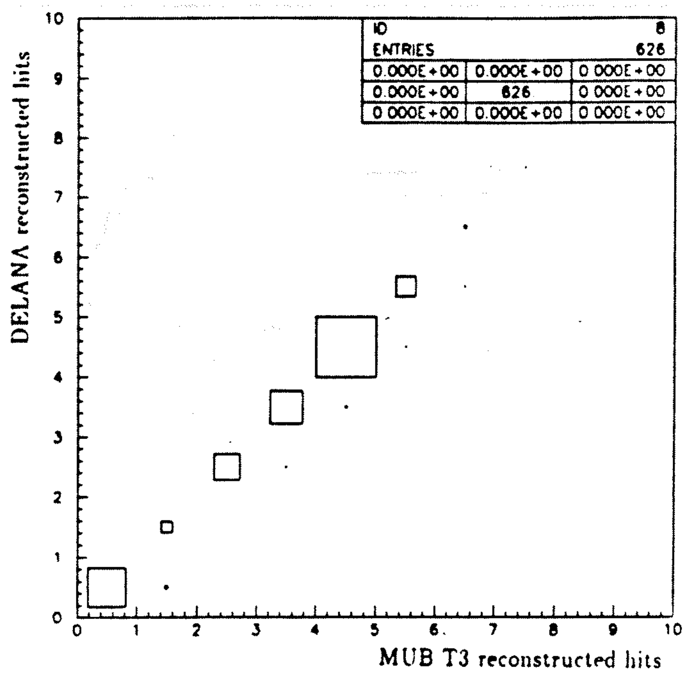

Figure 3.2: Number of hits reconstructed by the T3 algorithm, versus number of hits reconstructed by the offline code (DELANA), for a sample of $\mu^+\mu^-$events.

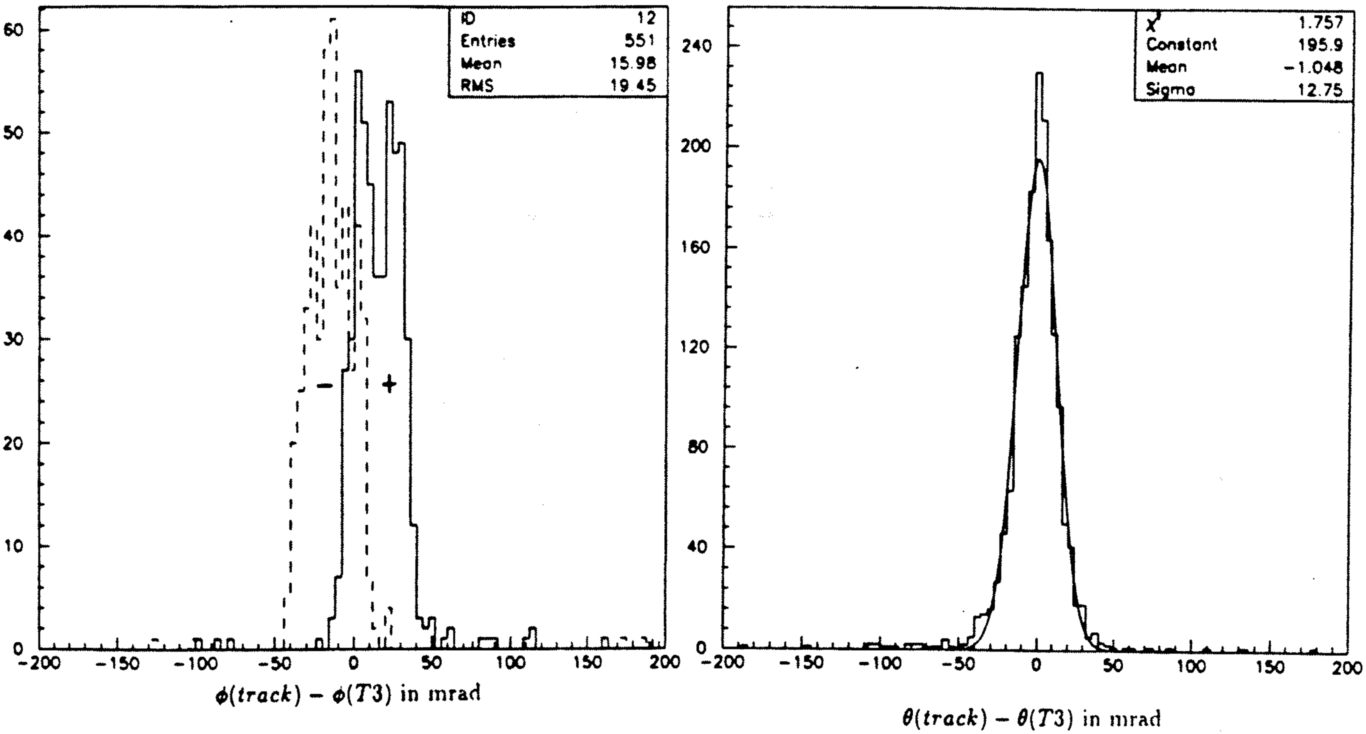

Figure 3.3: First plot - ϕ (T3) - ϕ (track) in mrad, for a sample of $\mu^+\mu^-$events, where '+'and '−' indicate the distributions for positive and negative charged tracks. Second plot - θ (T3) - θ (track) in mrad, for the same sample of events.

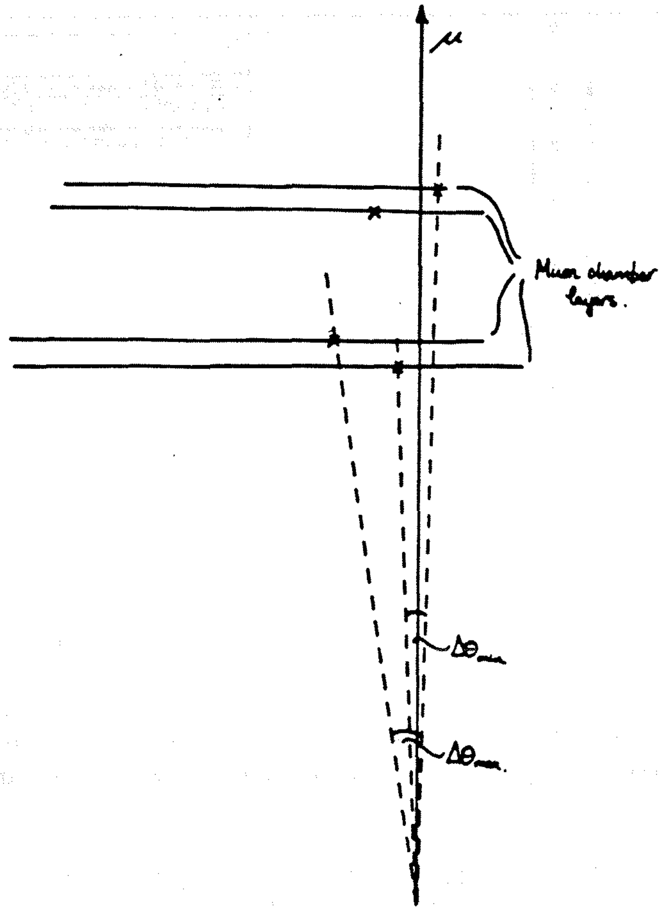

Figure 3.4: Definition of the quantities $\Delta\theta_{min}$ and $\Delta\theta_{max}$

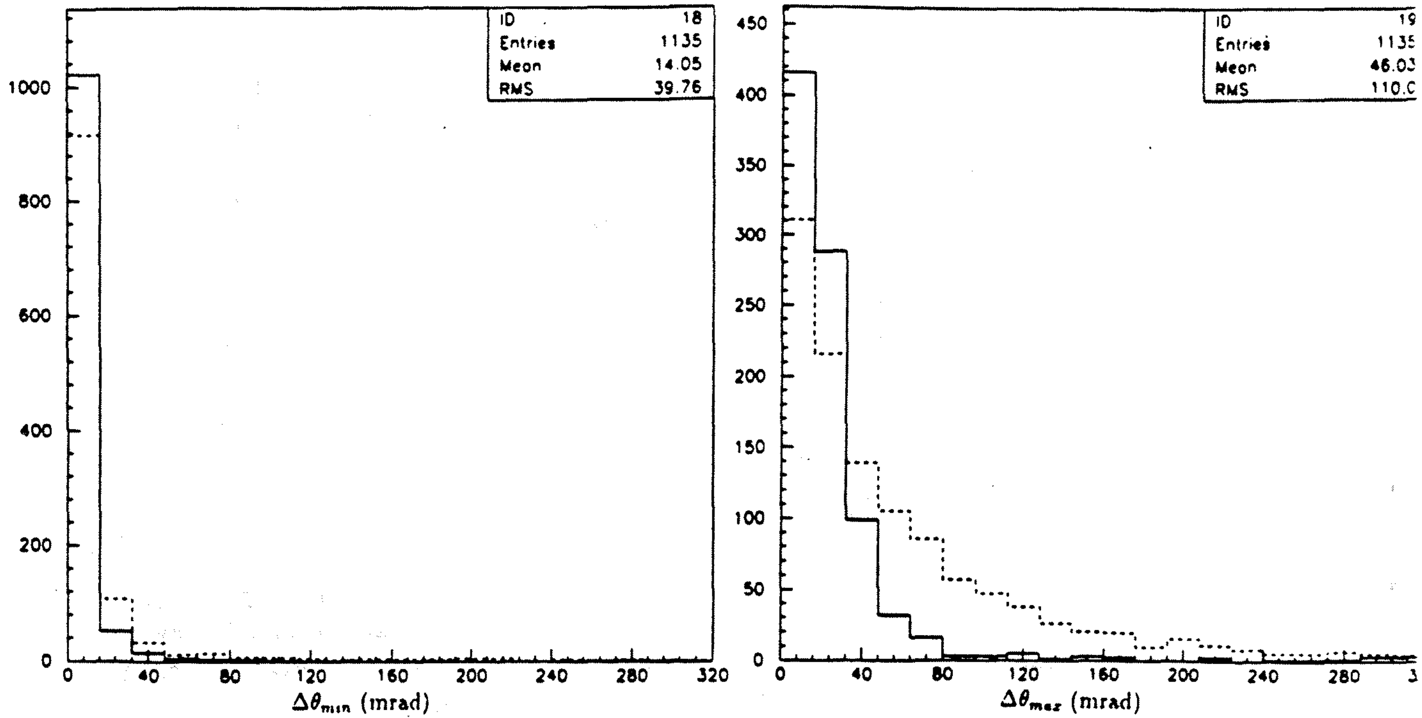

Figure 3.5: $\Delta\theta_{min}$ and $\Delta\theta_{max}$ for $\mu^+\mu^-$and cosmic events

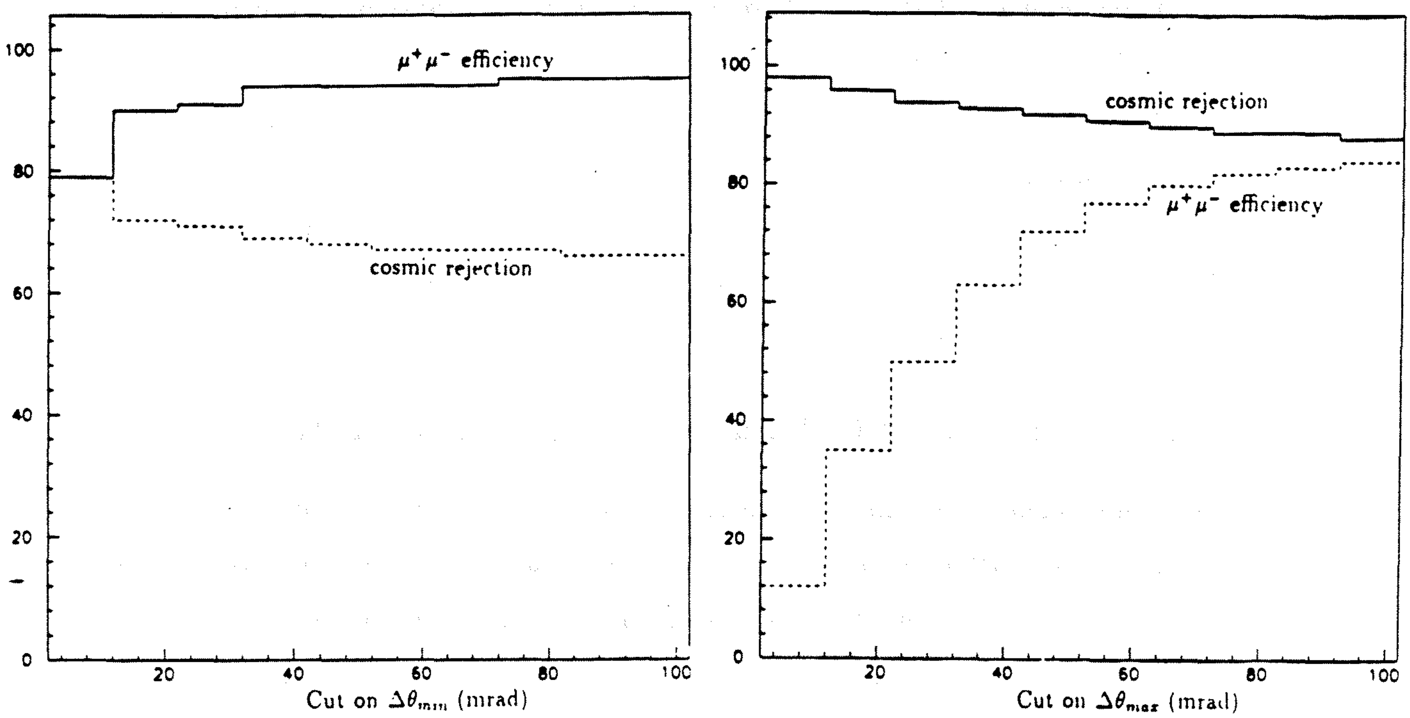

Figure 3.6: First plot - comparison of T3 efficiency for $\mu^+\mu^-$events, and rejection power for cosmic events, for a cut on $\Delta\theta_{min}$. Second plot - as the first plot, but for a cut on $\Delta\theta_{max}$.

3.2 Noise in the Barrel Muon Chambers

One of the problems which must be considered when designing triggers and, later on, when attempting to select certain types of events, is noise in the detectors being used to form the trigger or identify the events. Knowledge of the noise rate in the muon chambers is particularly important when identification of muons in jets is being attempted, since there are many charged tracks with which a noise hit in the muon chambers could be associated.

A noise hit in the MUB is defined as a triplet or doublet of signals from one chamber which may be used to reconstruct a space point, but which is not due to the products of a Z^o decay. There are several possible causes of such noise hits, for example cosmic ray muons, chamber and electronics noise, and beam effects other than Z^o production.

3.2.1 Method of Calculation of the Noise Rate

For the calculation of the noise rate, DST-only data of the leptonic candidates from the July 1991 reprocessing of the 1990 data, and from the April 1991 reprocessing of the 1991 data were used. These data were reduced to form two files (one per year) small enough to fit on disk, for ease of analysis. Standard mupair selection cuts were used to obtain a sample of mupair candidates, with the additional requirement that the MUB was fully operational. Chapter 4 contains more detail on the way the data were processed, and on the cuts used to select mupair events.

Noise hits were then identified by calculating the difference in ϕ between each charged track in the mupair events and any MUB hit points which had not been associated with the tracks by EMMASS, the DELPHI offline code for muon identification [41]. Histograms of this phi difference for the 1990 and 1991 data are shown in Figure 3.7. From these histograms, noise hits were defined as those hits which were beyond 15^o in ϕ (20^o in 1990) from both of the charged tracks. A check was made to avoid double counting when both of the possible space points corresponding to one hit in a MUB chamber were present.

The mean number of noise hits per event was then calculated as follows:

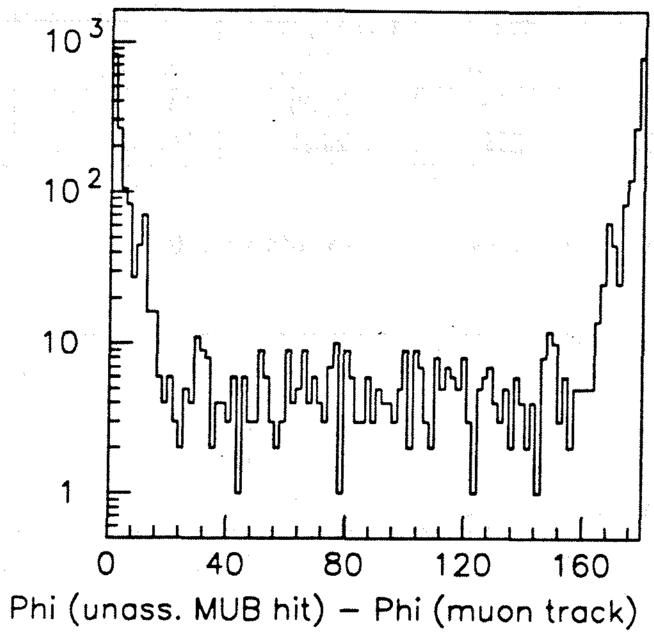

Figure 3.7: ϕ difference between MUB hits unassociated to tracks, and the charged tracks, in $\mu^+\mu^-$events.

$$R = \frac{N_{noise} \times C_\phi}{N_{\mu^+\mu^-}}$$

where R is the noise rate, C_ϕ is the correction factor for the ϕ cut, and $N_{\mu^+\mu^-}$ is the number of $\mu^+\mu^-$events.

Where the correction factor for the ϕ cut was 9/7 for the 20° cut in 1990, and 6/5 for the 15° cut in 1991.

The numbers of events with between 0 and 4 noise hits are given in table 3.1.

To give some idea of the distribution (and so hopefully the cause) of the noise, the number of noise hits in the upper and lower halves of the barrel, and the number of noise hits in the Inner, Outer and Peripheral chambers were recorded separately. These numbers are given in table 3.2, where I, O, P, D and T stand for hits in the inner, outer and peripheral chambers, and for doublet and triplet noise hits respectively. The relative proportions of doublet and triplet noise hits are not significantly different from those for hits associated with tracks. There appear to be more noise hits in the upper than the lower half of DELPHI, and slightly more in the peripheral chambers than in the inner chambers, in both 1990 and 1991. The fact that most of the noise hits are triplets suggests that they are

Year	No. of Mupairs	Total Noise hits	Events with 0 hits	1 hit	2 hits	3 hits	4 hits
1990	2349	158	2200	142	6	0	1
1991	2655	219	2451	195	10	0	1

Table 3.1: Numbers of $\mu^+\mu^-$events with 0-4 noise hits in MUB

Year		$y > 0$	$y < 0$	I	O
1990	Noise hits	95	63	45	55
	Hits/Event	0.052 ± 0.004	0.034 ± 0.003	0.025 ± 0.003	0.030 ± 0.003
1991	Noise hits	138	81	67	64
	Hits/Event	0.062 ± 0.004	0.037 ± 0.003	0.030 ± 0.003	0.0290.003

Year		P	D	T
1990	Noise hits	58	7	151
	Hits/event	0.032 ± 0.003		
1991	Noise hits	88	16	203
	Hits/event	0.040 ± 0.004		

Table 3.2: Numbers of noise hits in different parts of MUB

not electronics noise, but either cosmic ray muons (out of time with the BCO), or possibly background radiation in the cavern.

Chapter 4

Data Analysis

4.1 The Data Sample

For this analysis, a reduced set of data, consisting of all the useful information from events which satisfy some very simple and loose cuts was used. The processing chain which begins with raw data on IBM cassettes at the DELPHI pit, and results in the files used for this analysis, is described below.

4.1.1 Event Reconstruction

The cassettes of raw data are taken from the DELPHI control room to the main CERN site, where they are processed on DELFARM, a group of workstations running in parallel [33].

The raw data is processed by a program called DELANA (DELphi ANAlysis)[34], which produces a detailed reconstruction of each event and outputs this in the TANAGRA (Track ANAlysis and GRAphics package)[35] data structure. The first stage of DELANA involves reconstruction of Detector data (TD) information - space points, energy deposits and times in the subdetectors. Local pattern recognition (clustering of energy deposits in the calorimeters, track reconstruction in the individual tracking detectors) then forms Track Elements (TEs) from the Detector data. Track Elements from the tracking detectors are grouped into Track Strings (TSs), and finally a full track fit resolves ambiguities between the Track Strings and produces a set of Tracks (TKs), each containing a complete set of track parameters from the fit. For the processings of the data used here, the VD information is not included in the fit for the TK.[1] The final level of TANAGRA attempts to gather the TKs into Track Bundles (TBs) which appear

---

[1] The VD information is included in the TK fits automatically for the DELANA_E (early 1992) processing of the 1991 data onwards.

to originate from the same vertex, and then perform a fit to determine both the vertex position and the track parameters at the vertex - this information is stored in TVs. For the $\mu^+\mu^-$analysis only the TKs are used, because the vertex fit is not reliable for two high momentum and nearly colinear tracks.

The Tracks are then extrapolated out to the calorimeters and muon chambers, and a second stage of processing associates energy clusters and muon chamber hits with the tracks.

4.1.2 Data Reduction

A package called PXDST strips down the TANAGRA data to produce DST (Data Summary Tape) data, which contains all the essential information needed for analysis, in a smaller volume than that occupied by TANAGRA data. There are several output streams from this processing, one of which is all of the raw, TANAGRA and DST data for events which have been tagged as 'leptonic' [36].

4.1.3 Leptonic Tagging

To be classified as leptonic, an event must either satisfy the DELANA leptonic tagging criteria, or be tagged by code provided by the analysis teams working on electron, muon and tau pair physics. The aim is to tag all e^+e^-, $\mu^+\mu^-$and $\tau^+\tau^-$events that could possibly be identified by DELPHI, even those which would not be included in an analysis. This is very important because the 'leptonic' raw data may be reprocessed many times, and as the alignment of the detector and the reconstruction code in general is improved, some of the events which have been tagged by the looser criteria may become good lepton pair candidates.

- The DELANA leptonic tagging criteria[37] are summarised in fig 4.1. This tagging starts with the track trigger (TT), and the calorimeter trigger (CT), which aims to save e^+e^-events for which no tracks have been reconstructed. Tracks used by the TT must have impact parameter in $R\phi$ (*Rimpac*) satisfying $Rimpac < 8cm$, and distance of closest approach in Z (*Zimpac*) satisfying $Zimpac < 50cm$. The vertex track trigger (VTT) is the same as the TT, but with tighter vertex constraints $Rimpac < 6cm$ and $Zimpac < 10cm$.

- The tagging code provided by Team 2 (the $\mu^+\mu^-$analysis team) aims to save $\mu^+\mu^-$events - particularly in the forward region - for which no tracks have been reconstructed. There are three levels of tagging code - if an event is tagged by the first level, then it will not be processed by the second and third levels, and so on. If an event has been tagged as leptonic by DELANA then the team 2 code is not used at all. The tagging criteria are briefly described below.

  1. The first level of tagging is a simple topology requirement - an event is tagged if it has at least one and not more than 6 charged tracks, with: momentum greater than $5GeV/c$, impact parameter in $R\phi$ less than $8cm$, and closest approach in z less than $10cm$.
  2. The second level of tagging picks up events where tracks have passed along the sector boundaries of the TPC. Events are tagged if they have 0, 1 or 2 TKs, at least one of which has no TPC information; and there is activity in the Outer Detector behind two back-to-back TPC cracks.
  3. The third level of tagging aims to pick up events in the forward region for which tracks have not been reconstructed in the first processing of the data. The code first looks for 'MUON' and 'TRACK' signals in each endcap, a 'MUON' signal being some combination of information from the three muon identification detectors consistent with having been produced by a muon, and a 'TRACK' signal being evidence of a charged track having been detected in the end cap, i.e. a TK, or a TE in either of TPC, FCA or FCB. An event is then tagged if there is any back-to-back combination of 'TRACK' and 'MUON' signals (within certain cuts in θ and ϕ).

4.1.4 Production of a Leptonic micro-DST

When the cassettes of Raw + Tanagra + DST data of events tagged as leptonic had been produced, the DST data was stripped off and stored stored temporarily on private IBM cassettes. The data on these cassettes were then copied to Exabyte cassettes and taken to Oxford.

To reduce processing time[2], the analysis described in this chapter was

---

[2] from about 2 hours to 20 minutes for all the 1990 leptonic data, on a VAX 3100 workstation

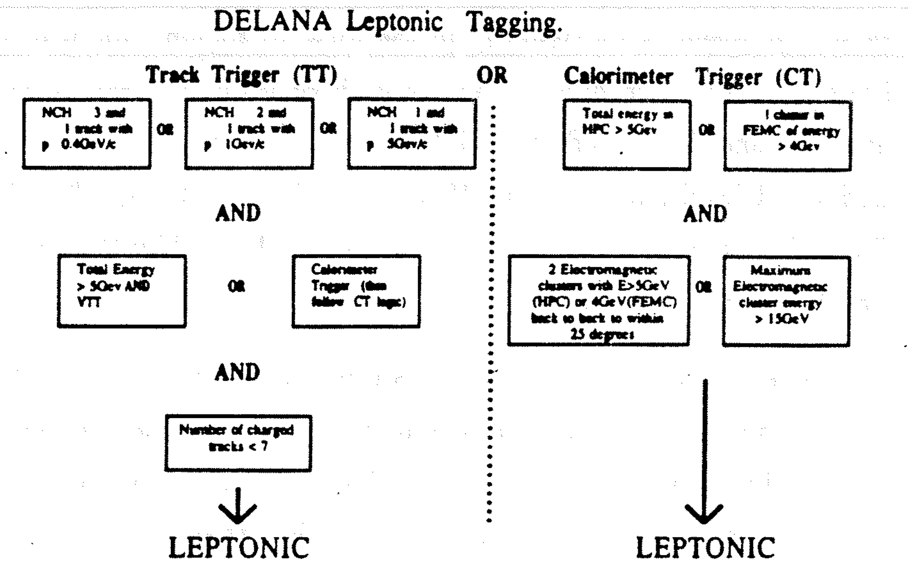

Figure 4.1: DELANA Leptonic Tagging - N_{ch} stands for the number of charged tracks, p stands for the momentum of a track.

performed using a reduced form of the DST data of the leptonics, called a 'micro-DST', which was contained in several data files stored on disk[3]. At the time of creation of the micro-DST, the charged tracks were refitted including the VD information with subroutines from the VDCLAP[4] library. The track perigee parameters (momentum, direction in theta and phi, and impact parameter in $R\phi$ and distance of closest approach in z with respect to the beamspot position) before and after the refit were stored.

Micro-DST information was only stored for events with between 1 and 8 reconstructed charged tracks. This cut includes all those events which could pass $\mu^+\mu^-$identification cuts, and single track events for use in studies of $\mu^+\mu^-$identification efficiencies. The contents of the micro-DST for each event are listed in full in appendix B.

---

[3] The 1991 leptonic DST data used in this thesis occupied 853 Mbyte, whereas the micro-DST of the same data occupied only 49 Mbyte - a reduction factor of 17.5.

[4] Vertex Detector Common Library for All Programs

4.2 The Data Used

For this study, data collected during all of 1990 and the first half of 1991 were used[5], which were processed by DELANA in July 1991. In 1990, LEP ran at 7 centre of mass energies around the Z^0 pole, and for the first half of 1991, all running was at one centre of mass energy close to the Z^0 pole. The simulated data used consisted of:

- 5000 e^+e^-events (generated in the (43°, 137°) region)
- 20000 $\tau^+\tau^-$events generated using KORALZ. For 10000 of these events, the detector simulation corresponded to the period before run 22094, when the HPC MIP efficiency was high. For the other 10000, the HPC MIP efficiency was low, as for the period after run 22094.[6]
- 20000 $\mu^+\mu^-$events generated using DYMU3. Again, 10000 of these events correspond to the period before run 22094, and 10000 to the period after run 22094.

4.2.1 Run Quality Requirements

In this analysis, information from all detectors except the RICHes is used. The status of each detector in DELPHI is recorded run by run, the information being given in the form of a number from 0 to 9. Table 4.1 gives the detector status requirements for this analysis. The statuses 4, 5, 6 and 7 refer to detectors being at 80−90%, 90−95%, 95−99% and $> 99\%$ respectively of their nominal efficiency.

Only data from runs where the statuses of the TPC and OD and at least two (all three for the cross section analysis) of the muon identification detectors (Electromagnetic calorimeters, Hadron calorimeters and Muon chambers) are good is used. The TPC and OD are considered to be essential for good momentum resolution, and at least two of the muon identification detectors are needed in order to be able to calculate the muon identification efficiency. In addition, for the cross section analysis the SAT status is required to be good.

---

[5] This corresponds to runs 7419 (April 23rd 1990) to 23545 (end of June 1991).

[6] Between runs 22093 and 22094, the HPC drift voltage was lowered by 100V, in order to slow down the ageing of the detector.

Detector	SAT	TPC	OD	HPC/FEMC	HCAL	MUB/MUF
Status	6-7	6-7	6-7	6-7/6-7	6-7	6-7(1990), 4-7(1991)/6-7

Table 4.1: Detector status requirements for the $\mu^+\mu^-$analysis

4.3 Characteristics of $\mu^+\mu^-$Events

We expect a $\mu^+\mu^-$event to have two charged tracks, each having energy approximately equal to the beam energy, and being almost back-to-back. As a $45GeV/c$ muon is minimum ionising and not strongly interacting, it should leave small energy deposits all the way through both electromagnetic and hadron calorimeters, and also hits in the muon chambers, which are positioned outside the hadron calorimetry. A muon from a $\mu^+\mu^-$event in the barrel region of DELPHI, reconstructed by DELANA and displayed by the DELPHI graphics package DELGRA is shown at the end of this chapter. There are three main backgrounds to $\mu^+\mu^-$events - certain categories of $\tau^+\tau^-$events, cosmic ray muons and e^+e^-events. Other backgrounds are $e^+e^-\rightarrow e^+e^-\mu^+\mu^-$ events (two photon events in which the $e^+e^-$is lost down the beampipe) and beam-gas events.

$\tau^+\tau^-$events. Tau leptons decay primarily into one (86%) or three (14%) charged particles plus a tau neutrino and possibly one or more other neutral particles[39]. The resulting charged particles are usually pions, muons or electrons (approximately 57, 21, and 21 % respectively in the one-prong decays, and ~ 100% pions in the three-prong decays). As the topology of these events is similar to that of $\mu^+\mu^-$events, and occasionally pions can simulate muons, $\tau^+\tau^-$events can form a significant background to $\mu^+\mu^-$events. However, the charged particles in a $\tau^+\tau^-$event tend to have lower momentum than those in a $\mu^+\mu^-$event since the additional neutral particles take some of the available momentum, and for the same reason, the acolinearity of the first two charged tracks in a $\tau^+\tau^-$event will tend to be larger than that of a genuine $\mu^+\mu^-$.

If a **Cosmic Ray Muon** passes through the detector at around the beam crossover time, and close to the interaction vertex, then it can simulate a $\mu^+\mu^-$event.

The topology of **Bhabha Events** is exactly the same as that of $\mu^+\mu^-$events, and so they can occasionally simulate $\mu^+\mu^-$events. (For example if they are not identified in the electromagnetic calorimetry, and there is a fake muon signal in the muon chambers.)

When choosing the event selection criteria, the following points have to be borne in mind:

1. The efficiency for genuine $\mu^+\mu^-$events should be as high as possible.
2. The efficiency for background events should be as small as possible.
3. Cuts should be made in regions where the agreement between real and simulated data is reasonably good and stable.

i.e. all corrections that have to be made to the sample should be small and well understood.

4.4 Event Selection Criteria - Track Cuts

The first cuts applied to the leptonic data sample are topology requirements. After these cuts the sample contains mainly $\mu^+\mu^-$and e^+e^-events, with some $\tau^+\tau^-$events and cosmic ray muons.

Table 4.2 summarises the track cuts used - the first, second, third etc charged tracks are taken to be the charged tracks of highest, second highest etc momentum in the event. Cuts labelled with a σ apply only to events selected for a cross section calculation, and cuts labelled with A_{FB} apply only to events selected for the asymmetry calculation.

C1-C5 and **MU** are the cuts used to select the events used in the analysis, **C1H, C2H** and **C4H** are harder versions of **C1, C2** and **C4** used to increase the purity of samples of $\mu^+\mu^-$events to study the effects of cuts, when knowledge of the absolute efficiencies is not necessary. **C2S** and **C4S** are soft momentum and acolinearity cuts, used to reject beam-gas events. The plots in this section use data from a period having roughly constant tracking, muon identification and trigger efficiencies. This period starts with run 12866 in 1990, after which the TPC triggers were installed, and ends with run 22094 in 1991, when the HPC voltage was lowered, resulting in a lower efficiency for MIPs.

C1	The number of charged tracks N_{ch} satisfies $2 \leq N_{ch} \leq 5$
C2	The first two charged tracks must have $p > 20GeV/c$.
C3	The impact parameter in $r\phi$ ($Rimpac_{1,2}$), and Z at the perigee ($Zimpac_{1,2}$) of the first two charged tracks satisfy: $\mid Rimpac_{1,2} \mid < 1.5cm$, $\mid Zimpac_{1,2} \mid < 4.5cm$ and $\mid Zimpac_1 - Zimpac_2 \mid < 4.0cm$. If a track has associated VD hits the impact parameter cut for that track is $0.4cm$.
C4	The acolinearity of the first two charged tracks must be less than 10°.
C5σ	The negatively charged track must have $43° < \theta < 137°$ (1990), or $28° < \theta < 152°$ (1991).
C5A_{FB}	The negatively charged track must have $22° < \theta < 158°$.

C1H	$N_{ch} = 2$
C2S	The first and second charged tracks must have $p > 5GeV/c$.
C2H	The first charged track must have $p > 40GeV/c$, and the second must have $p > 20GeV/c$.
C4S	The acolinearity of the first two charged tracks must be less than 90°.
C4H	The acolinearity of the first two charged tracks must be less than 0.5°.
MU	Both of the first two charged tracks satisfy one of MU1, MU2 and MU3 (see section 4.5.5).

Table 4.2: Track cuts for the $\mu^+\mu^-$analysis. **C1-C5** and **MU** are the final cuts used to select $\mu^+\mu^-$events, **C1H**, **C2S**, **C2H** and **C4H** are alternative cuts which were used to study where to place **C1-C5**.

4.4.1 C1: Number of charged tracks.

We do not use events with only one charged track, as the extra complications involved outweigh any gain in statistical error. More than two charged tracks can arise in case of conversion of radiated photons, and there is an upper limit of 5 charged tracks to avoid contamination from $\tau^+\tau^-$events and hadronic Z^0 decays. The percentage of $\mu^+\mu^-$events rejected by the requirement that the number of reconstructed charged tracks is no more than 5 is estimated from simulation data to be $(0.13 \pm 0.04)\%$.

Since the momentum of a conversion electron or positron is expected to be rather low, a potential method to reduce the $\tau^+\tau^-$background would be to make a cut on the momentum of a third charged track, if one existed. Figure 4.2 (a), (b) and (c) show respectively the momenta of the third charged track in simulated $\mu^+\mu^-$, simulated $\tau^+\tau^-$and real data events (with the sum of the simulated $\mu^+\mu^-$plus $\tau^+\tau^-$spectrum for comparison) passing cuts C1 - C5σ and MU. Both the simulated $\mu^+\mu^-$and $\tau^+\tau^-$events have a peak at low values of the momentum (less than $1GeV/c$) but the spectrum for the $\tau^+\tau^-$events shows a bump at around $7GeV/c$ and a longer tail at high momenta. From these plots, it looks as though a cut at $5GeV/c$ could provide reasonable $\tau^+\tau^-$rejection without losing too many mupairs. The fraction of events lost when this cut is included with the standard cuts is $(1.3\pm0.2)\%$ in the data, and $(0.8\pm0.1)\%$ in an equivalent set of simulated data consisting of the micro-DST of 10000 $\mu^+\mu^-$and 10000 $\tau^+\tau^-$events. Unfortunately these numbers do not agree particularly well, and even assuming the simulation data can be trusted, including the cut on the third charged track loses $(0.6\pm0.1)\%$ of mupairs and only reduces the $\tau^+\tau^-$background from $(2.0\pm0.1)\%$ to $(1.8\pm0.1)\%$. Thus no cut will be imposed on the momentum of a third charged track.

4.4.2 C2: Momentum cuts.

We make a momentum cut in order to reduce the backgrounds from beam-gas, $\tau^+\tau^-$and two photon events, and cosmic ray muons.

Fig 4.3 shows the momentum spectra for simulated $\mu^+\mu^-$, $\tau^+\tau^-$and real cosmic events, passing cuts C1, C3, C4, C5σ and MU. (The cosmic events were

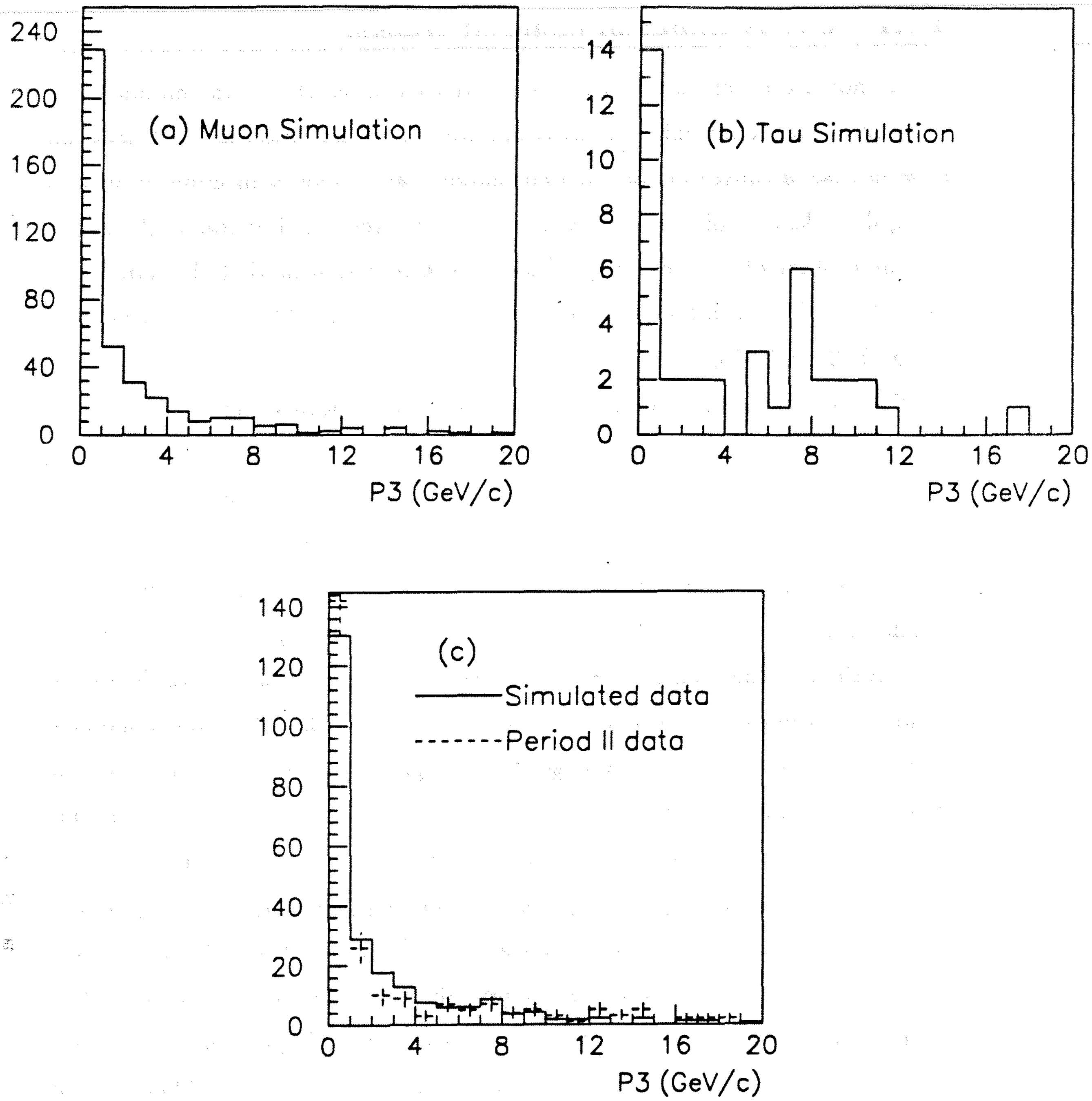

Figure 4.2: (a)+(b) - Momentum spectrum of the third charged track in simulated $\mu^+\mu^-$and $\tau^+\tau^-$events, respectively. (c) - Momentum spectrum of the third charged track in $\mu^+\mu^-$candidates in real data (error bars), with the sum of the simulated $\mu^+\mu^-$and $\tau^+\tau^-$spectra (solid line).

selected from the data using the same cuts, with the additional requirement that the event was identified as a cosmic ray muon using the vertex detector). It can be seen that the tracks in $\mu^+\mu^-$events have a momentum spectrum which peaks at around the beam energy E_b, with a radiative tail below E_b and a tail due to the momentum resolution above E_b. The tracks in $\tau^+\tau^-$and cosmic events tend to have much lower momentum, with the $\tau^+\tau^-$spectrum cutting off at around E_b, though the cosmic spectrum has a long tail up to very high energies. It is clear that cutting on the momenta of the first two charged tracks could significantly reduce backgrounds while losing very few genuine mupairs.

In (c), the areas of the histograms have been normalised to 1, exaggerating the importance of the $\tau^+\tau^-$and cosmic contributions, which are in fact very small (of the order of 1-2% and 0.5% respectively for this analysis - see Sections 4.8.1 and 4.8.2)

Figs 4.4 (a) and (b) show the momentum and charge/momentum of the first two charged tracks in events which have been selected from the data using C1, C2S, C3, C5σ and MU - the $\tau^+\tau^-$background to these events is estimated from simulated data to be $(9.8 \pm 0.3)\%$. It can be seen that a cut of $20GeV/c$ on each track should reject very few events.

It is important to be sure that at this value of the momentum cut, the corrections for $\tau^+\tau^-$background and $\mu^+\mu^-$loss are reasonably well known. To investigate these corrections, events were selected from the data using cuts C1, C2S (a very loose momentum cut was applied to remove beam-gas events from the data), C3, C4S, C5σ and MU - C4 was not used, as momentum and acolinearity are not independent, and so the momentum cuts should be justified before consideration of the acolinearity cut. This sample of events should contain only $\mu^+\mu^-$and $\tau^+\tau^-$events, with negligible background. An equivalent set of simulated data was created by applying the same cuts to 10000 events each of simulated $\mu^+\mu^-$and $\tau^+\tau^-$events (lepton universality is assumed). The fraction of events that would be lost from each sample for a certain momentum cut can then be calculated. Fig 4.5 (a) plots the fraction of data that would be lost from each sample versus momentum cut applied to both the two highest momentum charged tracks. The agreement between the real and simulated data is not very

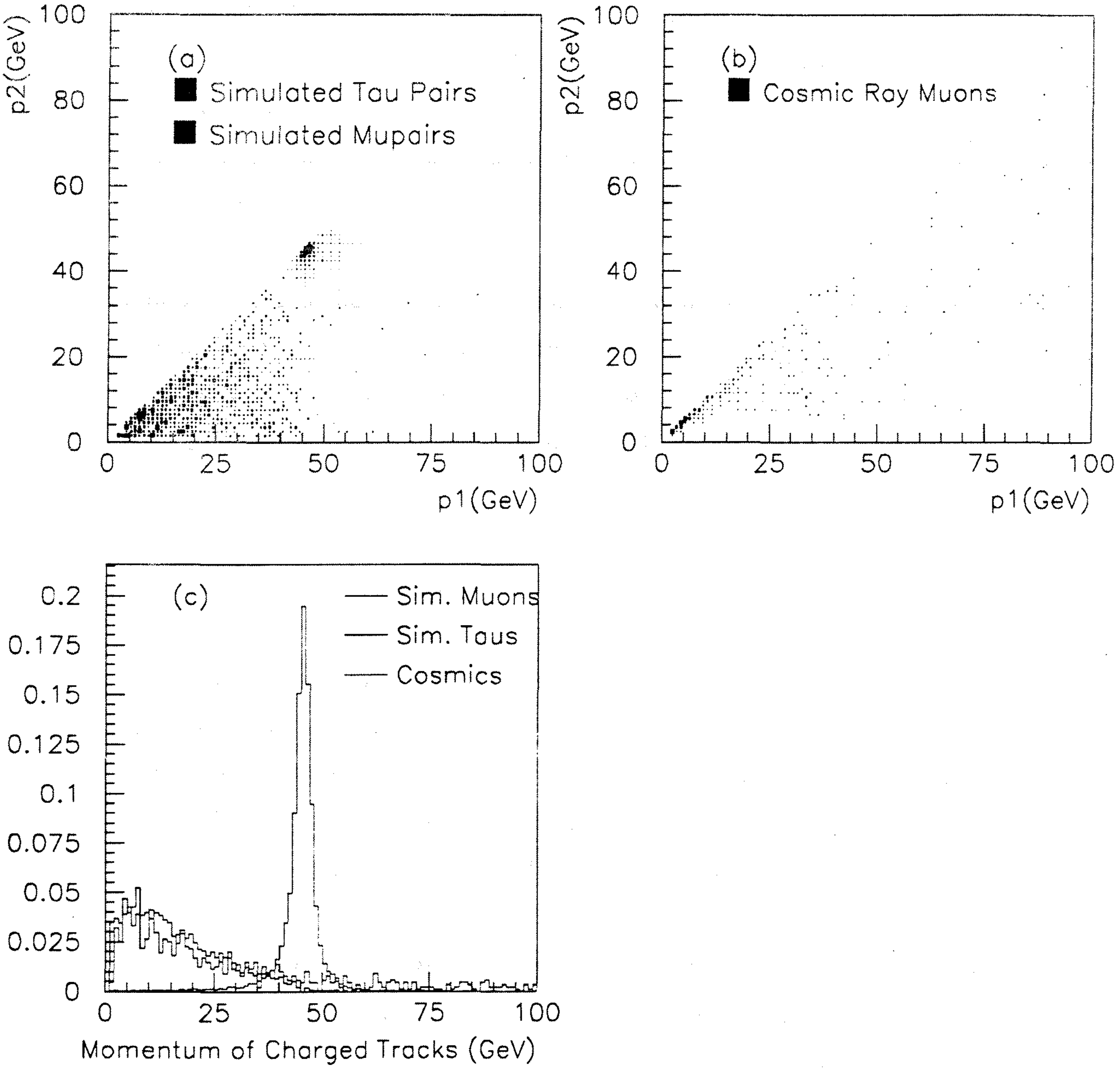
(a)
■ Simulated Tau Pairs
■ Simulated Mupairs
p2(GeV)
p1(GeV)
0
20
40
60
80
100
0
25
50
75
100
(b)
■ Cosmic Ray Muons
p2(GeV)
p1(GeV)
0
20
40
60
80
100
0
25
50
75
100
(c)
Sim. Muons
Sim. Taus
Cosmics
0
0.025
0.05
0.075
0.1
0.125
0.15
0.175
0.2
0
25
50
75
100
Momentum of Charged Tracks (GeV)

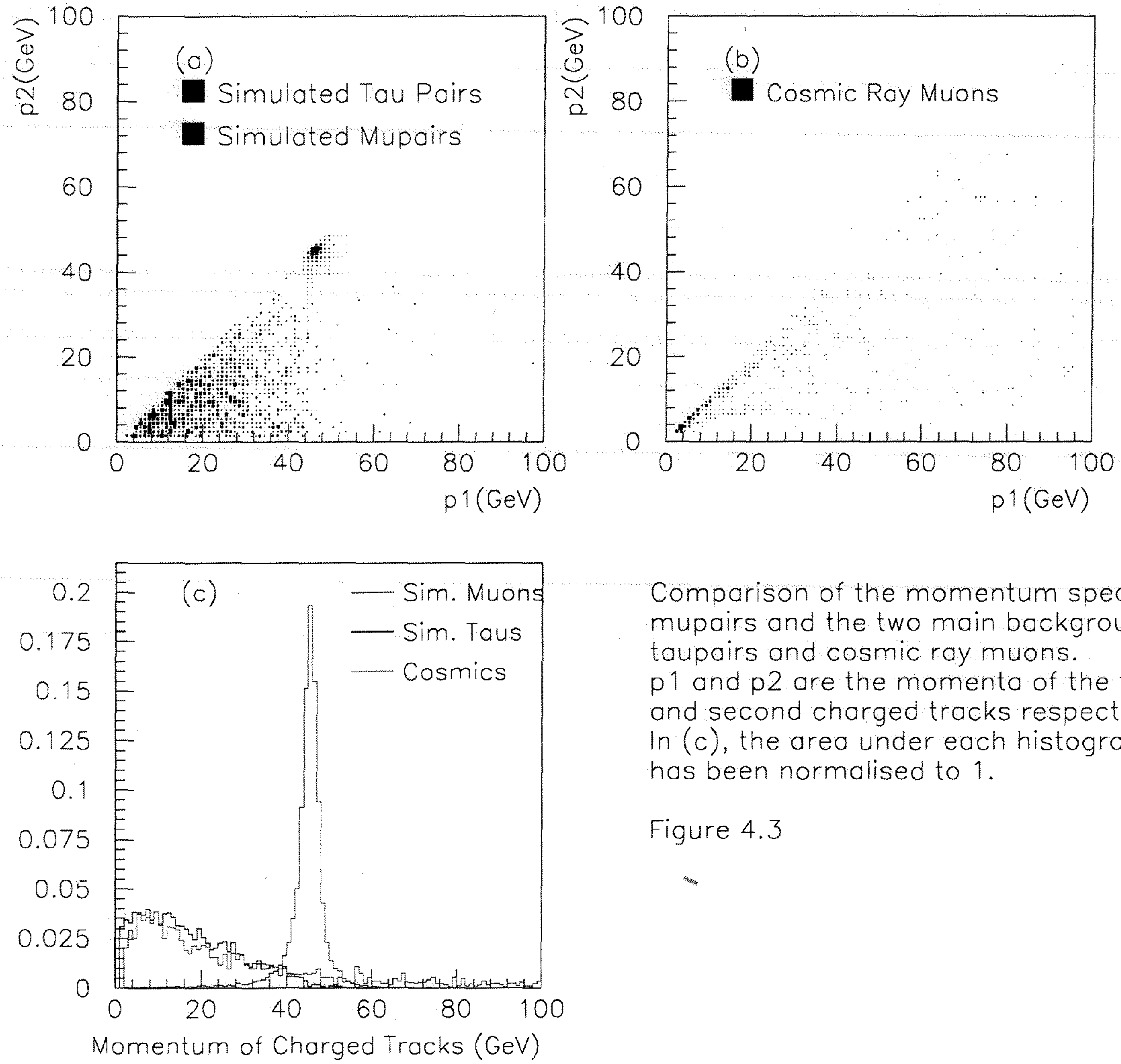

Comparison of the momentum spectra of mupairs and the two main backgrounds, taupairs and cosmic ray muons. p1 and p2 are the momenta of the first and second charged tracks respectively. In (c), the area under each histogram has been normalised to 1.

Figure 4.3

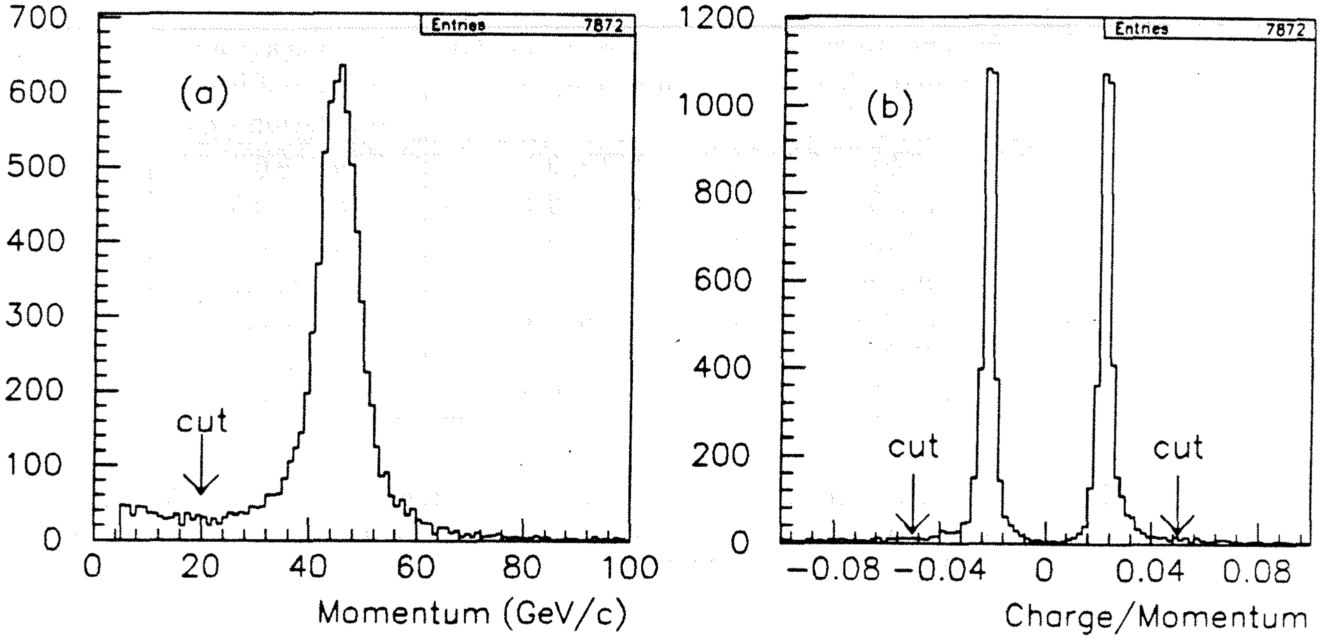

Figure 4.4: (a) Momentum and (b) charge/momentum of the first two charged tracks in events which satisfy all $\mu^+\mu^-$selection criteria but the momentum and acolinearity cuts. (data)

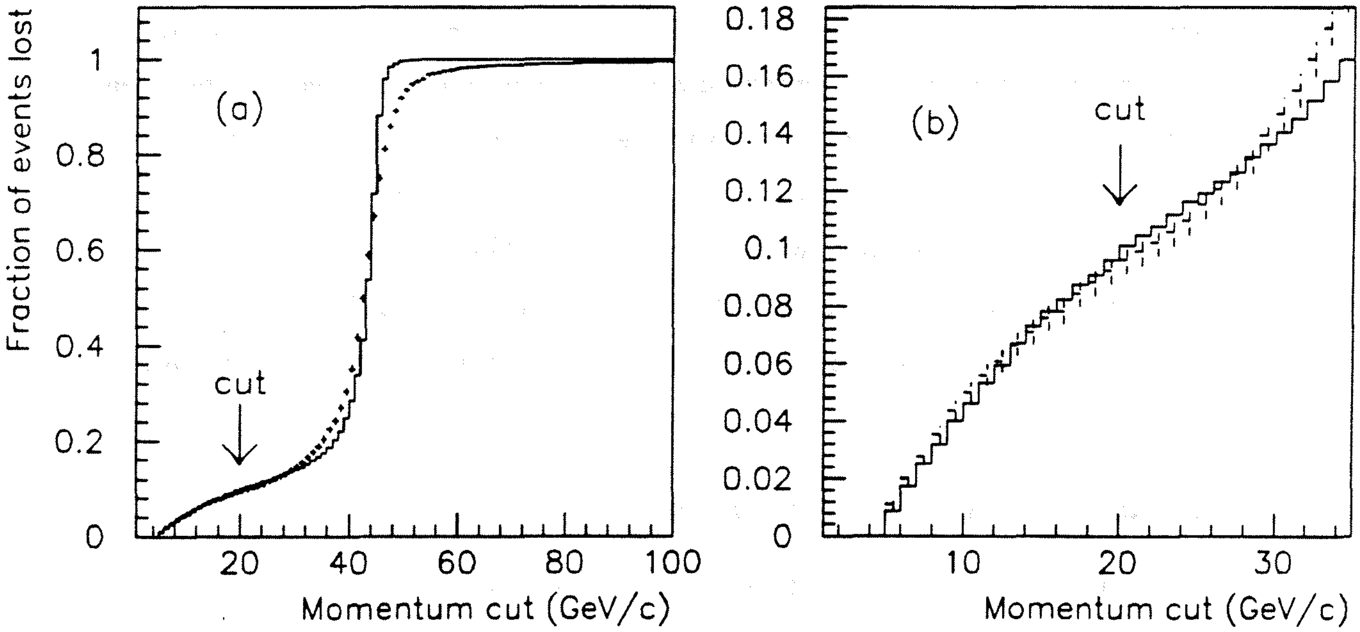

Figure 4.5: Fraction of events lost versus momentum cut on the first two charged tracks for real data (error bars), and simulated 1990 data (solid line). Events selected using C1, C2S, C3, C5σ and MU. a) shows the range up to a 100GeV cut, b) shows the lower part of a) in more detail.

Momentum cuts (on first, then second charged track)	$\mu^+\mu^-$ loss estimated from simulation (%)	$\tau^+\tau^-$ background estimated from simulation (%)
(5,5)	0.2 ± 0.1	9.8 ± 0.3
(10,10)	0.6 ± 0.1	6.4 ± 0.3
(15,15)	1.2 ± 0.1	3.7 ± 0.2
(20,15)	1.2 ± 0.1	3.5 ± 0.2
(20,20)	1.9 ± 0.1	1.9 ± 0.2
(25,20)	1.9 ± 0.1	1.7 ± 0.1
(25,25)	3.0 ± 0.2	0.9 ± 0.1

Table 4.3: Estimated percentage loss of mupairs, and remaining $\tau^+\tau^-$background, for simulated data at varying values of the momentum cut, where the other cuts used are C1, C3, C4S, C5σ and MU. The errors are statistical only.

good for higher energies, as the momentum resolution of the detector is not very well reproduced by the simulation. However, at lower energies the agreement improves - fig 4.5 (b) shows the region between 0 and $30GeV/c$ in greater detail - and at $20GeV/c$, the loss of events is calculated to be $(9.2 \pm 0.5)\%$ in the real data and $(9.6 \pm 0.3)\%$ in the simulated data, where the errors are statistical[6].

As these values for the correction are consistent, and the agreement between data and simulation is stable around the region of the cut, it is concluded that a cut of $20GeV/c$ on the first two charged tracks can safely be corrected for using simulated data. Table 4.3 shows the estimated $\mu^+\mu^-$loss and $\tau^+\tau^-$background for varying values of the momentum cut, when all other cuts but the acolinearity cut are standard, and assuming zero loss due to momentum cut for a cut of $1GeV/c$ on both tracks.

4.4.3 C3: Vertex constraint.

The requirement that the first two charged tracks should both appear to come from the beamspot rejects most of the background due to cosmic ray muons. Fig 4.6 (a) and (b) show the impact parameter (*Rimpac*) and Z at the perigee (*Zimpac*) (both relative to the beamspot position) of charged tracks in events passing all cuts but the vertex cut, where the impact parameter of a track is

---

[6] Note that this loss is almost entirely $\tau^+\tau^-$events!

defined as its distance of closest approach to the beamspot in the $x-y$ plane, and the distance of closest approach in Z is defined at the same point. Fig 4.6 (c) shows $Zimpac_1 - Zimpac_2$ versus $Zimpac_1$. The beamspot position for each run was obtained from a file provided by the VD group, using VD information and tracks from hadronic events. Requiring each track to have $Rimpac < 1.5cm$ and $Zimpac < 4.5cm$ should include all of the genuine mupairs, and some out-of-time[7] cosmics are rejected by the requirement $Zimpac_1 - Zimpac2 < 4.0cm$.

When there are hits in the vertex detector associated with a track, then the precision of its impact parameter may be improved dramatically from that given by the standard track fit results. Fig 4.7 shows the distribution of impact parameters for such tracks before and after the VD refit for $\mu^+\mu^-$events selected from the 1990 data, showing that the refit reduces the σ of the distribution from $350\mu m$ to $120\mu m$. Thus if the beamspot position is good[8], the impact parameter cut is reduced from $1.5cm$ to $0.4cm$ for tracks having associated VD hits, (for both 1990 and 1991 data).

The percentage of muon tracks within the angular range of the vertex detector ($37° < \theta < 143°$ in 1990 and $28° < \theta < 152°$ in 1991) which have one or more associated vertex detector hits was 86.0% in 1990, when there were two VD layers, and 99.5% in 1991, when there were three VD layers.

4.4.4 C4: Acolinearity cut

The acolinearity of two particles with momenta $\mathbf{p}_1^\mu$ and $\mathbf{p}_2^\mu$ is defined by

$$acol = 180.0 - \arccos\left(\frac{\mathbf{p}_1^\mu \cdot \mathbf{p}_2^\mu}{|\mathbf{p}_1^\mu|\ |\mathbf{p}_2^\mu|}\right) \tag{4.1}$$

As the acolinearity distribution for genuine $\mu^+\mu^-$events is expected to be very strongly peaked at small angles, the ratio of genuine $\mu^+\mu^-$to background events might be expected to decrease at high acolinearity angles. One possible background is $\mu^+\mu^-$events from two-photon interactions, another is $\tau^+\tau^-$events,

---

[7] Cosmic ray muons which pass through DELPHI a long time either side of the BCO time, so that even if they pass close to the beamspot, the Z positions of the tracks are offset in opposite directions in the TPC.

[8] 'Good' means beamspot quality '0' in the beamspot file - there are some runs which are assigned average beamspot positions, because for some reason a precise value could not be calculated

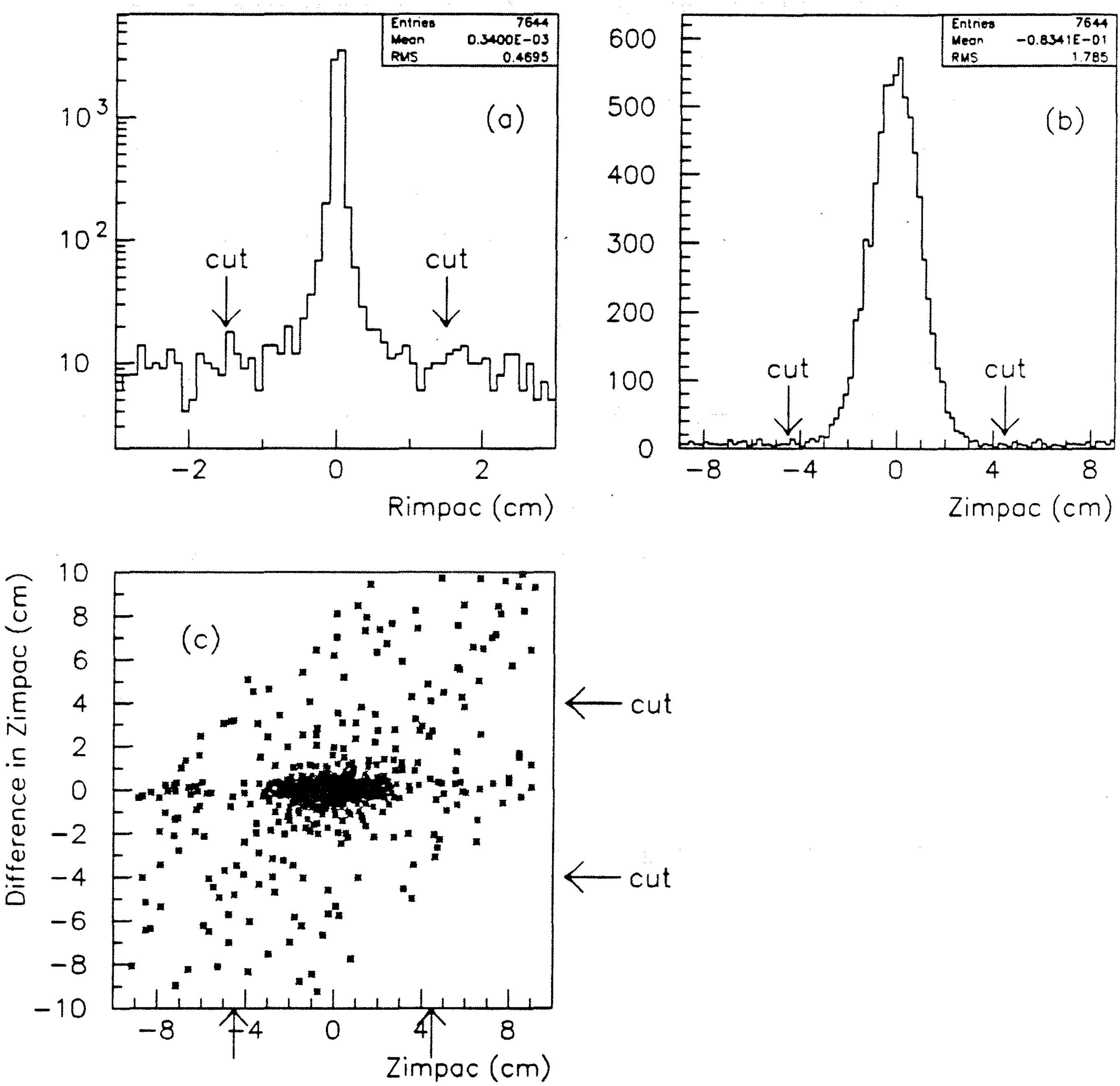

Figure 4.6: Impact parameter (plot (a)), distance of closest approach in z at the perigee (plot (b)), and difference in Zimpac between the first and second track versus Zimpac of the first track (plot (c)), relative to the beamspot position

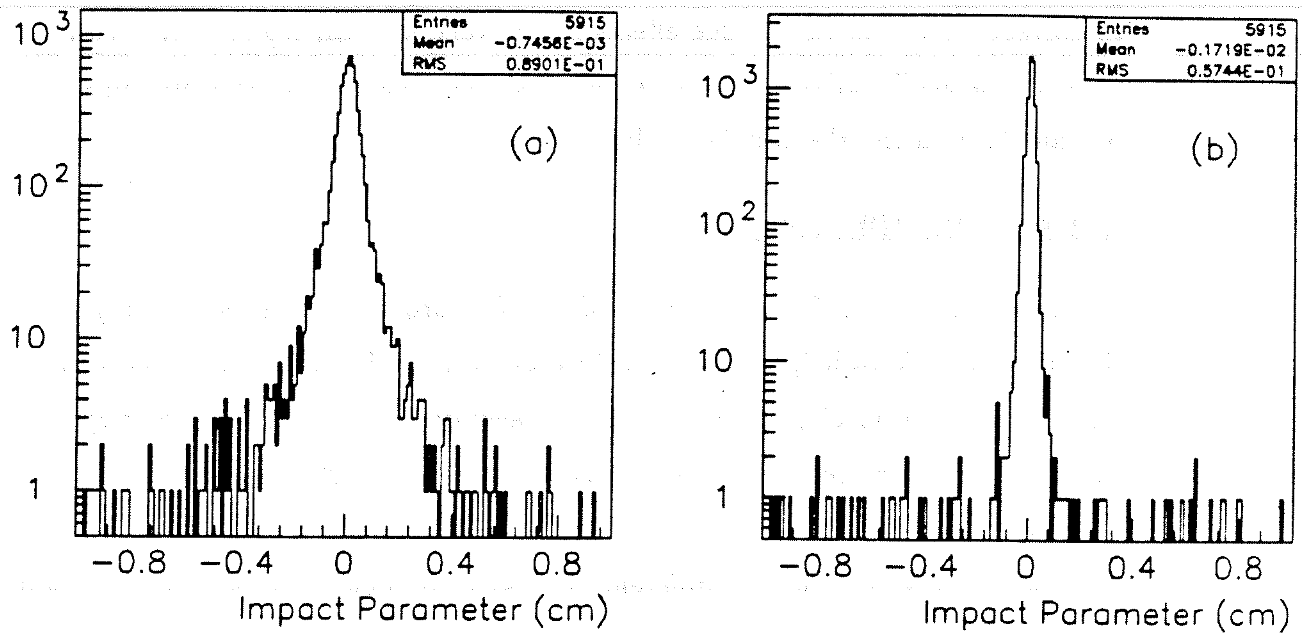

Figure 4.7: Impact parameter (a) before and (b) after a refit to include the VD hits, for tracks with associated VD information from the 1990 data.

where since each tau decays into at least three particles (e.g. $\tau \rightarrow \mu \bar{\nu}_\tau \nu_\mu$), there should always be an acolinearity between the two highest momentum charged tracks.

Fig 4.8 (a) shows the acolinearity of the two highest momentum charged tracks in simulated $\mu^+\mu^-$and $\tau^+\tau^-$events, and events from period II passing cuts C1, C2, C3, C5σ and MU. Fig 4.8 (b) plots the fraction of data lost versus acolinearity cut for both the real data from period II, and a sample containing 10000 each of simulated $\mu^+\mu^-$and $\tau^+\tau^-$events, again passing C1, C2, C3, C5σ and MU. It can be seen that although $\tau^+\tau^-$events tend to have a larger acolinearity than $\mu^+\mu^-$events, an acolinearity cut would have to be at less than 4° to give reasonable $\tau^+\tau^-$rejection, and fig 4.8 (b) shows that at low angles the data and Monte Carlo acolinearity distributions do not agree. This means that there would be a considerable uncertainty in the correction for the number of $\mu^+\mu^-$events lost in making the cut, and so it can not be applied in the selection of events for analysis. However, a 0.5° cut (C4H) is useful when a pure sample of mupairs is needed for studies of other cuts.

Since the cross section analysis uses events from the polar angle region (28°, 152°), and DELPHI's tracking and muon identification detectors extend only to a θ of $\sim 11°$, an acolinearity cut of 10° was decided on, to avoid having to correct for complicated edge effects in the very forward region. At this loose value of the acolinearity cut, a correction for events lost due to the cut can safely be calculated using the simulated data.

4.4.5 C5: Theta cut

In the method used for calculation of the forward-backward asymmetry (log-likelihood fit), knowledge of the absolute detection efficiencies is not necessary, and so in selection of $\mu^+\mu^-$events for the asymmetry calculation, the negative muon track is required to be within the theta region $(22°, 158°)$ defined by the TPC acceptance.

For the cross section and differential cross section calculation it is important to know the absolute detection efficiencies for $\mu^+\mu^-$events. For the first half of the 1990 data there were too few good independent triggers in the forward region to allow a trigger efficiency to be calculated. After run 12868 (June, 1990) the TPC triggers and muon subtrigger were both present, allowing the trigger efficiency and track reconstruction efficiency to be calculated[9]. However, a systematic shift in the momentum measurement in the region between 43° and 33°, where only the TPC and ID are present, makes widening the θ region for the second half of the 1990 data difficult, and it was eventually decided that the reduction in statistical error would be outweighed by the additional systematic error due to the θ dependent correction for the momentum cut. Thus in 1990, the negative muon track was required to be within 43° and 137°, the region defined by the acceptance of the OD.

In 1991, the shift in momentum between 43° and 33° was no longer present, and very efficient single track triggers were present down to around 20°. To make sure that the momentum resolution was good, and to avoid edge effects, it was decided to require the negative muon track to be within the region $(28°, 152°)$, a safe distance from the edge of the TPC acceptance, and just within the VD acceptance.

---

[9] For determination of the track reconstruction efficiency it is necessary to have very efficient single track triggers

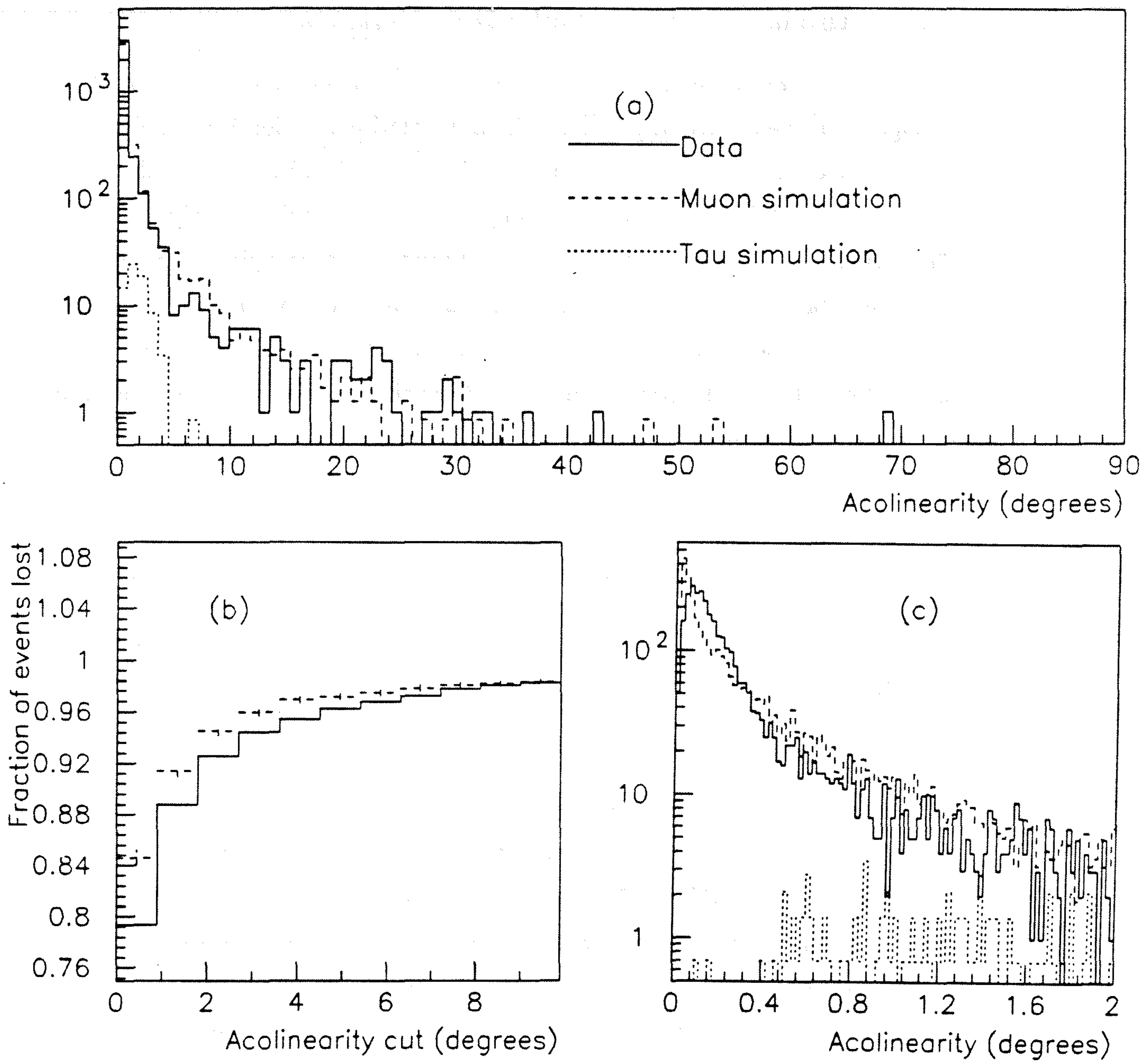

Figure 4.8: (a) Acolinearity of the first two charged tracks for real data, simulated $\mu^+\mu^-$and simulated $\tau^+\tau^-$events passing all standard cuts but the acolinearity cut, (b) Fraction of events passing a certain acolinearity cut versus acolinearity cut for data (points with errors) and Monte Carlo (solid line) events, (c) A more detailed look at (a) at low acolinearity angles.

4.5 Muon Identification

4.5.1 Initial Choice of Selection Criteria

As has already been mentioned, a high energy muon is expected to pass straight through both the electromagnetic and hadron calorimeters, leaving small energy deposits in each, and to produce hits in the muon chambers. To look at the response of DELPHI to muons, a sample of data containing only $\mu^+\mu^-$and e^+e^-events, with very little $\tau^+\tau^-$background (and so very few pions) was selected from the data by applying hard momentum and acolinearity cuts, and requiring exactly two charged tracks (cuts C1H, C2H, C3, C4H and C5A_{FB}). An initial choice of cuts that will separate the muons from the electrons is made by looking at the response of the muon identification detectors to this sample. The plots in this section use all the 1991 data.

The energy E_h associated with a track in HCAL is not used directly, as it is θ dependent. This θ dependence was parametrised to obtain a corrected energy E'_h, given by:

- $E'_h = E_h \sin^2\theta$ $(50° < \theta < 130°)$
- $E'_h = E_h$ $(\theta < 50°, \theta > 130°)$

Figure 4.9 shows E_h and E'_h versus theta, for muons identified using C1H, C2H, C3, C4H, C5σ and MU. It can be seen that the theta dependence of the energy in the barrel (about $45° - 135°$) has been removed by the above correction.

Figure 4.10 (a) shows the energy in the hadron calorimeter versus the energy in the electromagnetic calorimeter for charged tracks in the sample, and fig 4.10 (b) shows the number of hits in the muon chambers versus the energy in the electromagnetic calorimeter for the same tracks. Both these plots are for tracks in the barrel region, so they show the response of the HPC, barrel HCAL and MUB. Similar results are obtained for the FEMC, forward HCAL and MUF, when tracks in the forward region are studied, and also for the 1990 data. There is a clear separation between the muons, which leave on average $5GeV$ in the HCAL, less than $1GeV$ in the HPC and one or more hits in the muon chambers, and the electrons, which deposit no energy in the HCAL or hits in the muon chambers, but leave around $45GeV$ in the HPC.

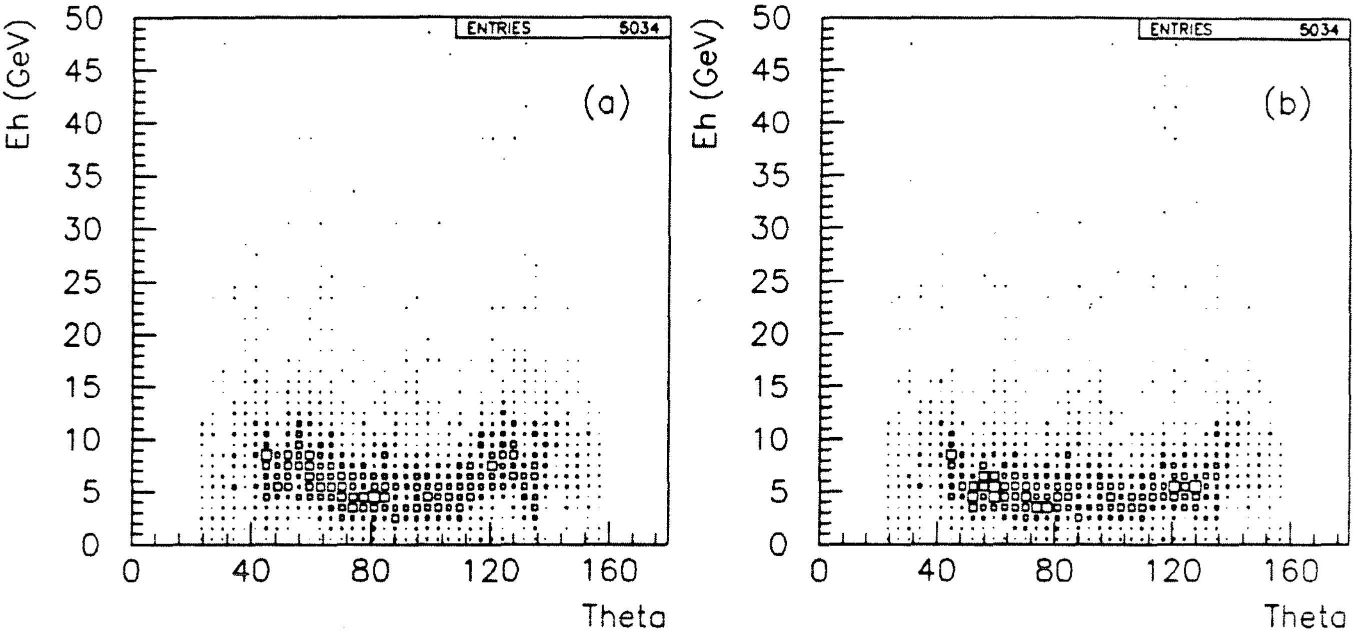

Figure 4.9: (a) E_h versus θ, and (b) E'_h versus θ, both for muons from $\mu^+\mu^-$events in 1991.

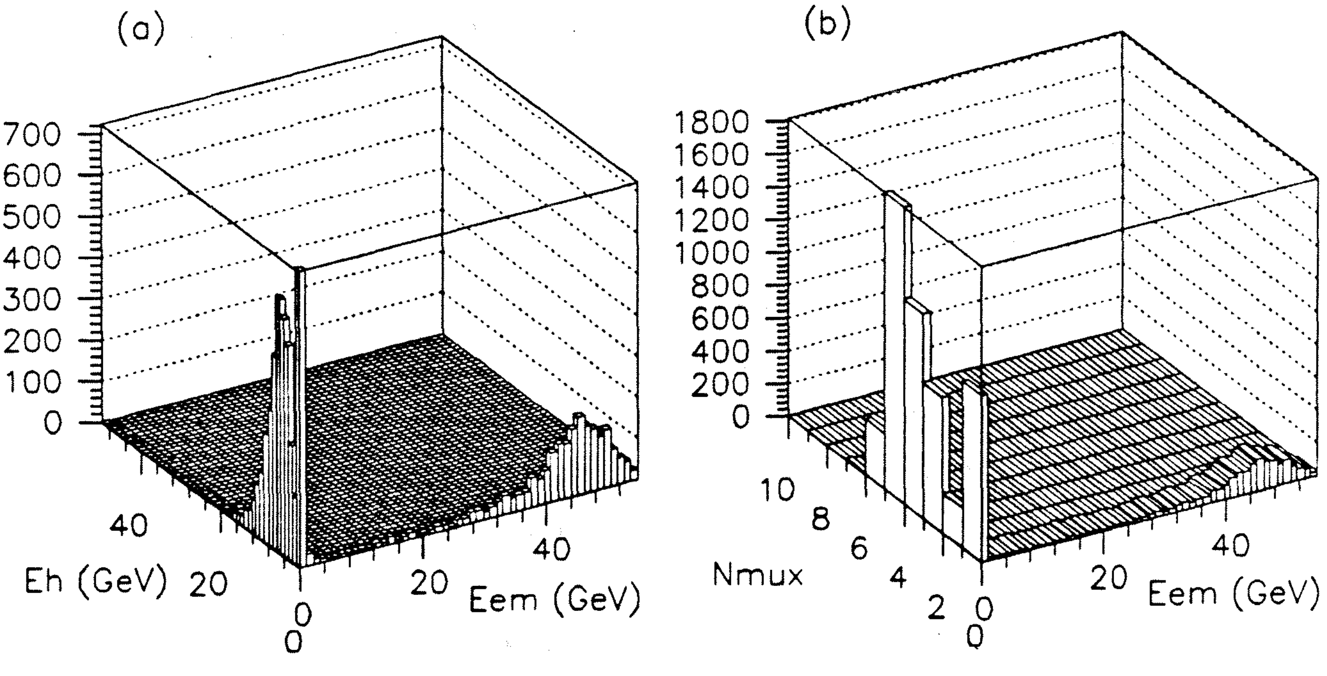

Figure 4.10: (a) E'_h versus E_{em}, and (b) N_{mux} versus E_{em}, both for a roughly equal mixture of electrons and muons from e$^+$e$^-$and $\mu^+\mu^-$events in 1991.

From these plots and fig 4.11, a preliminary set of cuts may be chosen, for use in studying the characteristics of muons in more detail. A particle is classified as a muon if it satisfies any one of the following requirements:

- The energy E_{em} associated with the particle in the HPC or FEMC is between 0 and 1 Gev.
- The energy E_h' associated with the particle in the HCAL is between 0 and 15 Gev for the barrel region $50° < \theta < 130°$, and between 0 and 20 GeV in the forward region.
- The number of associated hits in the muon chambers, N_{mux} is at least 1.

Figures 4.11 shows the response of each of the three muon identification detectors (the HPC and FEMC, barrel and forward HCAL and MUB and MUF are all shown separately) to particles which have been identified as muons by an 'OR' of the other two detectors. The histograms are only filled for particles within the angular range of the detector concerned, and 'Underflow' entries in the histograms for a detector are due to particles for which there was no response in that detector. The conditions chosen above all seem reasonable, and for the muon chambers, HCAL and FEMC give a reasonably high efficiency for muon identification. The HPC efficiency is rather low[10] for the 1991 data, but was high in 1990.

An 'OR' of the above identification criteria in conjunction with the track cuts C1 - C5 chosen in section 4.4 should give a sample of $\mu^+\mu^-$events with high efficiency, and with small e$^+$e$^-$background. The next subsection looks in more detail at the HCAL data, and attempts to improve the HCAL identification criteria to give better discrimination between pions and muons, and so reduce the $\tau^+\tau^-$background.

---

[10] After run 22094 in 1991, the HPC drift voltage was lowered by $100V$ to reduce ageing of the calorimeter modules, and its efficiency for minimum ionising particles (MIPs) dropped significantly, from about 85% to 25%

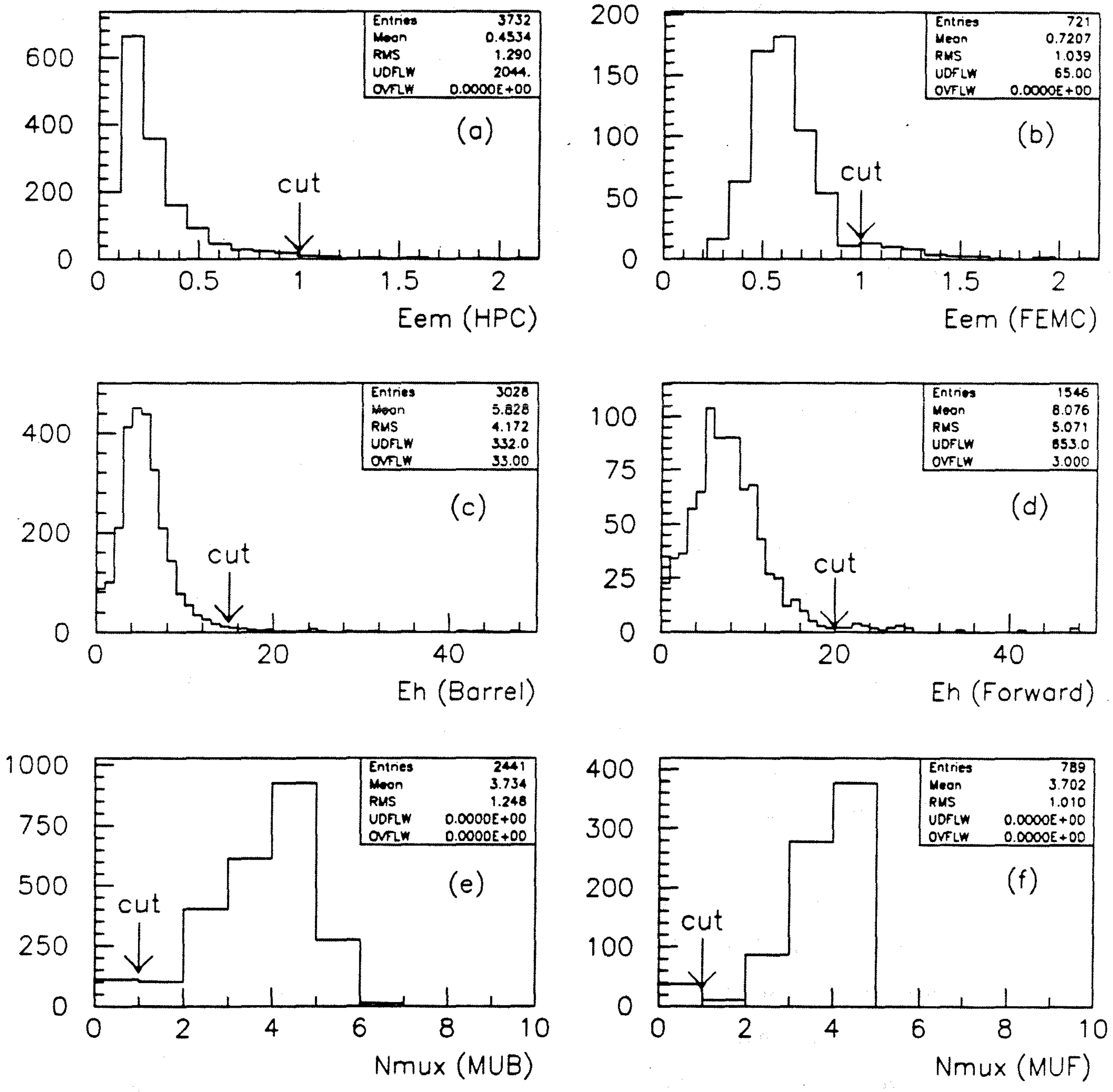

Figure 4.11: (a) and (b) - E_{em} in HPC and FEMC for particles identified as muons in HCAL, MUB or MUF. (c) and (d) - E_h' in the barrel and forward HCAL, for particles identified as muons in HPC, FEMC, MUB or MUF. (e) and (f) - N_{mux} in MUB and MUF for particles identified as muons in HPC, FEMC or HCAL, all for 1991.

4.5.2 A More Detailed Look at the HCAL Data

One of the backgrounds to $\mu^+\mu^-$events is $\tau^+\tau^-$events where the τ leptons have decayed to muons, or one or more pions, and so the HCAL identification criteria should be chosen so that as few pions as possible are identified as muons, without sacrificing too much of the efficiency for muon identification.

In order to look at the response of HCAL to muons, a sample of $\mu^+\mu^-$events is used, selected from the $e^+e^- + \mu^+\mu^-$sample with the additional requirement that the two tracks are identified as muons in either the HPC or MUB, and at least one of the tracks is in the barrel region $43° < \theta < 137°$. The pions studied are taken from a sample of τ 1 prong versus 3 prong events[11] selected by the DELPHI $\tau^+\tau^-$analysis team from the 1991 data. Again, only charged tracks in the barrel region are considered. The particle from the 1 prong decay is taken to be the particle with the largest isolation angle in the event, and approximately 58% of these will be pions, 21% muons and 21% electrons[39]. The other three charged particles are almost all pions.

To study the response of HCAL to pions, the 1 prong side of the tau 1 vs 3 events is used. This is because the granularity of HCAL is not sufficiently good to resolve the three pions on the 3 prong side properly, so that frequently all of the HCAL energy is associated with just one of the tracks, and the HCAL efficiency appears to be much lower than it would be for an isolated pion. The 1 prong decays are also more important because the majority (74%) of $\tau^+\tau^-$events are 1 vs 1 prong events.

An improvement in the HCAL identification criteria will decrease the $\tau^+\tau^-$background if it results in those tracks (presumably pions or electrons) which fail both the HPC and MUB identification criteria, also failing the HCAL cuts. Thus the response of tracks which are associated with an energy deposit in the HPC of greater than $1GeV$, and no associated MUB hits, will be studied. Most electrons are also rejected (on the assumption that they will fail all the muon identification cuts in any case) by requiring $0 < E_{em}/p < 0.6$. Figure 4.12 shows the distribution of E_{em}/p for (a) the $\mu^+\mu^- + e^+e^-$event sample, and (b) the 1 prong tracks in tau 1 vs 3 events, with momentum greater than $15GeV/c$.

---

[11] A τ 1 vs 3 event is a $\tau^+\tau^-$event in which one τ decays to one charged particle plus one or more neutrals, and the other decays to three charged particles plus one or more neutrals.

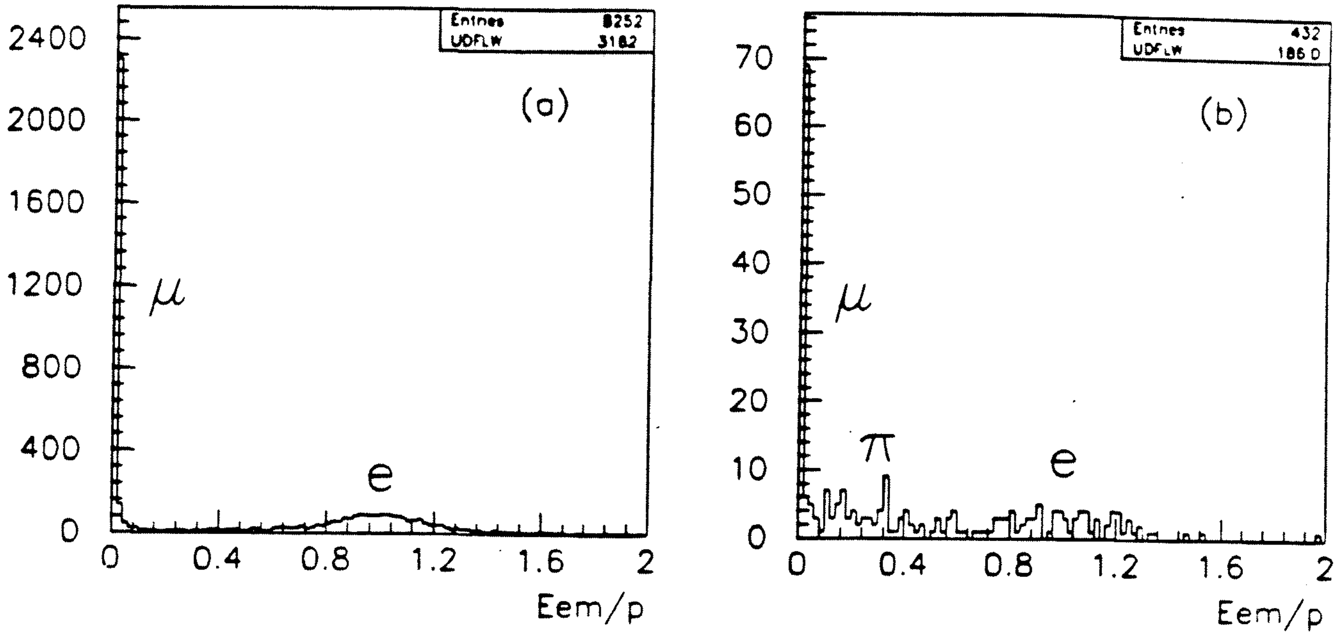

Figure 4.12: E_{em}/p for (a) a roughly equal mixture of muons and electrons, from the 1991 Monte Carlo, and (b) charged tracks from the 1 prong side of a tau 1 versus 3 decay with momentum greater than $15GeV/c$, from the 1991 data.

The above cuts give a sample containing mainly pions, which have failed both the HPC and MUB identification criteria, and, due to the requirement $E_{em} > 1GeV$, have probably started to shower in the HPC. Now the HCAL response to these particles may be studied.

A quantity which has not yet been considered, and which in fact proves to be very useful in discriminating between muons and pions, is the pattern of layers in which energy has been deposited in HCAL. This is provided as a four bit word, bits 0-3 being set when layers 1-4 respectively are hit. The hit pattern word has been plotted for pions and muons in fig 4.13. Most muons deposit energy in three or all four layers, whereas pions tend to deposit energy in between one and four consecutive layers, starting with the first layer, with most pions stopping in the first two layers (hit patterns 1 and 3). After consideration of these plots, the condition for positive muon identification in HCAL is improved to:

- $E_h' < 15GeV$ AND hit pattern ≥ 4.

Fig 4.14 shows E_h' versus the hit pattern for muons, and pions failing the HPC and MUB identification criteria. It can be seen that the new HCAL muon

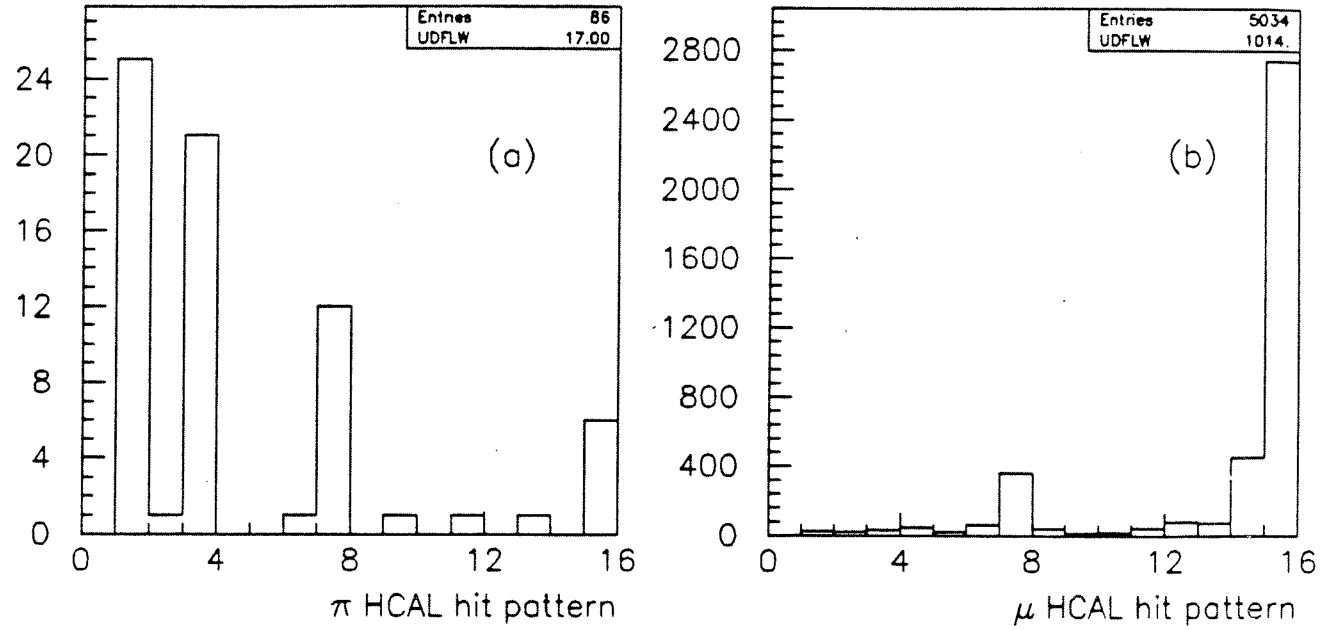

Figure 4.13: (a) HCAL hit pattern for pions of momentum greater than $15GeV/c$, with $E_{em} < 1GeV$ and $N_{mux} = 0$, and (b) HCAL hit pattern for muons, both for 1991 data

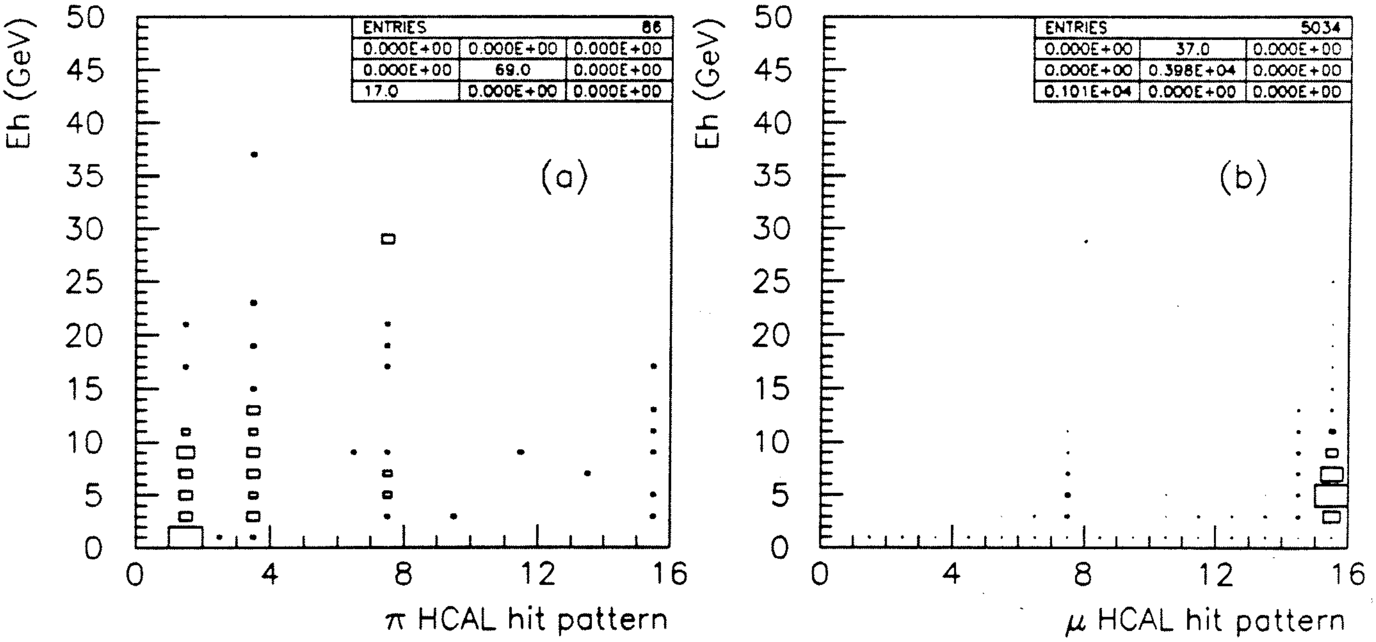

Figure 4.14: E_h' versus HCAL hit pattern for (a) pions of momentum greater than $15GeV/c$, with $E_{em} > 1GeV$ and $N_{mux} = 0$, and (b) muons from $\mu^+\mu^-$events, both for 1991 data

identification condition will be efficient for muons while rejecting most of these pions. The efficiency for these 1 prong pions to be identified as muons in HCAL is estimated from the data to be $(17 \pm 4)\%$, compared with $(66 \pm 5)\%$ using the energy condition alone. The 3 prong pions were also studied, and the efficiency for identification of the 3 prong side of a tau 1 vs 3 event as a muon in HCAL was found to be $(6 \pm 1)\%$.

4.5.3 Muon Identification in the Monte Carlo data

It is very important that the response of the calorimeters and muon chambers in DELSIM accurately reproduces that in the data, because simulated data is needed to estimate the $\tau^+\tau^-$and e^+e^-backgrounds. In particular, the amount of $\tau^+\tau^-$ background due to the 1 vs 1 prong channels π vs π and π vs μ, and the 1 vs 3 prong channels π vs 3π, and μ vs 3π is quite sensitive to small changes in the muon identification criteria.

Figure 4.15 compares the response of forward and barrel HCAL, HPC, FEMC, MUB and MUF to muons in the data and monte carlo, in 1991 [12]. The $\mu^+\mu^-$events were selected using C1H, C2H, C3, C4H, C5σ, and muon identification as summarised in section 4.5.5.

The reproduction of DELPHI's response to muons by the simulation has been seen to be good enough for our purposes, but the pion simulation still needs to be checked. To do this, the 1 prong side of tau 1 vs 3 events from 1991 will again be used, with data taken before and after the HPC voltage drop being considered separately. The muons, electrons and pions are all considered together, as attempting to separate them would rely heavily on the calorimeter and muon chamber simulation, and this is what is under investigation. The overall probability that a 1 prong τ decay will pass the standard track and muon identification cuts C1 - C5σ and MU1-MU3 is given in table 4.4. Since the data and Monte Carlo probabilities agree well both before and after the HPC voltage drop, it is concluded that a Monte Carlo estimate of the $\tau^+\tau^-$background will be reliable.

---

[12] Tuning factors applied to the Monte Carlo data are given in Appendix C

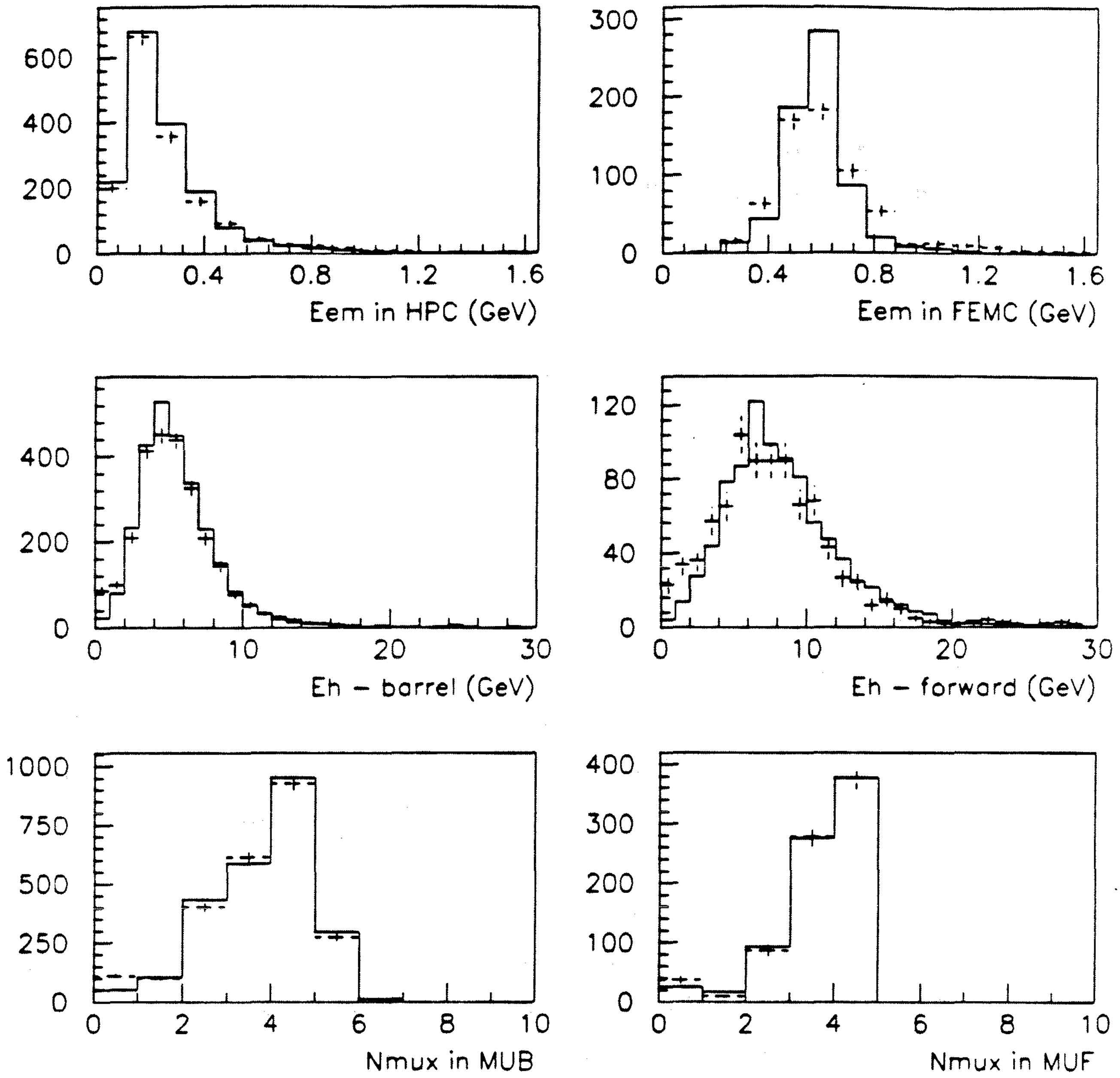

Figure 4.15: Comparison of calorimeter and muon chamber response to muons in the 1991, real (error bars) and simulated (solid line) data.

	Before	After
Data	$(16 \pm 3)\%$	$(13 \pm 1)\%$
Monte Carlo	$(16 \pm 1)\%$	$(13 \pm 1)\%$

Table 4.4: Probability that the 1 prong track in a τ 1 versus 3 decay will be identified as a muon from a $\mu^+\mu^-$ event, before and after the HPC voltage drop, in the data, and in the corresponding simulated data.

4.5.4 Using the Calorimeters to Veto Events

Using an OR of the identification conditions in three muon identification detectors is a very efficient way of identifying muons, but could result in other particles being falsely identified as muons, for example electrons which somehow manage to sneak through to the muon chambers or HCAL. Pions may also pass muon identification cuts, as has already been seen. The calorimeters could be used to veto such events, when large energy deposits, uncharacteristic of a muon, are left in a calorimeter.

Firstly, the HPC and FEMC could be used to veto e^+e^-events. Fig 4.16 shows E_{em2} associated with the second charged track versus E_{em1} associated with the first charged track for tracks in (a) all events passing C1-C5A_{FB} in both 1990 and 1991, and (b), events from the same sample which have been identified as mupairs using the identification criteria chosen above. The tails along each axis are assumed to be mainly due to radiative $\mu^+\mu^-$events, where one of the muons radiates a photon and the electromagnetic energy deposit produced by the photon is associated with the muon. The fact that the tail is longer for the lower momentum charged track, which is more likely to have radiated a high momentum γ, supports this assumption. There are no obvious e^+e^-candidates present, and so an E_{em} veto will not be applied.[13]

Another possibility is the use of HCAL to veto some of the $\tau^+\tau^-$background, when the tau decay products are pions. The tau background before any vetos is estimated from the simulated data to be $(2.0 \pm 0.2)\%$ before run 22094, and $(1.4 \pm 0.1)\%$ after run 22094[14].

Figure 4.17 (b) shows the corrected energy in HCAL associated with each of the μ tracks in 'gold plated' $\mu^+\mu^-$events, selected from the 1990 data using C1H, C2H, C3, C4H, C5A_{FB} and MU, and fig 4.17 (a) shows the simulated distribution of HCAL energy for tracks in $\tau^+\tau^-$events passing the standard $\mu^+\mu^-$cuts. It can be seen from fig 4.17 (b) that the veto must be set as low as possible in order to reject a reasonable amount of the background. The most harsh veto that can

---

[13] DELPHI is designed so that the HCAL and HPC/FEMC cracks do not coincide - thus electrons failing to produce a response in the electromagnetic calorimeters invariably lose all their energy in HCAL, and they never pass the HCAL cuts because in fact all their energy is lost within the first two layers.

[14] The difference in these figures is due to the lowering of the HPC efficiency at run 22094

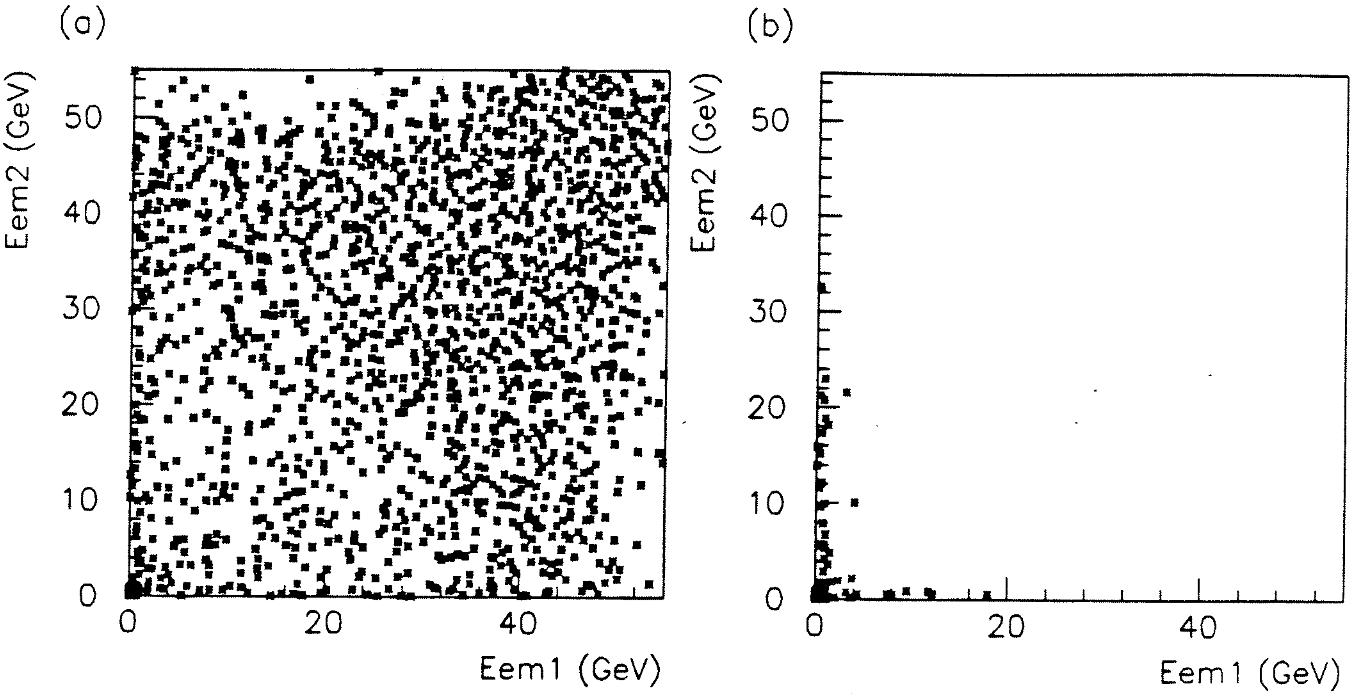

Figure 4.16: (a) E_{em2} versus E_{em1} for events passing the standard track cuts in all the data, and (b) E_{em2} versus E_{em1} for the same sample, for charged tracks identified as muons.

be applied is to reject events in which one or more of the μ candidates have E_h' greater than the cut used for positive identification in the HCAL. However, a study of the 'gold plated' $\mu^+\mu^-$candidates shows that this would veto $(3.9\pm0.4)\%$ of genuine $\mu^+\mu^-$events in 1990, which is far too many.

It has been suggested [40] that the veto could be applied to only those $\mu^+\mu^-$candidates with greater than 1° acolinearity, as in the simulated data, these events contain $(84 \pm 4)\%$ of $\tau^+\tau^-$events that pass the $\mu^+\mu^-$cuts, and only $(17.7 \pm 0.4)\%$ of the genuine $\mu^+\mu^-$events. Table 4.5 summarises the effect of this veto on the number of $\mu^+\mu^-$events, and on the $\tau^+\tau^-$background, where the $\tau^+\tau^-$background has been calculated using the simulated data, and the loss of $\mu^+\mu^-$events is calculated using the results given above for 'gold plated' muons from the data, and assuming that $(17.7 \pm 0.4)\%$ of $\mu^+\mu^-$events have acolinearity greater than 1°.

This veto is worth applying only if it reduces the total error on the cross section and asymmetry measurements. Table 4.5 shows that the combination of the statistical errors on the $\tau^+\tau^-$background and $\mu^+\mu^-$loss corrections is not significantly improved by the veto, and additional systematic errors (e.g. due to the imperfect representation of the acolinearity distribution at low angles in

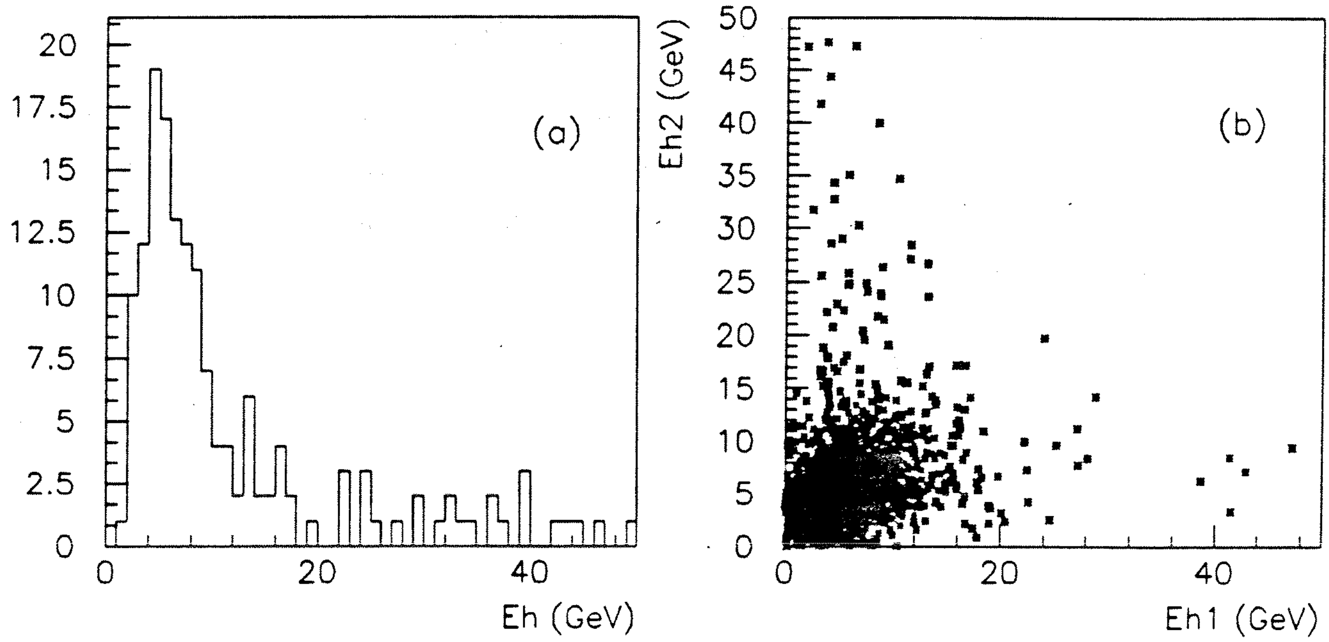

Figure 4.17: (a) Simulated E'_h distribution for tracks in $\tau^+\tau^-$events which pass $\mu^+\mu^-$cuts, (b) E'_{h1} versus E'_{h2} for 'gold plated' $\mu^+\mu^-$events selected from 1990 data using C1H, C2H, C3, C4H, C5A_{FB} and MU.

	No Veto	Veto
$\mu^+\mu^-$loss (%)	0	0.69 ± 0.07
$\tau^+\tau^-$background (%)	2.00 ± 0.15	1.61 ± 0.13
Error	0.15	0.15

Table 4.5: Loss of $\mu^+\mu^-$events, $\tau^+\tau^-$background, and the total error due to both corrections, before and after an HCAL veto in the 1990 data

the simulated data) will also be introduced by the use of the veto. Therefore no HCAL veto will be applied.

4.5.5 Summary of Muon Identification Criteria

An event is classified as a mupair candidate if it satisfies the track cuts of section 4.4, and each of the muon candidates (the two charged tracks of highest momentum in the event) are positively identified as muons, by satisfying at least one of the following criteria:

MU1: $0 < E_{em} < 1 GeV$

MU2: $N_{mux} \geq 1$

MU3: The HCAL identification criteria are summarised in the following table, where E'_h is given by:

- $E'_h = E_h \sin^2\theta$ ($50° < \theta < 130°$)
- $E'_h = E_h$ ($\theta < 50°, \theta > 130°$)

Year	$50° < \theta < 130°$	$\theta < 50°, \theta > 130°$	Hit pattern cut
1990	$0 < E'_h < 10 GeV$	$0 < E'_h < 15 GeV$	Hit pattern ≥ 4
1991	$0 < E'_h < 15 GeV$	$0 < E'_h < 20 GeV$	Hit pattern ≥ 4

Table 4.6: HCAL muon identification criteria for each θ region, for 1990 and 1991

where E_{em} is the energy associated with the track in the HPC or FEMC, E'_h is the corrected energy associated with the track in HCAL, and N_{mux} is the number of muon chamber hits associated with the track.

4.6 Charge Determination

Where both tracks in a $\mu^+\mu^-$candidate event have the same charge, the ambiguity is resolved by assuming that the charge of the track with the smaller absolute

Year	Total $\mu^+\mu^-$events for A_{FB}	Like sign events	++ events	−− events	Percentage bad charge
1990	3995	57	33	24	1.4%
1991	3529	9	5	4	0.3%

Table 4.7: Charge misassignment in 1990 and 1991.

momentum error is correct, and forcing the charge of the other track to be opposite. This was shown to be a reliable method of resolving charge ambiguities by looking at the difference between the ϕ positions of barrel muon chamber hits associated with the two highest momentum charged tracks in $\mu^+\mu^-$candidate events[42], since because of the large radius of the barrel muon chambers, this ϕ difference gives an unambiguous determination of the charges of the muons. It was shown that the efficiency of this method in determining the charge correctly was $\sim 90\%$.

The numbers of like sign events, and the number of events with two positive muon candidates and two negative muon candidates, are summarised in table 4.7. The angular distribution of the like sign events was studied, and the correlation between them was found to be small, though there was a slight tendency for like sign events to be in the forward region. The percentage of events in which both tracks have the wrong charge assigned to them was thus determined to be negligible. As mentioned above, the charge of the tracks in like sign events is determined by the track with the smallest absolute momentum error, and this method has an efficiency of $\sim 90\%$. An estimate of the percentage of events with the wrong charge assignment is also given in table 4.7, and this contributes to the systematic error in A_{FB}, as will be described in chapter 5.

4.7 Correction Factors - Efficiencies

4.7.1 Track Reconstruction Efficiency

There are three contributions to the track reconstruction inefficiency in DELPHI, the two largest being due to losses at the TPC centre plane at $\theta = 90°$, and its sector boundaries every 60° in ϕ, and the third, smaller, contribution being the track reconstruction efficiency in the fiducial volume of the TPC. These contributions are considered to be independent, and are calculated separately as described below.

TPC sector boundaries

Track losses at the TPC sector boundaries are calculated by selecting $\mu^+\mu^-$events using C1-C5σ and MU, and plotting ϕ mod 60° for the muons in the events. The central bins around (ϕ mod 60°) = 30° have a reduced number of entries due to losses at the sector boundaries, particularly in $35° < \theta < 43°$ and $145° > \theta > 137°$, where only the TPC and ID are present. Figure 4.18 shows (ϕ mod 60°) for tracks in $\mu^+\mu^-$events in three θ regions - the first plot is for the region where the TPC, ID and OD are all present, the second plot is for events in the region where only the TPC and ID are present, and the third is for the region where the TPC, ID and FCA and FCB are all present.

To calculate the correction factor, ϕ mod 60° was plotted in 30 bins, and the total number of entries in the central 6 bins[15] (N_{cent}), and the other 24 bins (N_{edge}) were counted. The inefficiency $1 - \epsilon$ for $\mu^+\mu^-$events caused by the sector boundaries is then given by equation 4.2.

$$1 - \epsilon = \frac{1}{5}\left(1 - \frac{4N_{cent}}{N_{edge}}\right) \tag{4.2}$$

This then gives a correction factor for the TPC ϕ loss of $\frac{1}{\epsilon}$.

The error on this correction is absorbed by scaling up the statistical percentage error on the cross section by $\sqrt{\frac{5}{4}}$, as only events with tracks greater than 6° from a TPC sector boundary are contributing statistically in the calculation of the cross section.

Loss at $\theta \sim 90°$

The correction for the loss of events in the centre plane of the TPC is made in a similar way to the ϕ loss correction. After all the other corrections have been made, the corrected $\cos\theta$ distribution of the negative tracks in the events is plotted, and the central two $\cos\theta$ bins (out of 48) are given values which are

---

[15] corresponding to ±3° either side of the ϕ crack

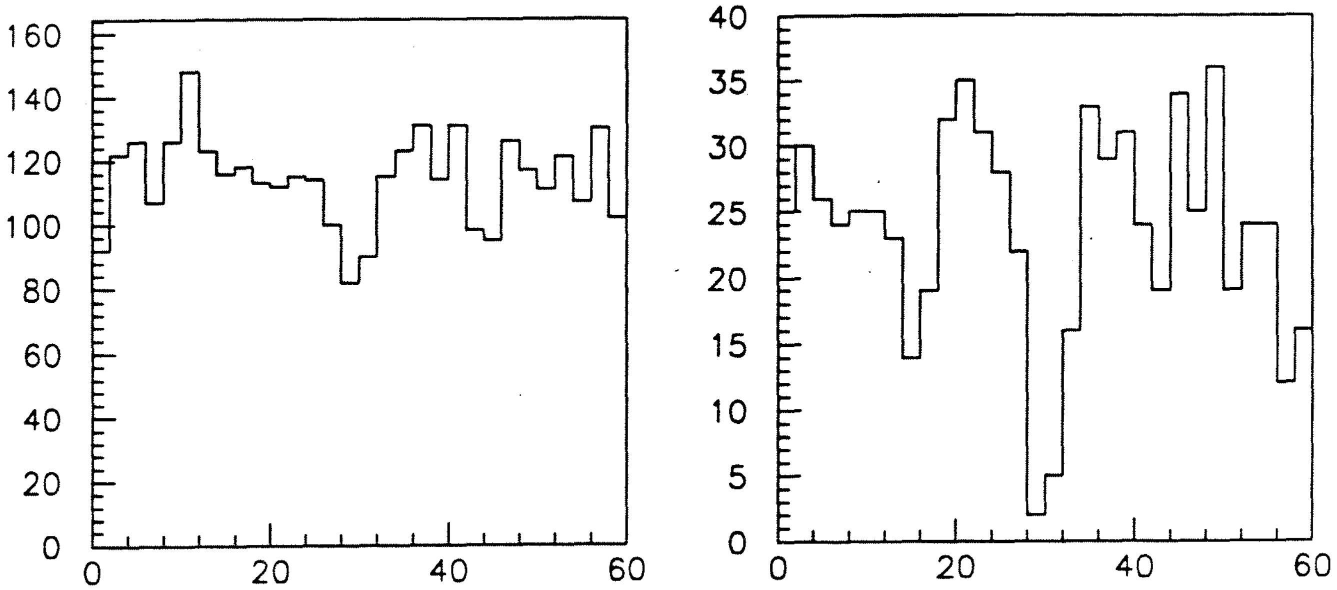

(a) Phi loss – TPC+OD

(b) Phi loss – TPC only

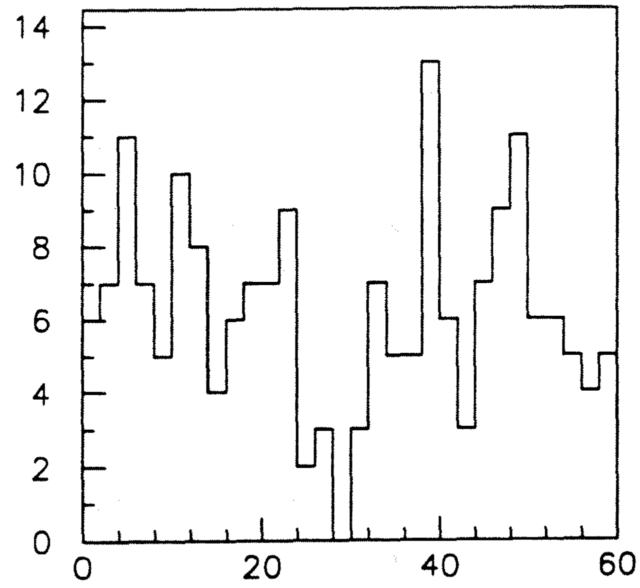

(c) Phi loss – TPC+FCH

Figure 4.18: ϕ mod 60° of charged tracks in $\mu^+\mu^-$events in (a) $43° < \theta < 137°$), (b) $35° < \theta < 43°, 145° > \theta > 137°$, (c) $28° < \theta < 35°, 152° > \theta > 145°$, 1991 data.

obtained by finding a weighted mean of the contents of all the other bins in the barrel region, assuming a $1 + \cos^2\theta + R\cos\theta$ distribution. The central bins are each given the same value, so they have zero asymmetry (though this effect would be negligible in any calculation of the asymmetry by a counting method). The statistical error on the cross section is scaled up as for the ϕ loss correction, as events within $\sim 2.5°$ of the $\theta \sim 90°$ region are not contributing statistically in the calculation of the cross section.

Inefficiency in the fiducial volume of the TPC

The inefficiency in the fiducial volume of the TPC was measured as a function of $\cos\theta$, by selecting events with a high momentum muon candidate, and looking for another track roughly back to back with the first. The selection criteria for the first track were:

- $N_{ch} \leq 5$.
- $40GeV/c < p < 56GeV/c$. The lower limit rejects $\tau^+\tau^-$events, beam-gas events and cosmic ray muons, the upper limit rejects cosmic ray muons.
- $22° < \theta < 87°$ or $92° < \theta < 158°$. The plane at $\theta \sim 90°$ is removed with a slightly asymmetric cut, because the beamspot position is at $\sim -0.5cm$ in the DELPHI frame.
- ϕ is further than 10° from a TPC sector boundary.
- *Rimpac* $< 50\mu m$ (using the vertex detector if possible), and *Zimpac* $<$ $3.0cm$. These cuts are tighter than normal to reject cosmic ray muons.
- Standard muon identification.

and a second track satisfying the following criteria was searched for.

- $p > 5GeV/c$.
- *Rimpac* $< 1.5cm$ (using the vertex detector if possible), and *Zimpac* $<$ $4.5cm$.

- Acolinearity with respect to the first track of less than 20°.

If no such other track is found, then the track reconstruction is assumed to have failed for the second track. For the calculation of the θ dependent track reconstruction efficiency, the θ position of the second track is assumed to be back to back with that of the high momentum muon candidate, whether it is reconstructed or not. The result of this measurement in 1991 is shown in fig 4.19 (a).

This method of measuring the track reconstruction efficiency produces a result which is an underestimate of the true efficiency, due to the effects of the momentum and acolinearity requirement on the second track, and $\tau^+\tau^-$background. This inefficiency due to the method was calculated by applying the same cuts to a sample containing 10000 each of simulated $\mu^+\mu^-$and $\tau^+\tau^-$events, and dividing the result obtained with the true track reconstruction efficiency in the fiducial region of the TPC, taken directly from the Monte Carlo simulation information. The true efficiency in the simulation was very close to 100% over the barrel region, and the resulting efficiency 'of the method' as a function of $\cos\theta$ is shown in fig 4.19 (b). The real track reconstruction efficiency as a function of $\cos\theta$ was then obtained by dividing fig 4.19 (a) by fig 4.19 (b), giving fig 4.19 (c).

As the efficiency in the barrel region is very high, small statistical fluctuations can mean that the corrected efficiency in a few of the $\cos\theta$ bins can be greater than 1. The average track reconstruction efficiency in the barrel region calculated by using the above method, and then finding the weighted mean of the efficiency between 43 and 137 degrees, assuming a $1 + \cos^2\theta$ distribution, was found to be $(1.001 \pm 0.001)\%$, which is clearly consistent with 1. Furthermore, examination of all events (approximately 60 in total) which contained a high momentum muon in the barrel region passing the first set of cuts, but had no track passing the second set of cuts revealed no sign of any genuine loss of tracks. Thus the track reconstruction efficiency may be taken to be 100% over the barrel region.

The track reconstruction efficiency for $\mu^+\mu^-$events is found by multiplying the efficiencies in back-to-back $\cos\theta$ bins, giving a distribution symmetric about $\cos\theta = 0$, as shown in fig 4.20. The total track reconstruction efficiency may

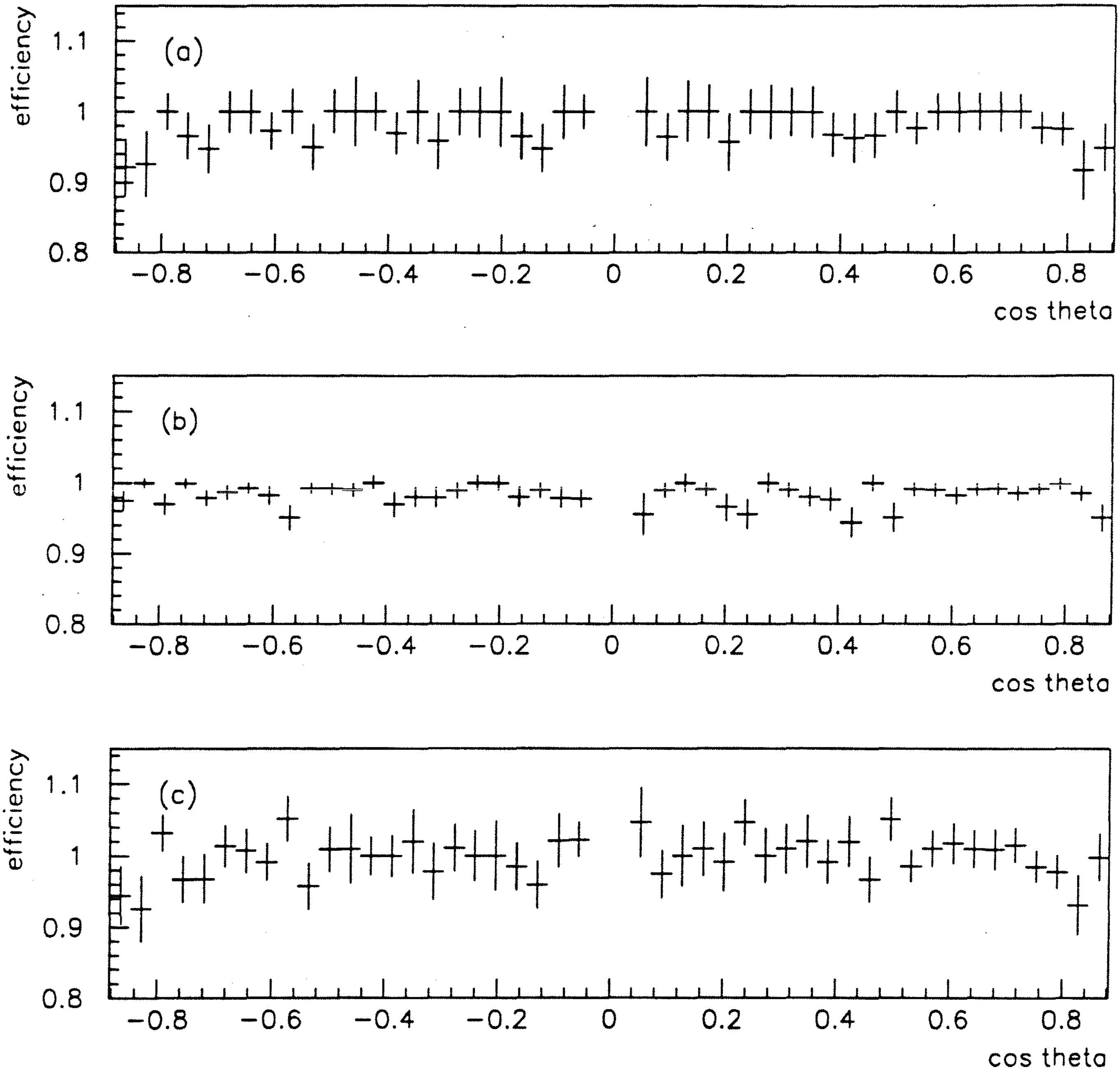

Figure 4.19: (a) Raw track reconstruction efficiency in the fiducial volume of the TPC versus $\cos\theta$ in $\mu^+\mu^-$events, (b) Efficiency of the method of measurement of the efficiency (measured divided by actual efficiency) in the Monte Carlo, and (c) True track reconstruction efficiency, given by dividing (a) by (b).

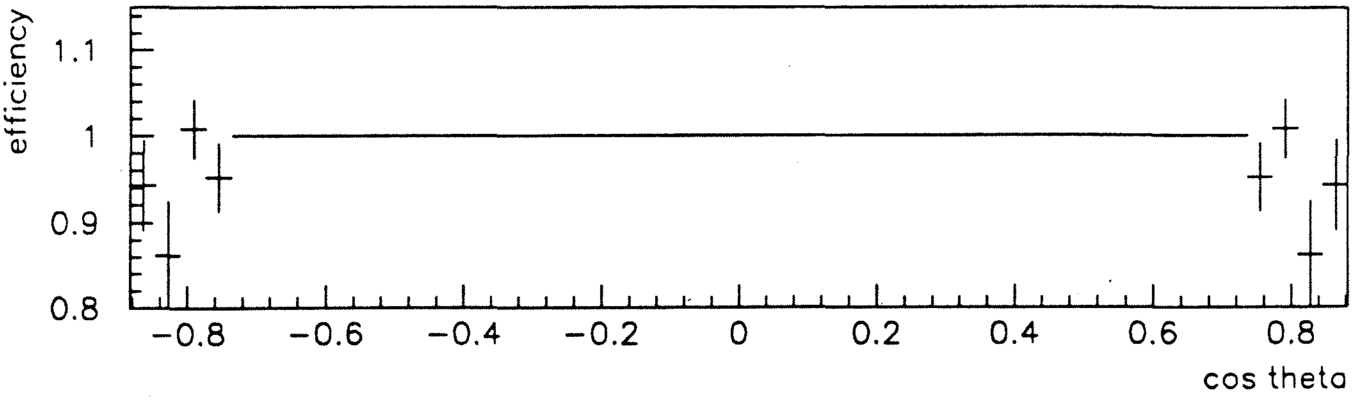

Figure 4.20: Track reconstruction efficiency for a $\mu^+\mu^-$event in the fiducial volume of the TPC in 1991, versus $\cos\theta$. The efficiency in the barrel region has been fixed at 100%.

then be calculated as a weighted mean of the resulting histogram, assuming the $\mu^+\mu^-$events follow a $1+\cos^2\theta$ distribution.

4.7.2 Muon Identification Efficiency

To measure the efficiency of each muon identification detector, events were selected using C1 - C5σ, and positive muon identification in one of the other two muon identification detectors. For example, the HCAL efficiency was measured using a sample of $\mu^+\mu^-$events selected using the electromagnetic calorimetry and muon chambers alone. Figures 4.21 and 4.22 show the single track muon identification efficiency versus $\cos\theta$ in the three muon identification detectors, and the total single arm efficiency, which is an 'OR' of the efficiencies for the three detectors. The identification efficiency for $\mu^+\mu^-$events is found by multiplying the efficiencies in back-to-back $\cos\theta$ bins, giving a distribution symmetric about $\cos\theta = 0$, as shown in fig 4.23.

The overall muon identification efficiency may be calculated as a weighted mean over the required range in $\cos\theta$, assuming that the $\cos\theta$ distribution of the tracks in $\mu^+\mu^-$events follows a $1+\cos^2\theta$ distribution. The resulting efficiencies are as follows:

(a) HPC 1990

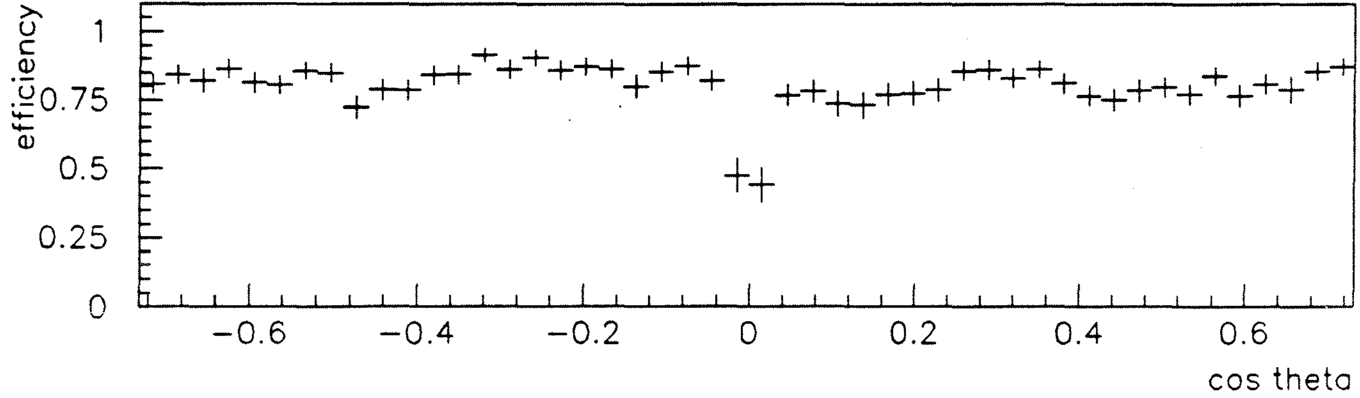

(b) HCAL 1990

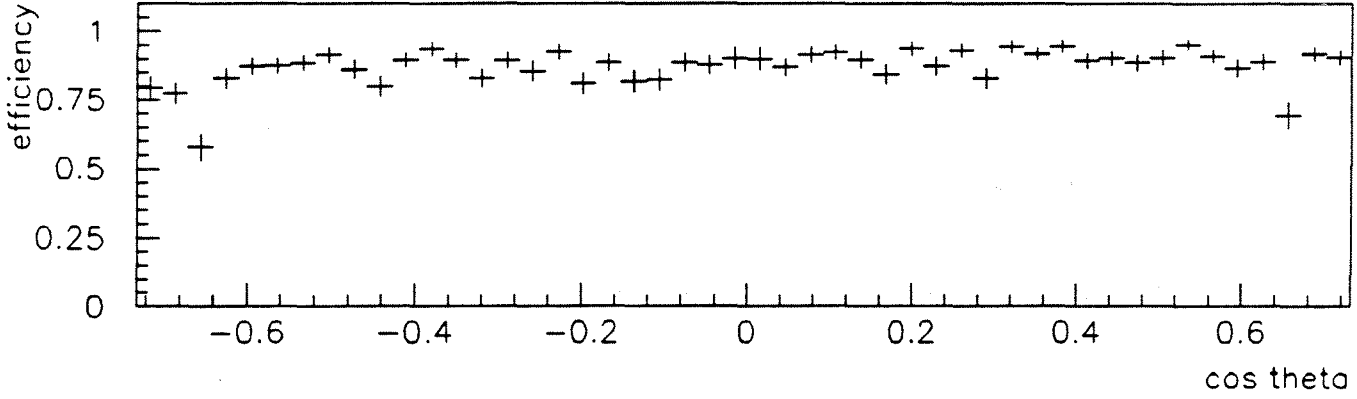

(c) MUB 1990

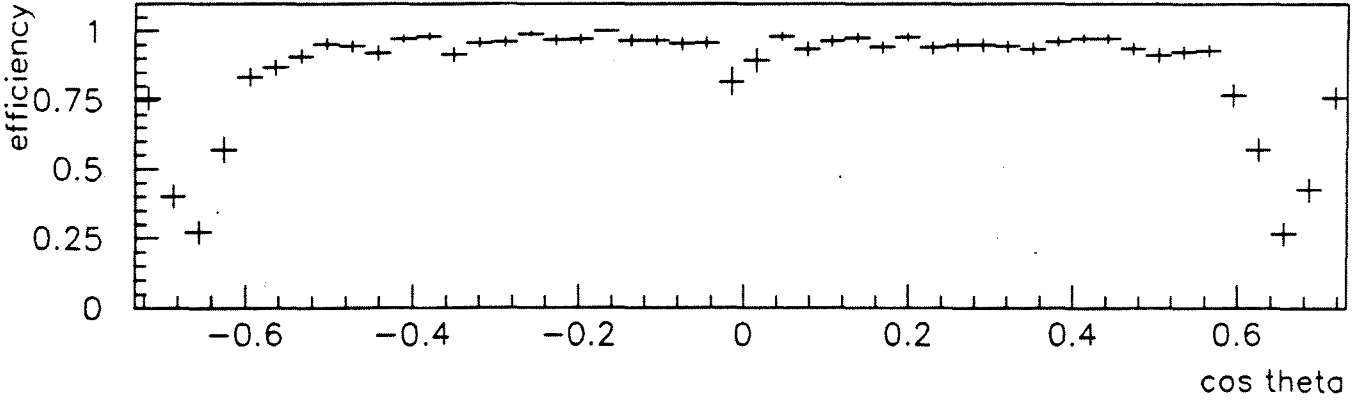

Figure 4.21: Single arm muon identification efficiency versus $\cos\theta$ for (a) HPC and FEMC, (b) HCAL, and (c) MUB and MUF in 1990.

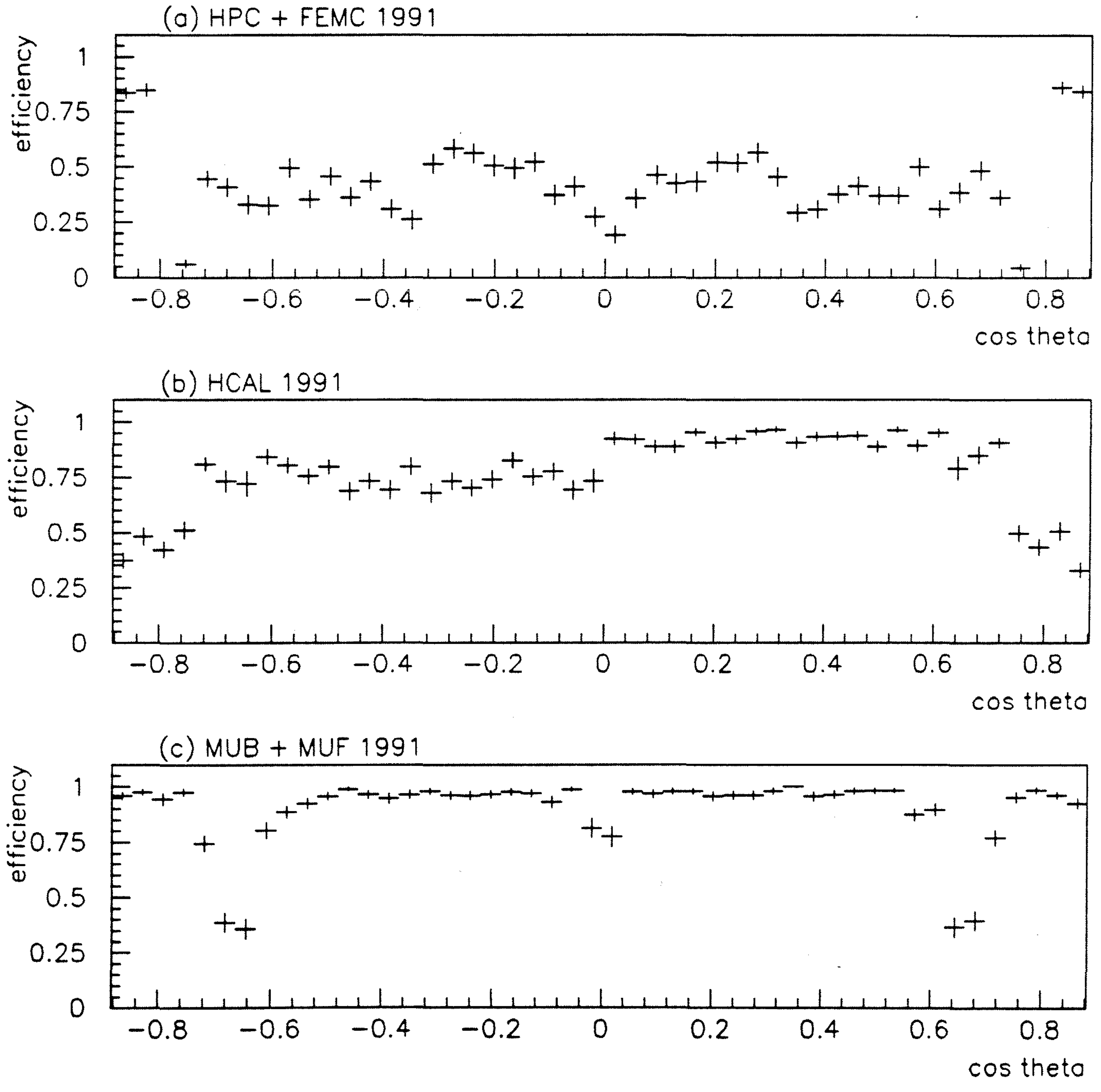

Figure 4.22: Single arm muon identification efficiency versus $\cos\theta$ for (a) HPC and FEMC, (b) HCAL, and (c) MUB and MUF in 1991.

(a) 1990

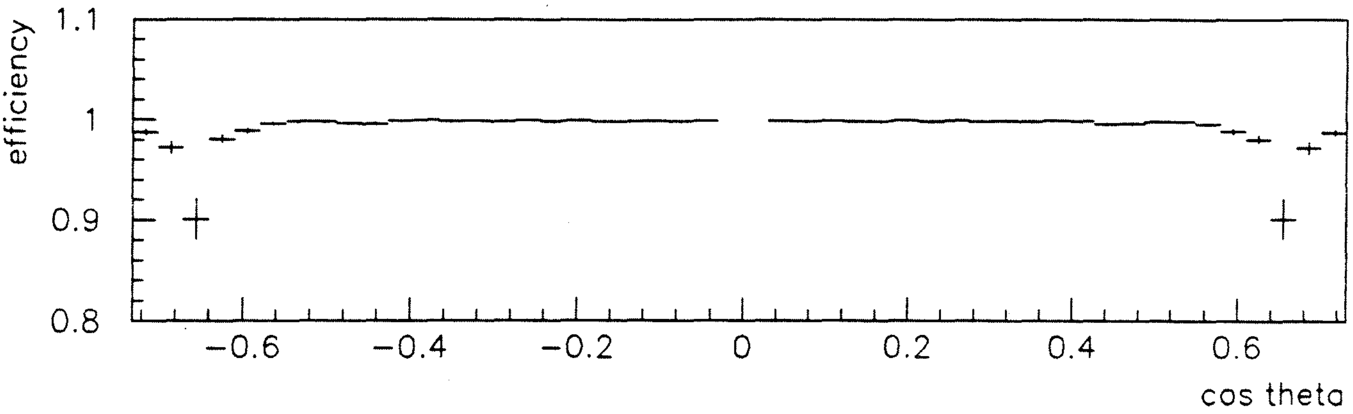

(a) 1991

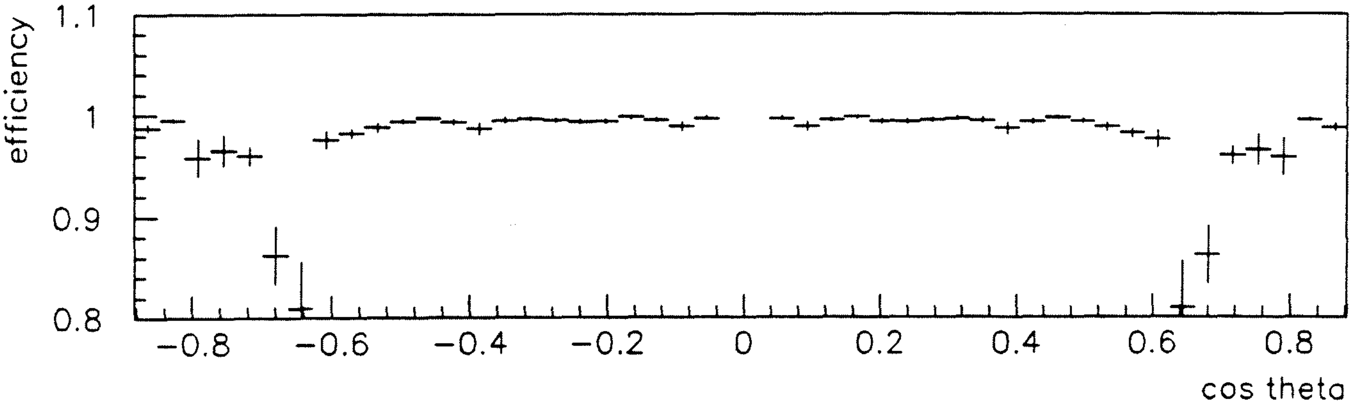

Figure 4.23: Identification efficiency for a $\mu^+\mu^-$event versus $\cos\theta$ in (a) 1990, and (b) 1991.

1990	$(98.96 \pm 0.20)\%$
1991	$(97.53 \pm 0.22)\%$

Table 4.8: Muon identification efficiencies for the $\mu^+\mu^-$analysis.

4.7.3 Trigger Efficiency

The trigger efficiency was calculated for the $\mu^+\mu^-$analysis team by B. Nijjhar and D. Reid in 1990, and by P. Kluit in 1991[31, 32]. This analysis will use the Nijjhar and Reid result for the 1990 data, and the Kluit result for the 1991 data, when the TPC contiguity trigger, forward majority trigger and muon subtrigger were all present.

Trigger efficiencies are calculated by using a sample of $\mu^+\mu^-$events selected from the data, and comparing the response of independent triggers to these events. If there were two independent triggers, the efficiency would be calculated as follows [30].

$$\epsilon_1 = \frac{N_{12}}{N_2} \pm \frac{\epsilon_1(1-\epsilon_1)}{N_2} \tag{4.3}$$

$$\epsilon_2 = \frac{N_{12}}{N_1} \pm \frac{\epsilon_2(1-\epsilon_2)}{N_1} \tag{4.4}$$

$$\epsilon_{tot} = \epsilon_1 + \epsilon_2 - \epsilon_1 \times \epsilon_2 \pm \Delta(\epsilon_{tot}) \tag{4.5}$$

where ϵ_1, ϵ_2 and ϵ_{tot} are the efficiencies of the first and second triggers, and the 'OR' of the two, respectively, and N_{12}, N_1 and N_2 are the numbers of events firing both triggers, the first trigger, and the second trigger respectively, as shown in fig 4.24. $\Delta(\epsilon_{tot})$ is given in [30].

For period I, various combinations of the following B1 triggers were present (* denotes a logical AND).

- TOF back to back trigger (TOBB)
- TOF singles * OD singles (SCOD)
- ID singles * OD back-to-back (IDOD)

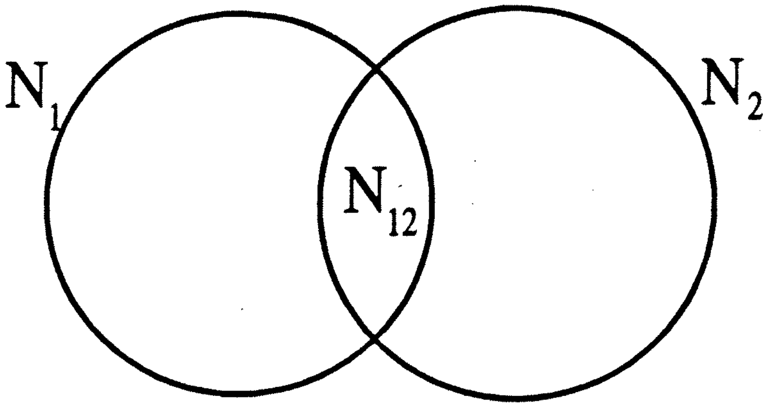

Figure 4.24: Venn diagram for the calculation of the efficiencies of two independent triggers.

- ID singles * OD majority 2 (IOMJ)
- TPC RZ and contiguity triggers

The overall trigger efficiency was calculated using the method above, taking correlations between the triggers into account

For 1991, the triggers were divided into two independent groups, A and B, where A contained the triggers based on the TPC or Forward Chambers, and B contained the triggers not dependent on the TPC or FC. The efficiencies of the two groups were high (above about 95%) over the whole angular region, and this enabled the efficiencies of individual components of the trigger to be measured precisely.

The results are summarised in table 4.9.

Fig 4.25 shows the trigger efficiency versus $\cos\theta$ in detail for 1991.

4.7.4 Losses due to the Momentum and Acolinearity cuts

The loss of $\mu^+\mu^-$events due to the momentum and acolinearity cuts used in this analysis was estimated from a sample of 10000 simulated $\mu^+\mu^-$events. This loss

Period	Efficiency	Error (stat)	Error (syst)
1990, runs 7912-9632	0.921	0.013	0.006
1990, runs 9633-10500	0.992	0.002	0.003
1990, runs 10501-10627	0.986	0.013	0.0
1990, runs 10628-10679	0.992	0.002	0.003
1990, runs 12868-15879	0.9998	0.0002	
1991	0.9987	0.0004	0.001

Table 4.9: Trigger efficiencies for the $\mu^+\mu^-$analysis.

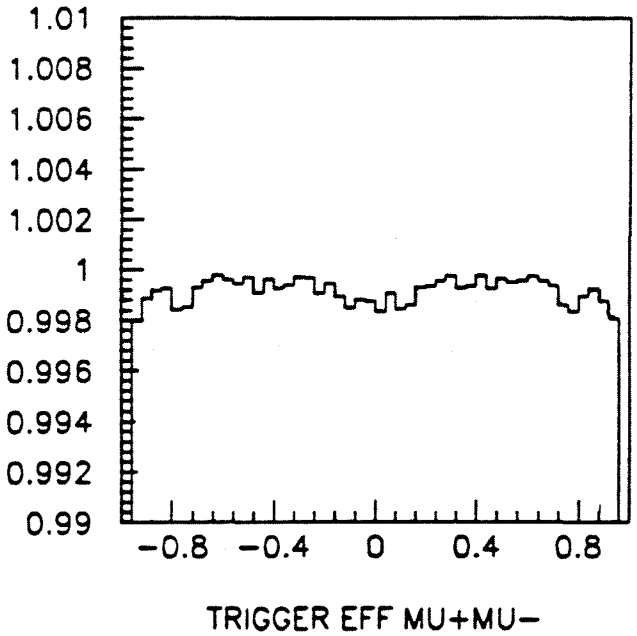

Figure 4.25: Trigger efficiency for $\mu^+\mu^-$events versus $\cos\theta$ in 1991, from [32]

is $\sqrt{s}$ dependent as the momentum cut used is constant, and over the region of the Z^{0}resonance is given by equation 4.6,

$$\epsilon_i = \left(0.066\left(\frac{E_p}{E_i} - 1\right) + 0.0369\right) \pm 0.0014 \tag{4.6}$$

where ϵ_i is the percentage loss of events at energy point i having centre of mass energy E_i, and E_p is the peak energy point. This formula was obtained by applying different momentum cuts to the simulated data, which was all generated at the peak.

4.8 Calculation of Correction Factors - Backgrounds

4.8.1 $\tau^+\tau^-$Background

The $\tau^+\tau^-$background was estimated by applying the $\mu^+\mu^-$selection criteria to 10000 each of simulated $\mu^+\mu^-$and $\tau^+\tau^-$events. If the number of events passing the $\mu^+\mu^-$cuts from the $\mu^+\mu^-$and $\tau^+\tau^-$samples are N_μ and N_τ respectively, then the $\tau^+\tau^-$background is given by

$$\frac{N_\tau}{N_\mu + N_\tau}. \tag{4.7}$$

Two samples of simulated data were used, corresponding to the periods before and after the HPC voltage drop. The tau backgrounds for 1990 and 1991 are given in table 4.10, where the errors are statistical. The lower tau background in 1991 is due to the loss of efficiency in the HPC - since the overall efficiency for misidentification of a pion as a muon is the 'OR' of three fairly low efficiencies, the loss in HPC efficiency affects this overall efficiency much more than it does the muon identification efficiency, resulting in a drop in the $\tau^+\tau^-$background.

1990	$(2.0 \pm 0.2)\%$
1991	$(1.4 \pm 0.1)\%$

Table 4.10: Values for the $\tau^+\tau^-$background estimated from simulation

4.8.2 Cosmic Background

The cosmic ray muon background was estimated by varying the impact parameter cut and seeing how the number of $\mu^+\mu^-$candidates altered. There were two types of $\mu^+\mu^-$candidate, those with VD information associated with one or more of the muon tracks, and those without any VD information (the latter type formed 2% of the $\mu^+\mu^-$candidates in 1990 and 0.5% in 1991).

Tables 4.11 and 4.12 give the results of varying the impact parameter cut on the number of $\mu^+\mu^-$candidates selected. The increase in the number of $\mu^+\mu^-$candidates appears to depend linearly on the impact parameter cut, and this fact was used to estimate the number of events within both the 1.5cm impact parameter cut used for tracks with no VD information, and the 0.4cm impact parameter cut used when VD information is present. The events with VD information present were studied separately, to confirm that their cosmic background also depends linearly on the impact parameter cut (using the impact parameters given by the VD refit). Table 4.13 gives the cosmic ray background estimated using the above method in the region of the cross section analysis, for 1990 and 1991.

The cosmic background in the region of the asymmetry analysis was also estimated using the above method, giving a total background of $(0.53 \pm 0.1)\%$ in 1990, and $(0.23 \pm 0.08)\%$ in 1991. The $\cos\theta$ dependence of this background was assumed to be given by $1 - \cos^2\theta$, as determined in [43].

These estimates of the cosmic ray background are for the whole data sample, including data from all centre of mass energies. The estimated total number of cosmic ray muons is divided between the different energy points according to the integrated luminosity at each point, assuming that integrated luminosity is a linear function of time.

4.8.3 Electron Background

The electron background was estimated by applying the $\mu^+\mu^-$selection cuts C1-C5σ and MU to 5000 simulated e^+e^-events. Only 1 of the e^+e^-events passed the cuts, giving an almost negligible e^+e^-background of $(0.02 \pm 0.02)\%$.

Vertex cut (cm)	$\mu^+\mu^-$ candidates	Difference from 1.5*cm* cut	Cosmic estimate	
			1.5*cm* cut	0.4*cm* cut
3.0	3817	59	59	16
2.5	3796	38	57	15
2.0	3778	20	60	16
1.5	3758	0		

Table 4.11: Number of $\mu^+\mu^-$candidates selected for varying values of the impact parameter cut in $R\phi$, and estimates of the cosmic background assuming a final cut of 1.5 and 0.4*cm*, in 1990.

Vertex cut (cm)	$\mu^+\mu^-$ candidates	Difference from 1.5*cm* cut	Cosmic estimate	
			1.5*cm* cut	0.4*cm* cut
3.0	3383	33	33	9
2.5	3368	18	27	75
2.0	3360	10	30	16
1.5	3350	0		

Table 4.12: Number of $\mu^+\mu^-$candidates selected for varying values of the impact parameter cut in $R\phi$, and estimates of the cosmic background assuming a final cut of 1.5 and 0.4*cm*, in 1991.

Year	Cosmic ray Background
1990	$(0.4 \pm 0.1)\%$
1991	$(0.3 \pm 0.1)\%$

Table 4.13: Percentage cosmic ray background in the region of the cross section analysis, for 1990 and 1991.

4.8.4 Summary of Correction Factors

To apply the θ dependent correction factors, the $\mu^+\mu^-$events are divided into 48 bins of equal width between the upper and lower $\cos\theta$ limits, where $\cos\theta$ for the event is defined by the negative track. The $\cos\theta$ dependent correction factors are also calculated in 48 $\cos\theta$ bins, and are applied bin by bin, since there are correlations between the various inefficiencies. The final corrected number of $\mu^+\mu^-$events may then be calculated. Table 4.14 gives the total $\cos\theta$ dependent efficiencies, calculated assuming a folded $1 + \cos^2\theta$ distribution of tracks in $\mu^+\mu^-$events. The overall trigger efficiencies are summarised above in table 4.9 Note that because of the correlations between the various inefficiencies, the cross sections given by this analysis are not the same as those obtained by taking the number of $\mu^+\mu^-$events and simply correcting for the overall efficiencies.

Year	TPC ϕ loss	Track Reconstruction	Muon Identification
1990	$(96.6 \pm 0.7)\%$	$(100.0^{+0}_{-0.2})\%$	$(98.96 \pm 0.20)\%$
1991	$(96.4 \pm 0.7)\%$	$(98.8 \pm 0.28)\%$	$(97.53 \pm 0.22)\%$

Table 4.14: Overall track reconstruction and muon identification efficiencies for each period, and the data with which the efficiencies were calculated.

The $e^+e^- \rightarrow e^+e^-\mu^+\mu^-$ background has been estimated using simulated two-photon events[44], and found to be negligible. The $e^+e^- \rightarrow e^+e^-$ and has also been measured and found to be very small. The remaining non θ dependent correction factors are to account for the momentum cut, $\tau^+\tau^-$background, cosmic background and the upper limit on the number of charged tracks.

The $\tau^+\tau^-$background is assumed to have the same θ dependence as the $\mu^+\mu^-$sample, and to be independent of $\sqrt{s}$, so an overall correction factor is applied, as summarised in table 4.15

The correction factor applied to account for the loss of events due to the requirement that the number of charged tracks is ≤ 5 is (1.0013 ± 0.0004).

The correction factor due to the momentum and acolinearity cuts is dependent on $\sqrt{s}$, but is assumed to be independent of θ. The correction factor for each centre of mass energy was calculated using the simulated data and is given in table 4.16

1990	0.979 ± 0.002)
1991	0.986 ± 0.001)

Table 4.15: Correction factors for the $\tau^+\tau^-$background.

Energy point	Correction
1	1.0384 ± 0.002
2	1.0377 ± 0.002
3	1.0371 ± 0.002
4	1.0369 ± 0.002
5	1.0360 ± 0.002
6	1.0354 ± 0.002
7	1.0348 ± 0.002

Table 4.16: Correction factors for losses due to momentum and acolinearity cuts

4.8.5 Resulting distribution of events

Before the above corrections have been applied, the $\cos\theta$ distribution of the negative charged track in the $\mu^+\mu^-$candidates selected from 1990 data (at the LEP energy point nearest the Z^0peak) is as shown in fig 4.26 (a). The total correction factor is shown, as a function of $\cos\theta$, in fig 4.26 (b). Applying this correction factor gives the distribution shown in fig 4.26 (c). Figures 4.27 (a)-(c) show the same distributions for the 1991 data.

Now that the $\mu^+\mu^-$selection criteria have been chosen, and all the necessary efficiencies and backgrounds to the $e^+e^-\rightarrow\mu^+\mu^-$ channel have been studied, $\mu^+\mu^-$candidates may be selected from the data, and values for the cross sections and asymmetries for this channel at several centre of mass energies may be calculated. The cross section and asymmetry results are given in the following sections.

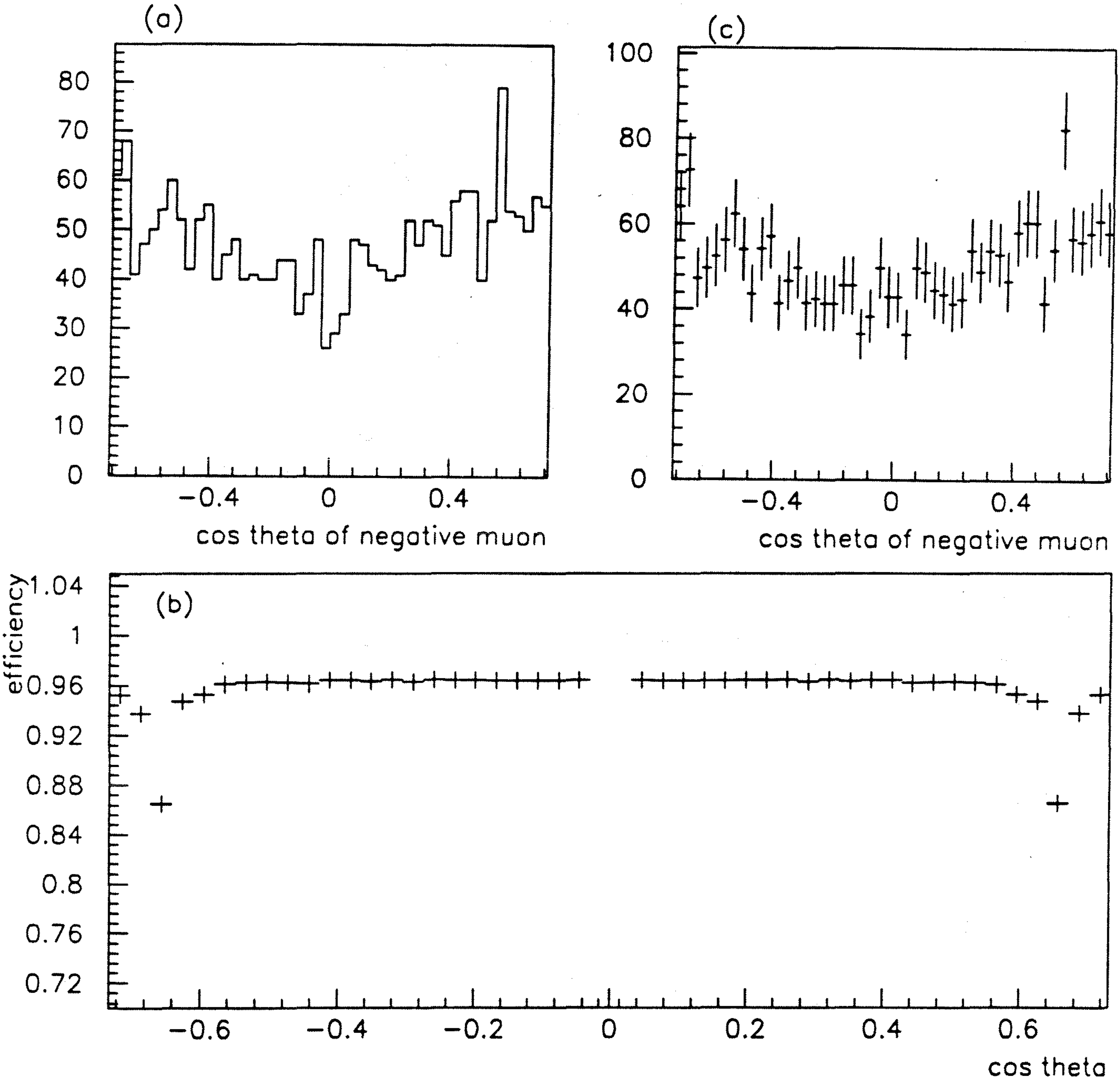

Figure 4.26: (a) $\cos\theta$ distribution of negative charged tracks in $\mu^+\mu^-$candidate events in 1990, (b) Correction factor versus $\cos\theta$, and (c) Corrected $\cos\theta$ distribution.

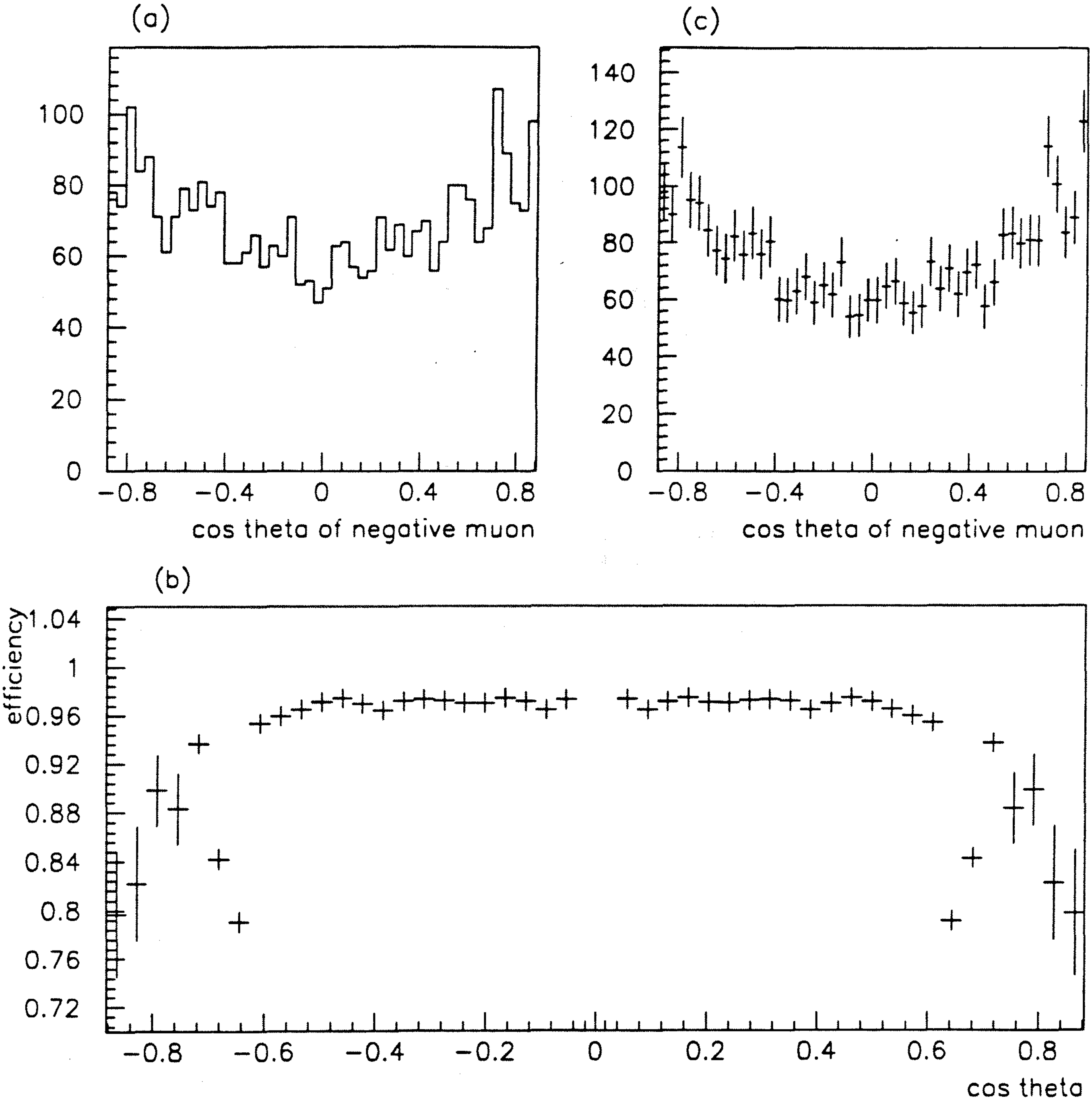

Figure 4.27: (a) $\cos\theta$ distribution of negative charged tracks in $\mu^+\mu^-$candidate events in 1991, (b) Correction factor versus $\cos\theta$, and (c) Corrected $\cos\theta$ distribution.

4.9 Numbers of $\mu^+\mu^-$Candidates Selected

Table 4.17 gives the total number of $\mu^+\mu^-$events selected from the 1990 and 1991 data samples.

Year	Number for σ_μ	Number for A_{FB}	Total integrated luminosity (pb^{-1})
1990	2691	3995	4.13
1991	2160	3529	1.95
Total	4851	7524	6.08

Table 4.17: Numbers of $\mu^+\mu^-$events selected for the measurement of σ_μ and A_{FB}, and total integrated luminosity for the cross section measurement.

4.10 σ_μ Results

The cross sections are obtained by:

- Selecting $\mu^+\mu^-$events with the cuts $C1 - C5\sigma$ and MU described in sections 4.4 and 4.5.5, and storing the $\cos\theta$ of the negative muon in a 48 bin histogram.
- Applying the θ dependent corrections for the track reconstruction efficiency in the fiducial volume of the TPC, losses in the TPC sector boundaries, muon identification efficiency and trigger efficiency (in 1991) bin by bin to the above histogram.
- Correcting for the loss of events at $\theta = 90°$ by assuming a $1 + \cos^2\theta$ distribution over the $(43°, 137°)$ region.
- Finding the contents of the corrected histogram, and then making global corrections for the remaining losses and backgrounds, i.e. cosmic ray muon, $\tau^+\tau^-$and e^+e^-backgrounds, and losses due to the momentum and acolinearity cut, upper limit on the number of charged tracks, and trigger efficiency (in 1990).

Period	$\sqrt{s}$ (GeV)	No. of $\mu^+\mu^-$events	Luminosity $(nb)^{-1}$	σ_μ (nb)	σ_μ (corr to 4π)
1990	88.221	36	251	0.158 ± 0.029	0.245 ± 0.046
1990	89.216	84	336	0.272 ± 0.033	0.421 ± 0.051
1990	90.217	216	330	0.720 ± 0.055	1.115 ± 0.085
1990	91.212	1933	2145	0.984 ± 0.025	1.522 ± 0.039
1990	92.207	211	318	0.718 ± 0.055	1.110 ± 0.085
1990	93.209	111	327	0.366 ± 0.039	0.566 ± 0.060
1990	94.200	100	419	0.248 ± 0.028	0.383 ± 0.043
1991	91.243	2160	1946	1.231 ± 0.030	1.476 ± 0.036

Table 4.18: Number of $\mu^+\mu^-$candidates and cross section results for 8 different centre of mass energies, in the θ region covered by the analysis, and corrected to the full solid angle.

- Dividing by the luminosity to give a cross section for the angular region used in the analysis.
- Correcting the above cross section to 4π solid angle, by dividing by a factor

$$\frac{3}{4}\left(\cos\alpha + \frac{\cos^3\alpha}{3}\right)$$

where α is the lower θ limit in the analysis. This assumes that the negative muon tracks have a $1 + \cos^2\theta + r\cos\theta$ distribution.

The uncorrected numbers of $\mu^+\mu^-$candidates selected at each energy point in 1990 and 1991 are given in table 4.17, together with the corresponding luminosity and cross section result before and after the correction to 4π solid angle.

The errors quoted in the above table are purely statistical. Contributions to the systematic error on the cross section are summarised in table 4.19, their origin being the statistical error on the calculation of the corresponding correction. One exception is the luminosity systematic error, contributions to which were summarised in chapter 2.

Source of error	Systematic error on σ_μ (%)	
	1990	1991
Muon identification	0.2	0.2
Trigger	0.3	0.1
$\tau^+\tau^-$background	0.2	0.1
Momentum, acol cuts	0.2	0.2
Cosmic background	0.1	0.1
Track reconstruction	0.1	0.3
Total from analysis	0.5	0.5
Luminosity	0.7	0.6
Total	0.9	0.8

Table 4.19: Contributions to the systematic error on the cross section

4.11 Asymmetry Measurements

Events for the asymmetry measurements were selected using the cuts $C1-C5A_{FB}$ and MU described in sections 4.4 and 4.5.5. The asymmetry was determined using the log likelihood method, using the likelihood function given in equation 4.8

$$\mathcal{L} = \frac{3}{8}\left(1+\cos^2\theta + \frac{8}{3}A_{FB}\cos\theta\right) + \frac{3}{4}C\left(1-\cos^2\theta\right) \qquad (4.8)$$

where the first term is the expected $\cos\theta$ distribution for the negative muon in $\mu^+\mu^-$events, and the second term describes the cosmic ray muon background. C is the ($\sqrt{s}$ dependent) fraction of cosmic ray muons measured to be in the sample of events used for determination of A_{FB}, from section 4.8.2.

Using this likelihood function, the asymmetry A_{FB} may be extracted by maximising

$$\mathcal{LL} = \sum_{i=1}^{N} \log \mathcal{L}_i \qquad (4.9)$$

at each energy point, where N is the number of $\mu^+\mu^-$candidates at that point. The statistical error on A_{FB} is the change in A_{FB} when $\mathcal{LL}$ is lowered by 0.5 from its maximum value.

When using the log likelihood method, knowledge of the detection efficiencies is not necessary, provided that they are symmetric about $\cos\theta = 0$. To a large extent this symmetry is imposed by the event selection, since the events are required to have two muon candidates, back to back within 10°. The results of this measurement of A_{FB} are given in table 4.20.

Year	$\sqrt{s}$ (GeV)	No. of $\mu^+\mu^-$events	A_{FB}
1990	88.221	59	-0.11 ± 0.13
1990	89.216	125	-0.22 ± 0.09
1990	90.217	303	-0.10 ± 0.06
1990	91.212	2857	0.023 ± 0.019
1990	92.207	325	-0.009 ± 0.055
1990	93.209	188	0.11 ± 0.07
1990	94.200	138	0.23 ± 0.08
1991	91.243	3529	0.006 ± 0.015

Table 4.20: Number of $\mu^+\mu^-$candidates and results for the forward - backward asymmetry given by the log - likelihood method for 8 different centre of mass energies.

Possible sources of systematic error on A_{FB} are:

- Charge misidentification - a very safe estimate of 0.16%, from section 4.6.
- Differences in identification efficiency for positive and negative muons, in the forward and backward hemispheres. For example, if the efficiency for identification of negative muons was 95% where $\cos\theta < 0$, and 100% where $\cos\theta > 0$, and the efficiency for positive muons was 100% everywhere. A safe estimate of 0.5% in 1990 and 1991. This number was studied by repeating the asymmetry analysis with a lower ($15GeV$) momentum cut, assuming that this would reduce such effects.
- Background events with an asymmetry different to that of the $\mu^+\mu^-$asymmetry. The cosmic background is taken into account in the likelihood function, and the $\tau^+\tau^-$background is assumed to have the same asymmetry as the $\mu^+\mu^-$events. Studies of the simulated data revealed that the effect of the $\tau^+\tau^-$background was negligible, and the effect of the cosmic background was also found to be very small, by observing the effect of increasing the cosmic background (by increasing the VD vertex cut) on the measured

asymmetry, with the cosmic background term removed from the likelihood function.

The total systematic error on the asymmetry measurements was taken to be 0.5% in both 1990 and 1991[16].

4.12 Cross section as a function of $\cos\theta$

The cross section as a function of $\cos\theta$ is obtained in the same way as the total cross section, except that a $\cos\theta$ dependent cosmic background correction is applied, and the cross section is integrated over a number of equal regions in $\cos\theta$, and divided by the bin width, to give $\Delta\sigma/\Delta\cos\theta$.

Two sets of $\Delta\sigma/\Delta\cos\theta$ measurements were made, for two different choices of the number of bins at each energy point. For the first set, the cross section was measured in two bins at each energy point - this is of course equivalent to measuring the cross section, and the asymmetry using the counting method. The first set of measurements are given in table 4.21 For the second set of measurements, the number of bins at each energy point were chosen to make the number of events in each bin roughly the same, giving each bin a roughly equal weight in the fit . Table 4.22 gives the cross section for each bin, at each energy point, together with the upper and lower $\cos\theta$ limits for the bin.

The systematic error is divided into two components for use in the fitting procedure.

- The overall systematic error is 0.8% in 1990 and 0.6% in 1991. These figures are the combined systematic errors on the trigger efficiency (in 1990), $\tau^+\tau^-$background, momentum and acolinearity cut corrections, cosmic ray background and the luminosity.

- The contribution to the systematic error which is calculated for each $\cos\theta$ bin separately. The contributions to this error are the errors on the $\cos\theta$ dependent corrections, that is the trigger efficiency (in 1991), muon identification efficiency, and track reconstruction efficiency. Because of

---

[16] N.B. this is an absolute error, not a fraction of the asymmetry itself.

the back - to - back topology of $\mu^+\mu^-$events, these errors are essentially correlated in back - to - back $\cos\theta$ bins, and this is taken into account in the propagation of the systematic errors when fitting to these results. This error is of the order of 0.5% per bin when $\Delta\sigma/\Delta\cos\theta$ is calculated in 24 bins at the peak points.

In the next chapter, fits to the cross section and asymmetry results obtained above will be described.

Bin	Lower $\cos\theta$	Upper $\cos\theta$	$\mu^+\mu^-$ events	$\Delta\sigma/\Delta\cos\theta$ (nb)
Point 1 Energy = 88.221GeV Luminosity = $251nb^{-1}$				
1	-0.7314	0.0000	23	0.140 ± 0.033
2	0.0000	0.7314	13	0.079 ± 0.025
Point 2 Energy = 89.216GeV Luminosity = $336nb^{-1}$				
1	-0.7314	0.0000	49	0.221 ± 0.035
2	0.0000	0.7314	35	0.154 ± 0.029
Point 3 Energy = 90.217GeV Luminosity = $330nb^{-1}$				
1	-0.7314	0.0000	117	0.540 ± 0.056
2	0.0000	0.7314	99	0.448 ± 0.050
Point 4 Energy = 91.212GeV Luminosity = $2145nb^{-1}$				
1	-0.7314	0.0000	934	0.653 ± 0.024
2	0.0000	0.7314	999	0.695 ± 0.025
Point 5 Energy = 92.207GeV Luminosity = $318nb^{-1}$				
1	-0.7314	0.0000	111	0.519 ± 0.055
2	0.0000	0.7314	100	0.466 ± 0.052
Point 6 Energy = 93.209GeV Luminosity = $327nb^{-1}$				
1	-0.7314	0.0000	50	0.227 ± 0.036
2	0.0000	0.7314	61	0.276 ± 0.040
Point 7 Energy = 94.200GeV Luminosity = $419nb^{-1}$				
1	-0.7314	0.0000	40	0.133 ± 0.024
2	0.0000	0.7314	60	0.208 ± 0.030
Point 8 Energy = 91.243GeV Luminosity = $1946nb^{-1}$				
1	-0.8829	0.0000	1075	0.695 ± 0.024
2	0.0000	0.8829	1085	0.703 ± 0.024

Table 4.21: $\Delta\sigma/\Delta\cos\theta$ results for two bins (one forward, one backward) at each energy point.

Bin	Lower $\cos\theta$	Upper $\cos\theta$	$\mu^+\mu^-$ events	$\Delta\sigma/\Delta\cos\theta$ (nb)
Point 1 Energy = 88.221GeV Luminosity = $251nb^{-1}$				
1	-0.7314	0.0000	23	0.140 ± 0.033
2	0.0000	0.7314	13	0.079 ± 0.025
Point 2 Energy = 89.216GeV Luminosity = $336nb^{-1}$				
1	-0.7314	0.0000	49	0.221 ± 0.035
2	0.0000	0.7314	35	0.154 ± 0.029
Point 3 Energy = 90.217GeV Luminosity = $330nb^{-1}$				
1	-0.7314	-0.3657	69	0.620 ± 0.084
2	-0.3657	0.0000	48	0.460 ± 0.074
3	0.0000	0.3657	37	0.343 ± 0.063
4	0.3657	0.7314	62	0.550 ± 0.078
Point 4 Energy = 91.212GeV Luminosity = $2145nb^{-1}$				
1	-0.7314	-0.6704	106	0.889 ± 0.097
2	-0.6704	-0.6095	75	0.657 ± 0.085
3	-0.6095	-0.5485	79	0.654 ± 0.082
4	-0.5485	-0.4876	94	0.774 ± 0.089
5	-0.4876	-0.4266	82	0.677 ± 0.084
6	-0.4266	-0.3657	76	0.625 ± 0.080
7	-0.3657	-0.3047	82	0.675 ± 0.083
8	-0.3047	-0.2438	68	0.560 ± 0.076
9	-0.2438	-0.1828	72	0.593 ± 0.078
10	-0.1828	-0.1219	79	0.651 ± 0.082
11	-0.1219	-0.0609	60	0.494 ± 0.071
12	-0.0609	0.0000	61	0.592 ± 0.120
13	0.0000	0.0609	53	0.515 ± 0.111
14	0.0609	0.1219	84	0.685 ± 0.084
15	0.1219	0.1828	74	0.601 ± 0.078
16	0.1828	0.2438	70	0.566 ± 0.076
17	0.2438	0.3047	83	0.669 ± 0.082
18	0.3047	0.3657	88	0.707 ± 0.084
19	0.3657	0.4266	86	0.688 ± 0.083
20	0.4266	0.4876	95	0.761 ± 0.087
21	0.4876	0.5485	75	0.598 ± 0.077
22	0.5485	0.6095	109	0.872 ± 0.093
23	0.6095	0.6704	92	0.772 ± 0.090
24	0.6704	0.7314	90	0.727 ± 0.086
Point 5 Energy = 92.207GeV Luminosity = $318nb^{-1}$				
1	-0.7314	-0.3657	71	0.662 ± 0.088
2	-0.3657	0.0000	40	0.375 ± 0.066
3	0.0000	0.3657	45	0.419 ± 0.070
4	0.3657	0.7314	55	0.510 ± 0.077

Bin	Lower $\cos\theta$	Upper $\cos\theta$	$\mu^+\mu^-$ events	$\Delta\sigma/\Delta\cos\theta$ (nb)
Point 6 Energy = 93.209GeV Luminosity = $328nb^{-1}$				
1	-0.7314	0.0000	50	0.227 ± 0.036
2	0.0000	0.7314	61	0.276 ± 0.040
Point 7 Energy = 94.200GeV Luminosity = $419nb^{-1}$				
1	-0.7314	0.0000	40	0.133 ± 0.024
2	0.0000	0.7314	60	0.208 ± 0.030
Point 8 Energy = 91.243GeV Luminosity = $1946nb^{-1}$				
1	-0.8829	-0.8094	92	0.833 ± 0.097
2	-0.8094	-0.7358	120	0.951 ± 0.097
3	-0.7358	-0.6622	109	0.863 ± 0.092
4	-0.6622	-0.5886	91	0.758 ± 0.089
5	-0.5886	-0.5151	111	0.828 ± 0.088
6	-0.5151	-0.4415	96	0.706 ± 0.081
7	-0.4415	-0.3679	85	0.630 ± 0.076
8	-0.3679	-0.2943	70	0.514 ± 0.069
9	-0.2943	-0.2207	77	0.567 ± 0.072
10	-0.2207	-0.1472	72	0.530 ± 0.070
11	-0.1472	-0.0736	82	0.605 ± 0.075
12	-0.0736	0.0000	70	0.557 ± 0.105
13	0.0000	0.0736	70	0.584 ± 0.110
14	0.0736	0.1472	75	0.549 ± 0.071
15	0.1472	0.2207	77	0.560 ± 0.071
16	0.2207	0.2943	87	0.630 ± 0.076
17	0.2943	0.3679	83	0.598 ± 0.073
18	0.3679	0.4415	88	0.638 ± 0.076
19	0.4415	0.5151	82	0.588 ± 0.073
20	0.5151	0.5886	109	0.792 ± 0.085
21	0.5886	0.6622	96	0.766 ± 0.087
22	0.6622	0.7358	97	0.746 ± 0.085
23	0.7358	0.8094	113	0.870 ± 0.092
24	0.8094	0.8829	108	0.943 ± 0.102

Table 4.22: $\Delta\sigma/\Delta\cos\theta$ results for 2, 2, 4, 24, 4, 2, 2, and 24 bins, at energy points 1-8 respectively

DELPHI Interactive Analysis

Beam: 45.7 GeV
Run: 21187
Evt: 1981
DAS : 2-May-1991
18:05:17
Proc: 4-Jun-1992
Scan: 4-Jun-1992

TD	TE	TS	TV	ST	PA
0	35		5	0	
(0)	(35)		(5)	(0)	
0	0		0	0	
(0)	(3)		(3)	(0)	

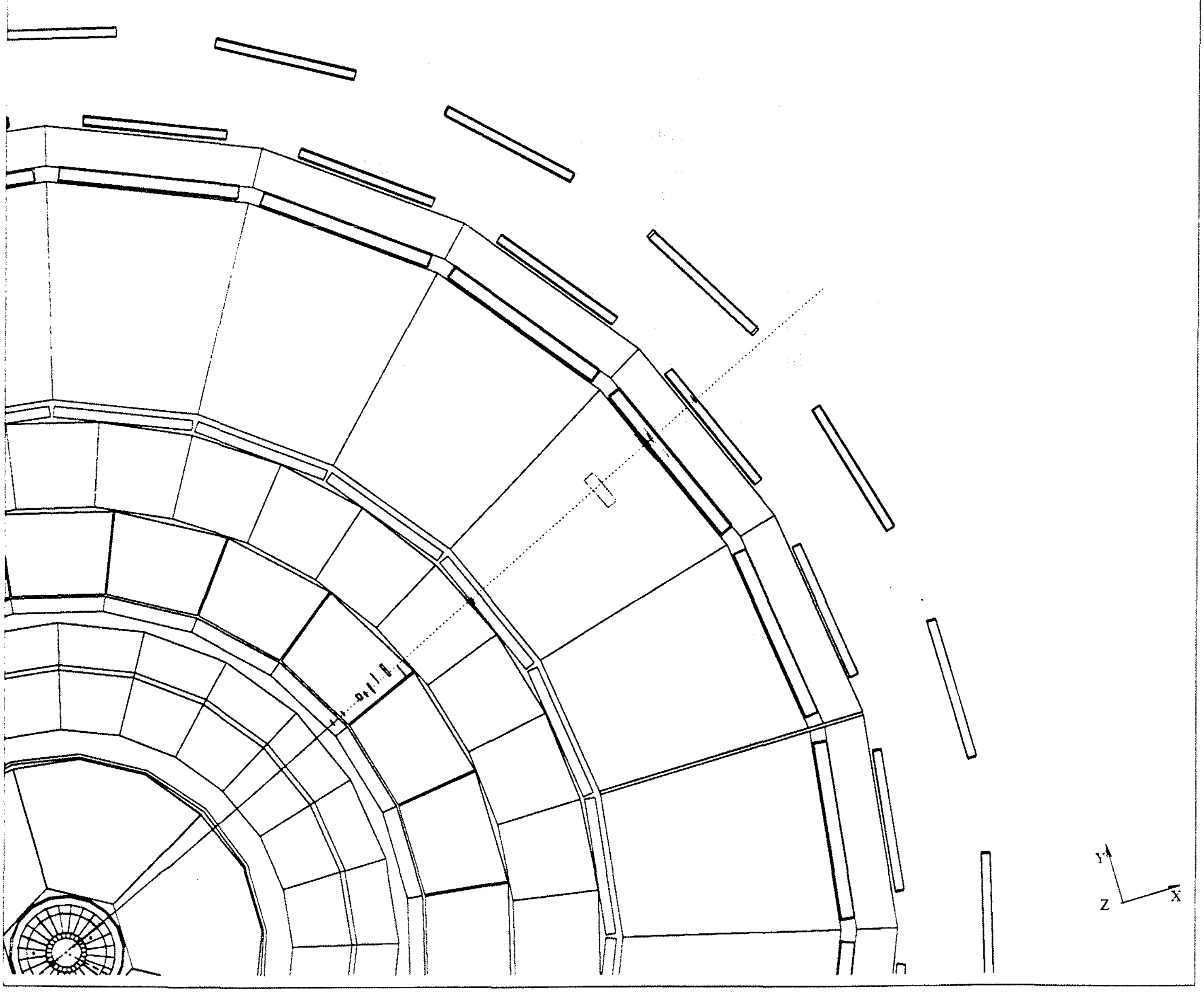

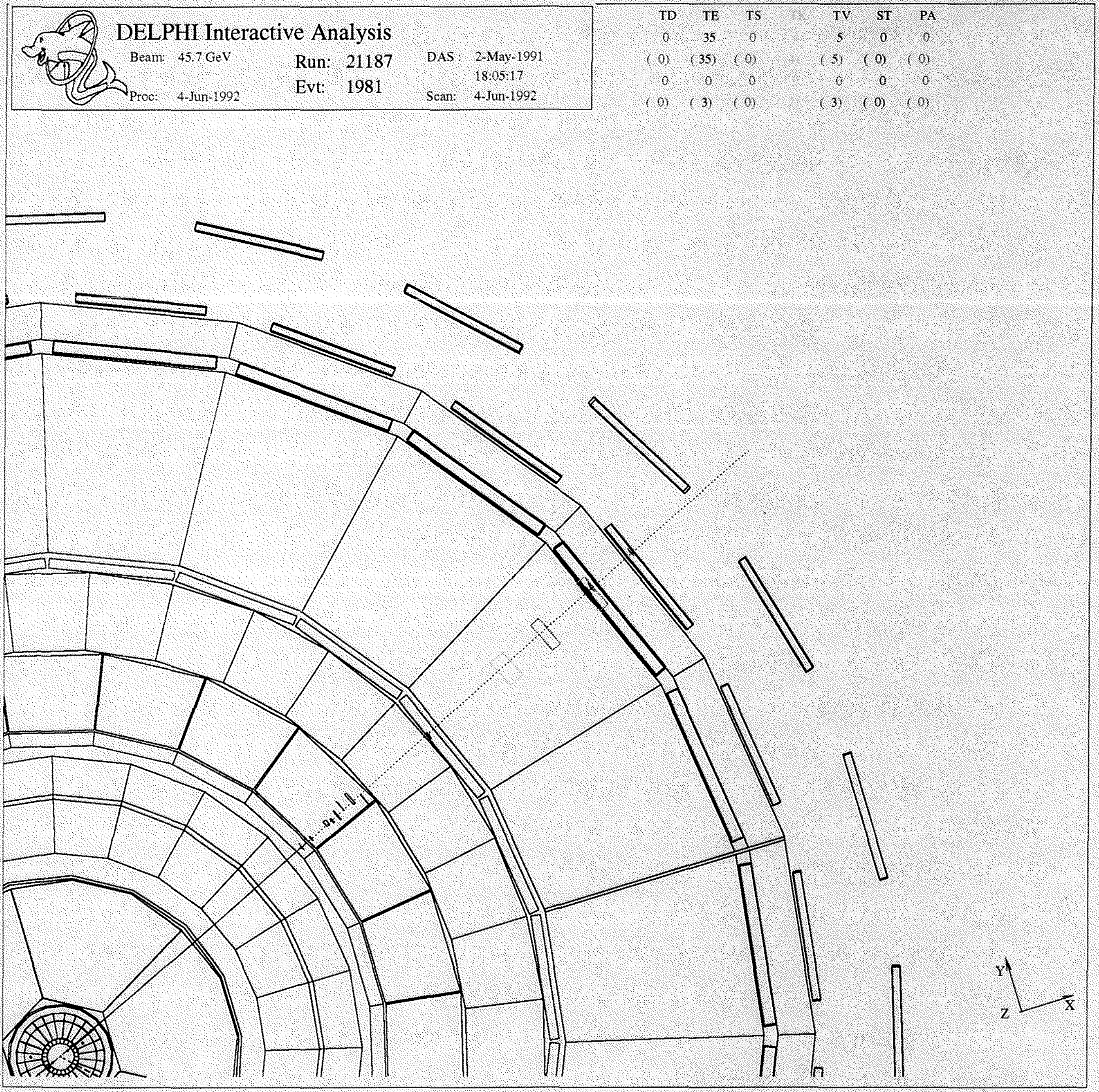

DELPHI Interactive Analysis

Beam: 45.7 GeV
Run: 21187
Evt: 1981
Proc: 4-Jun-1992
DAS : 2-May-1991
18:05:17
Scan: 4-Jun-1992

TD	TE	TS	TK	TV	ST	PA
0	35	0	4	5	0	0
(0)	(35)	(0)	(4)	(5)	(0)	(0)
0	0	0	0	0	0	0
(0)	(3)	(0)	(2)	(3)	(0)	(0)

Chapter 5

Data Analysis

This chapter contains the results of IBA fits to the cross section and asymmetry results, performed to extract the vector and axial vector couplings of the Z^0 to charged leptons, and the leptonic width. The results obtained are then compared with the MSM predictions for these quantities. The fitting was performed using the Minuit function minimisation package[1] [45]. The results from similar analyses performed by other experiments may be found in [49].

5.1 Fits

In some of the following fits, values of M_Z and Γ_Z were taken from a fit to the 1991 DELPHI hadronic data, from [47]. The values are:

- $\mathbf{M_Z} = (91.187 \pm 0.010(stat + syst))GeV$
- $\mathbf{\Gamma_Z} = (2.493 \pm 0.012(stat + syst))GeV$

where approximately $6MeV$ of the systematic error in M_Z is given by the systematic error in E_{cm} in 1991.

Where MSM predictions are given, they are calculated assuming $M_Z = (91.187 \pm 0.010)GeV$, $m_{top} = (139 \pm 38)GeV$[23], and with M_H having a flat distribution between 50 and 1000 GeV. All of the following fits assume lepton universality.

---

[1] All the errors given here are from the output of MIGRAD. Since the errors are in fact very nearly symmetric for the parameters fitted here, there is negligible difference between the MIGRAD errors and the full error calculation performed by MINOS

5.1.1 Fit I - 3 parameter fit to σ_μ

The first fit performed was a fit to the cross section measurements at 8 centre of mass energies, with free parameters M_Z, Γ_Z and $(\Gamma_l)^{\frac{1}{2}}$. The results of the fit are given in tables 5.1 and 5.2, and shown in figure 5.1. Also given in table 5.1 are the M_Z and Γ_Z values obtained from the DELPHI hadronic data[47]. The $e^+e^- \to \mu^+\mu^-$ results can be seen to be consistent with the hadronic results, although of course the statistical errors are much larger.

Parameter	Result from σ_μ data	Result from hadronic data
M_Z	$91.046 \pm 0.074)GeV$	$91.187 \pm 0.010)GeV$
Γ_Z	$2.471 \pm 0.12)GeV$	$2.493 \pm 0.012)GeV$
$(\Gamma_l)^{\frac{1}{2}}$	$83.5 \pm 3.6)MeV$	-
χ^2/N_{dof}	$5.2/(8-3)$	

Table 5.1: Results of a 3 parameter fit to the σ_μ results (statistical errors only), together with values of M_Z and Γ_Z given by an analysis of the DELPHI 1991 hadronic data for comparison[47].

Parameter	M_Z	Γ_Z	Γ_l
M_Z	1	0.295	0.248
Γ_Z	0.295	1	0.980
Γ_l	0.248	0.980	1

Table 5.2: Correlation matrix for 3 parameter fit I to the σ_μ results

5.1.2 Fit II - 1 parameter fit to σ_μ

In the second fit to the cross section data, M_Z and Γ_Z were taken from the DELPHI hadronic data, and a one-parameter fit to determine the best value for Γ_l was performed, assuming lepton universality. The systematic error in the cross section measurements was propagated by introducing a factor *Anor* representing the absolute normalisation, which multiplied the theoretical cross section, and was allowed to vary. The variation in this factor was constrained by introducing an additional term in the χ^2, given by $\frac{(Anor-1)^2}{\delta_{sys}}$, where δ_{sys} is the systematic error in the cross sections. When the fit was repeated with this factor free, a new and larger error was returned, from which the contribution due to the systematic error was extracted. There is an additional contribution to the systematic error which is due to the errors on M_Z and Γ_Z and their correlation with Γ_l. This contribution was found to be $0.36MeV$, mainly from the error on Γ_Z.

The result of this fit is given in table 5.3, and shown figure 5.2 (a), where the fit result is shown as a curve superimposed on a plot of the cross sections as a function of the centre of mass energy.

Parameter	Result from σ_μ data	MSM prediction
Γ_l	$84.22 \pm 0.69(stat) \pm 0.40(\sigma syst) \pm 0.36(M_Z, \Gamma_Z)MeV$	$83.6 \pm 0.4)MeV$
χ^2/N_{dof}	$8.8/(8-1)$	-

Table 5.3: Results of a 1 parameter fit to the σ_μ results, and the MSM prediction of Γ_l for comparison.

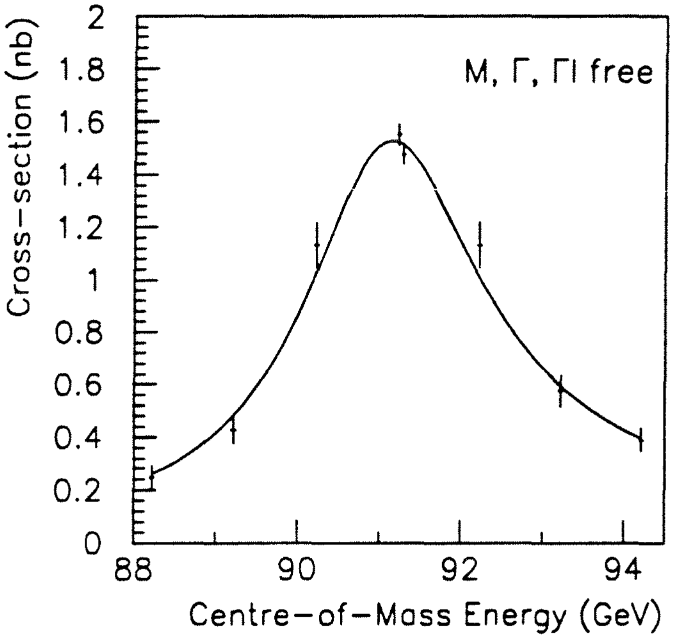

Figure 5.1: Result of Fit I to the muon cross sections.

5.1.3 Fit III - Combined Fit to σ_μ and A_{FB}

The next fit uses both the cross section and asymmetry measurements. ZFITTER calculates σ_μ and A_{FB} as a function of M_Z, Γ_Z, s, $\bar{v}_l^2$ and $\bar{a}_l^2$. The momentum and acolinearity cuts used in the event selection were also input to ZFITTER for the calculation of the forward - backward asymmetry. M_Z, Γ_Z and s were again provided by the DELPHI hadronic results and the LEP group, and a two-parameter fit was performed to obtain values for $\bar{v}_l^2$ and $\bar{a}_l^2$, assuming lepton universality.

The results of this fit are shown in table 5.4, and the correlation matrix in table 5.5. The systematic errors include the effect of the uncertainty on M_Z and Γ_Z, which contribute mainly to the uncertainties on $\bar{v}_l^2$ and $\bar{a}_l^2$ respectively (0.0001 on $\bar{v}_l^2$ from the uncertainty in M_Z, and 0.001 on $\bar{a}_l^2$, from the uncertainty in Γ_Z).

The cross sections and asymmetry results are shown in figure 5.2, with the curves resulting from fit III superimposed. (The curve resulting from fit II is indistinguishable from that resulting from fit III.) Figure 5.3 shows the result of this fit, and the 70 and 90% confidence level contours in the $\bar{v}_l$ - $\bar{a}_l$ plane (the contours take into account the statistical errors only). The sign of $\bar{v}_l$ has been determined by other experiments [48]. The MSM prediction for $\bar{v}_l$ and $\bar{a}_l$ is also shown, for varying values of the top and Higgs masses - smaller top masses correspond to smaller absolute values of $\bar{a}_l$, and the Higgs mass increases from left to right. The fit results can be seen to be in good agreement with the Minimal Standard Model for a wide range of top and Higgs masses. If the MSM is assumed, then the data from the $Z^0 \rightarrow \mu^+\mu^-$ channel alone may be used to restrict the top mass to lie between 50 to 310 GeV, at 90% confidence.

Parameter	Result from fit III
$\bar{v}_l^2$	$0.0017 \pm 0.0009(stat) \pm 0.0001(syst)$
$\bar{a}_l^2$	$0.2517 \pm 0.0023(stat) \pm 0.0016(syst)$
Equivalently	
ρ_{eff}	$1.007 \pm 0.011\ (stat + syst)$
$\sin^2\theta_W{}^{eff}$	$0.2295^{+0.0064}_{-0.0049}\ (stat + syst)$
χ^2/N_{dof}	$14.7/(16-2)$
$\bar{v}_l$	$-0.042^{+0.014}_{-0.010}(stat) \pm 0.001(syst)$
$\bar{a}_l$	$-0.5017 \pm 0.0023(stat) \pm 0.0016(syst)$

Table 5.4: Results of a 2 parameter fit performed to extract $\bar{v}_l^2$ and $\bar{a}_l^2$ from the σ_μ and A_{FB} measurements. The equivalent values of ρ_{eff} and $\sin^2\theta_W{}^{eff}$ are also given.

Parameter	$\bar{v}_l^2$	$\bar{a}_l^2$
$\bar{v}_l^2$	1	-0.40
$\bar{a}_l^2$	-0.40	1

Table 5.5: Correlation matrix for 2 parameter fit III to the σ_μ and A_{FB} results

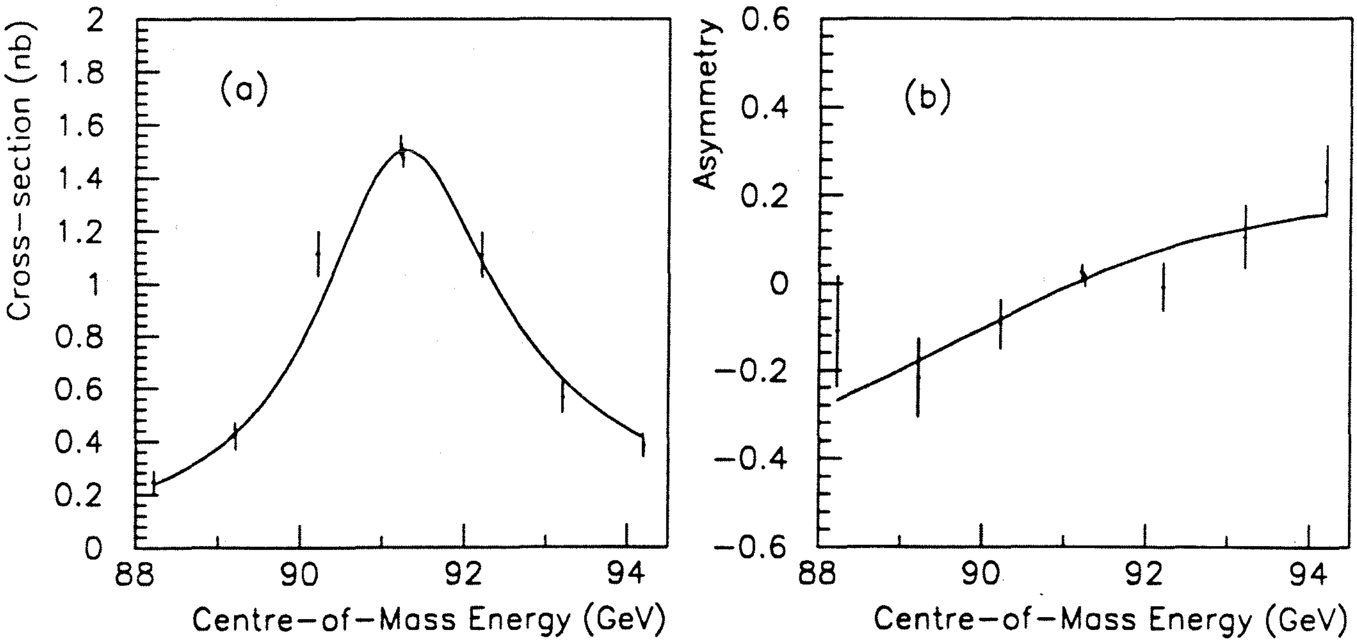

Figure 5.2: (a) $Z^0 \to \mu^+\mu^-$ cross sections (corrected to 4π) and (b) $Z^0 \to \mu^+\mu^-$ forward-backward asymmetries (corrected to 4π, but not for momentum and acolinearity cut) as a function of centre of mass energy. The curves are the results of a combined fit to both sets of data (fit III).

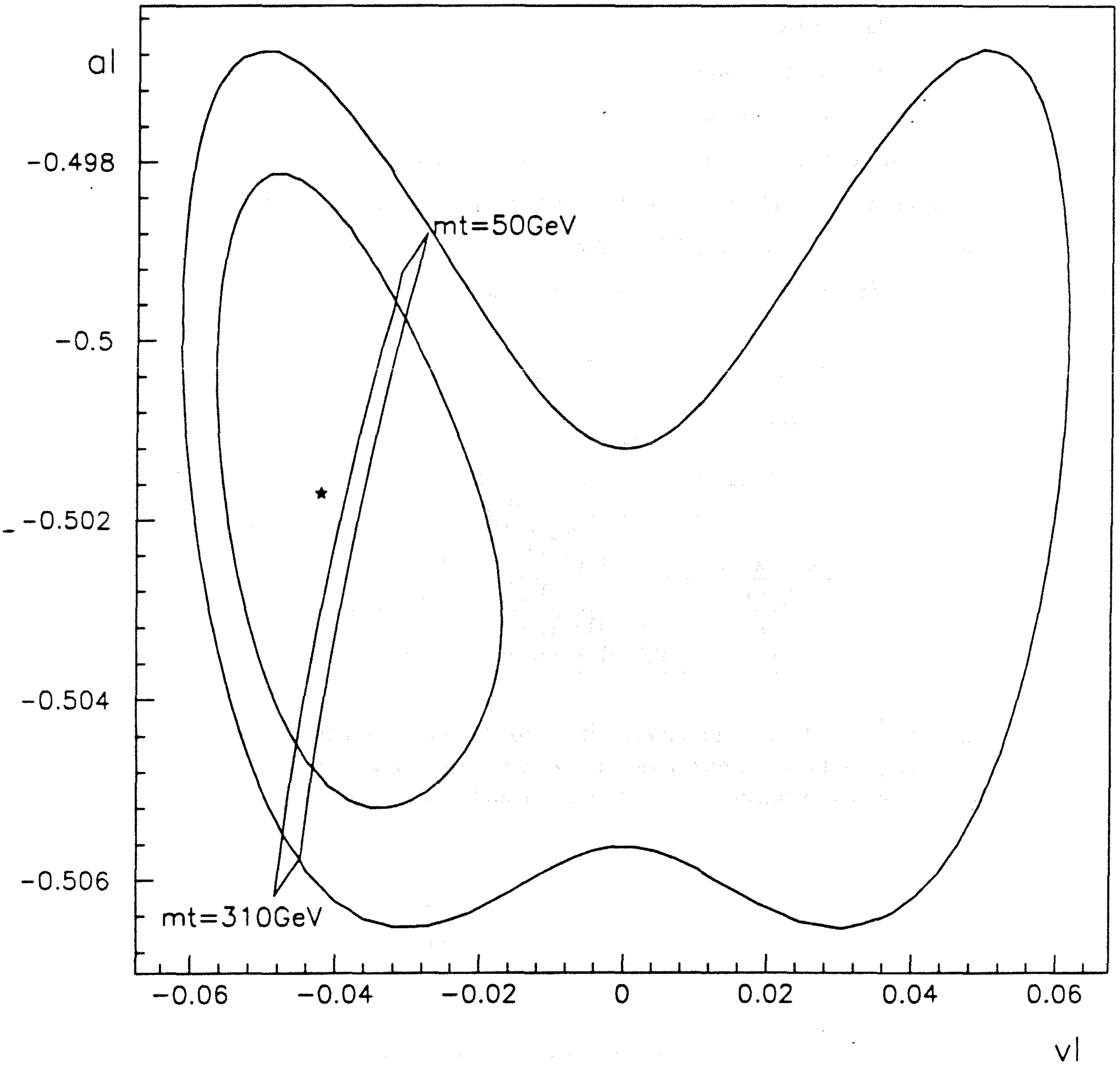

Figure 5.3: Result of the combined fit to the muon cross sections and asymmetries. The star marks the best value, and 70% and 90% confidence level contours are shown. MSM predictions for values of the top mass between 50 and 310GeV, and values of the Higgs mass between 50 and 1000 GeV are also marked.

5.1.4 Fits IV and V - Differential Cross Section

In the fits to $\Delta\sigma/\Delta\cos\theta$, ZFITTER is used to calculate $\Delta\sigma/\Delta\cos\theta$ as a function of s, $\bar{v}_l^2$, $\bar{a}_l^2$ and the upper and lower $\cos\theta$ limits for each bin.

Fit IV uses the $\Delta\sigma/\Delta\cos\theta$ measurements in two bins at each energy point. The results of this fit should be very consistent with the results given by fit III (although with a larger statistical error, since the sample of events for determination of the asymmetry is smaller in this case), as they are essentially equivalent to measurement of the cross section, and of the asymmetry by the counting method. The results of this fit are given in table 5.6, together with the correlation matrix in table 5.7, and can be seen to be consistent with both the results of fit III, and the MSM predictions shown in figure 5.3.

Parameter	Result from fit IV
$\bar{v}_l^2$	$0.0021 \pm 0.0016(stat) \pm 0.0001(syst)$
$\bar{a}_l^2$	$0.2521 \pm 0.0026(stat) \pm 0.0014(syst)$
Equivalently	
ρ_{eff}	$1.008 \pm 0.012\ (stat + syst)$
$\sin^2\theta_{W_{eff}}$	$0.227^{+0.012}_{-0.008}\ (stat + syst)$
χ^2/N_{dof}	$12.8/(16-2)$
$\bar{v}_l$	$-0.046^{+0.023}_{-0.015}(stat) \pm 0.001(syst)$
$\bar{a}_l$	$-0.5021 \pm 0.0026(stat) \pm 0.0014(syst)$

Table 5.6: Results of 2 parameter fit IV to the measurement of cross section in two bins (one forward, one backward) at 8 energy points. The systematic errors include the contributions due to the uncertainties in M_Z and Γ_Z

Parameter	$\bar{v}_l^2$	$\bar{a}_l^2$
$\bar{v}_l^2$	1	-0.60
$\bar{a}_l^2$	-0.60	1

Table 5.7: Correlation matrix for the 2 parameter fit IV

Fit V uses the $\Delta\sigma/\Delta\cos\theta$ measurements made in 2, 2, 4, 24, 4, 2, 2 and 48 bins, at energy points 1 - 7 in 1990, and the 1991 point respectively. The results of this fit are given in table 5.8, and the correlation matrix is given in table 5.9. The results can be seen to be consistent with those of fits IV and V, and the predictions of the MSM. The statistical uncertainty in $\bar{v}_l^2$ can be seen to be smaller than that given by fit IV - this is because more information is used from each event - the direction of the negative muon is important, rather than just whether it is in the forward or backward region. Of course, if the angular distribution is known (or assumed, as in our case), the best error is obtained by extracting the asymmetry using the maximum likelihood method, but as was mentioned before, the value of a differential cross section fit is that no prior knowledge of the angular distribution is required.

The good value of χ^2 suggests that the angular distribution of the $\mu^+\mu^-$events is consistent with that predicted by the MSM.

Parameter	Result from fit V
$\bar{v}_l^2$	$0.0008 \pm 0.0014(stat) \pm 0.0001(syst)$
$\bar{a}_l^2$	$0.2511 \pm 0.0025(stat) \pm 0.0014(syst)$
Equivalently	
ρ_{eff}	$1.004 \pm 0.012\ (stat + syst)$
$\sin^2\theta_{W eff}$	$0.236^{+0.014}_{-0.009}\ (stat + syst)$
χ^2/N_{dof}	$44.2/(64 - 2)$
$\bar{v}_l$	$-0.028^{+0.028}_{-0.017}(stat) \pm 0.002(syst)$
$\bar{a}_l$	$-0.5010 \pm 0.0025(stat) \pm 0.0014(syst)$

Table 5.8: Results of 2 parameter fit V to the measurement of cross section in 2, 2, 4, 24, 4, 2, 2, and 48 bins at energy points 1-8 respectively

Parameter	$\bar{v}_l^2$	$\bar{a}_l^2$
$\bar{v}_l^2$	1	-0.58
$\bar{a}_l^2$	-0.58	1

Table 5.9: Correlation matrix for the 2 parameter fit V

The $\Delta\sigma/\Delta\cos\theta$ measurements at the eight energy points are shown in figure 5.4, with the theoretical values given by the above results for $\bar{v}_l$ and $\bar{a}_l$ superimposed. Figure 5.5 shows the peak points in more detail.

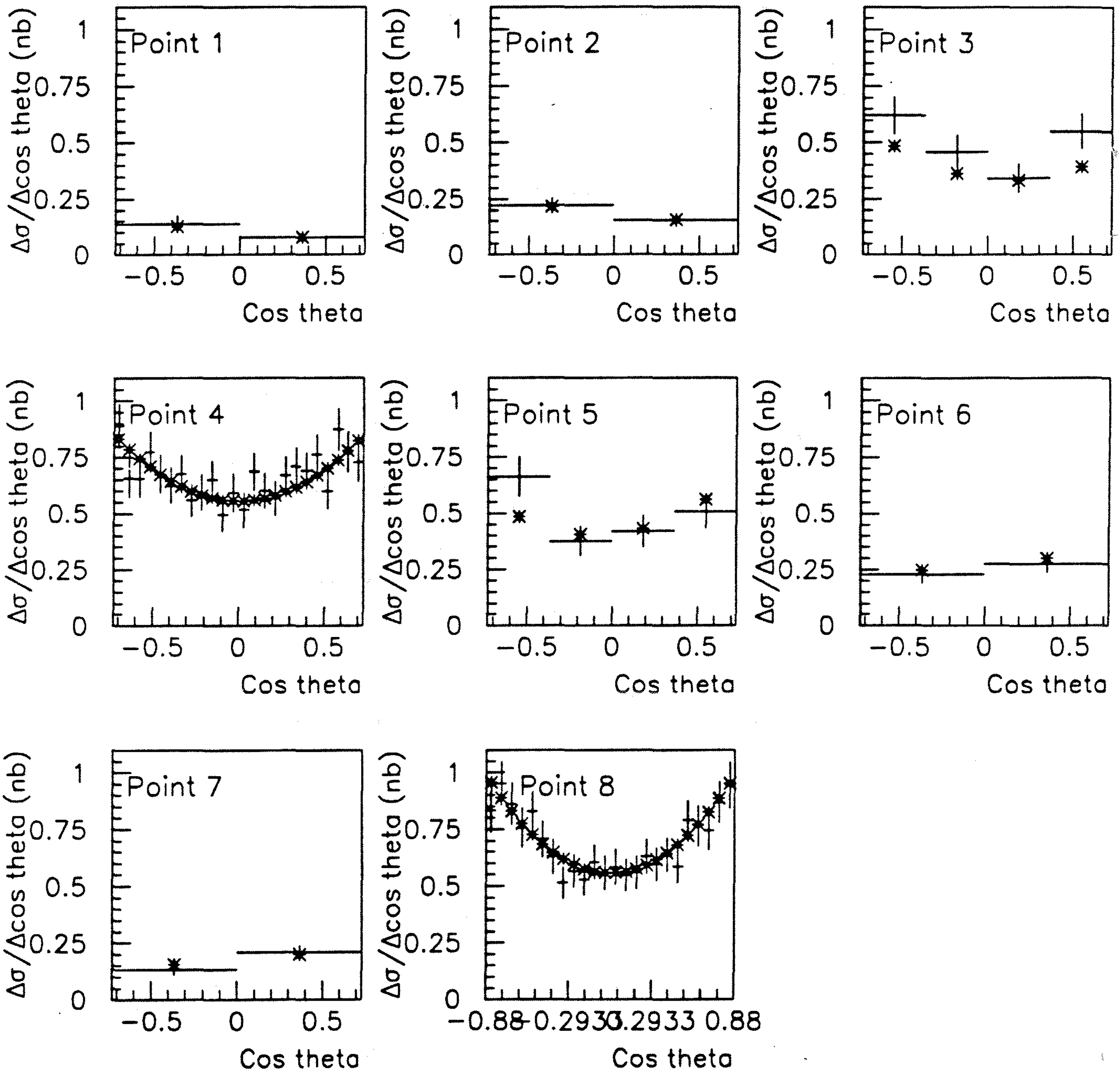

Figure 5.4: $\Delta\sigma/\Delta\cos\theta$ measurements at 8 energy points (error bars), with theoretical predictions given by the results of fit V superimposed (stars)

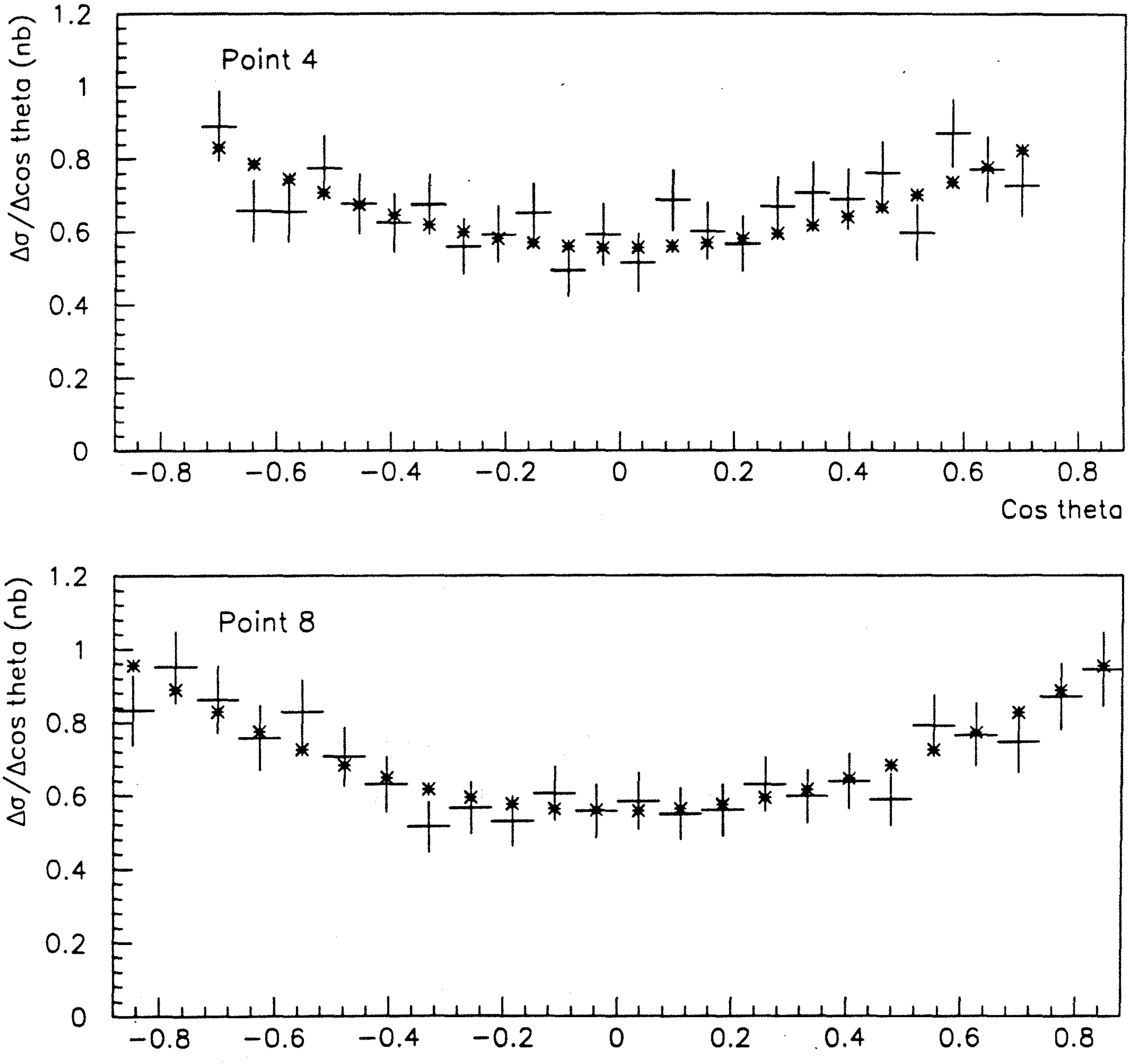

Figure 5.5: $\Delta\sigma/\Delta\cos\theta$ measurements at the two energy points closest to the Z^0peak (error bars), with theoretical predictions given by the results of fit V superimposed (stars)

5.2 Summary of Results

From measurements of the cross section for $Z^0 \rightarrow \mu^+\mu^-$ alone, taking values of M_Z and Γ_Z from the DELPHI hadronic data and assuming lepton universality, a value of the leptonic width Γ_l has been obtained. This value is:

$$\begin{aligned} \Gamma_l &= (84.22 \pm 0.69(stat) \pm 0.40(\sigma syst) \pm 0.36(M_Z, \Gamma_Z) MeV \\ \chi^2/N_{dof} &= 8.8/(8-1) \end{aligned}$$

A combined fit to both the cross sections, and to the forward-backward asymmetries calculated using the maximum likelihood method gave the following result for $\bar{v}_l^2$ and $\bar{a}_l^2$:

$$\begin{aligned} \bar{v}_l^2 &= (0.0017 \pm 0.0009(stat) \pm 0.0001(syst)) \\ \bar{a}_l^2 &= (0.2517 \pm 0.0023(stat) \pm 0.0016(syst)) \\ \chi^2/N_{dof} &= 14.7/(16-2) \end{aligned}$$

From the above results, and using the results of other experiments to determine the sign of $\bar{v}_l$, $\bar{v}_l$ and $\bar{a}_l$ are:

$$\begin{aligned} \bar{v}_l &= (-0.042^{+0.014}_{-0.010}(stat) \pm 0.001(syst)) \\ \bar{a}_l &= (-0.5017 \pm 0.0023(stat) \pm 0.0016(syst)) \end{aligned}$$

$$\begin{aligned} \rho_{eff} &= (1.007 \pm 0.011 \ (stat + syst)) \\ \sin^2\theta_W{}^{eff} &= (0.229 \pm 0.009 \ (stat + syst)) \end{aligned}$$

Measurements of the cross section as a function of $\cos\theta$ were also made, and were observed to agree well with the predicted angular distribution. Values for the leptonic vector and axial vector coupling constants extracted by fitting to these measurements were found to be consistent with those obtained by the above combined fit to cross sections and asymmetries, and the errors on the couplings decreased when the number of $\cos\theta$ bins for the peak points was increased, to use more of the information contained in the events. The statistical errors on the results given by this analysis were larger than those given by the combined fit, as only the angular region used for the cross section analysis could be used. However, when efficiencies can be calculated with confidence over a large angular region, this method will provide a very good test of MSM predictions for the $Z^0 \rightarrow \mu^+ \mu^-$ channel.

All of the above results are consistent with the predictions of the Minimal Standard Model, and assuming that this model is valid, they restrict the mass of the top quark to be between 50 and 310 GeV, at 90% confidence.

References

[1] I.S. Hughes, "Elementary Particles", CUP.
F. Mandl and G. Shaw, "Quantum Field Theory", Wiley.
I.J.R. Aitchison and A.J.G. Hey, "Gauge Theories in Particle Physics", Adam Hilger.
P. Renton, "Electroweak Interactions", CUP.
Proceedings of the School for Young High Energy Physicists, Rutherford Appleton Laboratory, September 5-16 1988, RAL-89-058.

[2] R. Kleiss, "Electroweak Interactions", a series of lectures from the 1990-1991 CERN Academic Training Programme.

[3] C.N. Yang and R.L. Mills, "Conservation of Isotopic Spin and Isotopic Gauge Invariance", Phys. Rev. 96 (1954) 191.

[4] H. Fritzsch and M. Gell-Mann, 1972 Proc. XVI Int. Conf. on High Energy Physics, Chicago (Batavia: FNAL) Vol 2.

[5] S.L. Glashow, "Partial Symmetries of Weak Interactions", Nucl. Phys. 22 (1961) 579.
A. Salam, "Renormalisability of Gauge Theories", Phys. Rev. 127 (1962) 331.
S. Weinberg, "A Model of Leptons", Phys. Rev. Lett. 19 (1967) 1264.

[6] P.W. Higgs, Phys. Lett. 12 (1964) 132, Phys. Rev. Lett. 13 (1964) 508, Phys. Rev. 145 (1966) 1156.
T.W.B. Kibble, Phys. Rev. 155 (1967) 1554.

[7] M. Kobayashi and T. Maskawa, Prog. Theor. Phys 49 (1973) 652.

[8] Peter Ratoff, "Electroweak Couplings and Asymmetries at LEP", Invited talk at XXVIth Rencontre de Moriond, Les Arcs, Savoie, France, March 10-17 1991. OUNP-91-28.

[9] P. Renton, "Constraints on Physics in and Beyond the Minimal Standard Model from LEP Experiments", OUNP-91-30.

[10] H. Burkhardt, J. Steinberger, "Tests of the Electroweak Theory at the Z^0 Resonance", CERN-PPE/91-50 (Vol 1 of Annual review of nucl and particle science)

[11] M. Consoli and W. Hollik, "Electroweak Radiative Corrections for Z^0 Physics", in Volume 1 of "Z Physics at LEP 1", CERN 89-08.

[12] R. Kleiss, "Hard Bremsstrahlung in $e^+e^- \rightarrow \mu^+\mu^-$, matching theory and experiment", in Volume 1 of "Z Physics at LEP 1", CERN 89-08.

[13] R. Kleiss, CERN, Geneva, "Radiative corrections on foot: the minimal standard model and physics at LEP".

[14] R. Marshall, "e^+e^- Annihilation at High Energies", RAL-89-021.

[15] Peter Clarke, "An Introduction to Cross Sections and Asymmetries measurable using Polarised Beams in High Energy e^+e^- Colliders", RAL-90-055.

[16] Bardin et. al., "A Users Guide to ZFITTER: An Analytical Program for Fermion Pair Production in e^+e^- Annihilation."

[17] Stephen Myers, "The LEP Collider, from Design to Approval and Commissioning", CERN 91-08.

[18] LEP Design Reports - "Vol I - The LEP Injector Chain", The LEP injector study group, CERN-LEP/TH/83-29, and "Vol II - The LEP Main Ring", CERN-LEP/84-01.

[19] LEP energy paper and draft

[20] DELPHI Collaboration, "The DELPHI Detector at LEP", CERN/EF 90-5, CERN-PPE/90-128.

[21] DELPHI Technical Proposal, DELPHI 83-66/1, CERN/LEPC/83-3.

[22] T.A.Fearnley and G.Myatt, "Barrel Muon (MUB) Detector", DELPHI 87-98 (Revised).

[23] DELPHI collaboration, "Determination of Z^0resonance parameters and couplings from its hadronic and leptonic decays", Nucl. Phys. B367 (1991) 511.

[24] L. Cerrito, Ph. Charpentier and S.O. Holmgren, "The DELPHI Trigger Control System ZEUS and PANDORA", DELPHI note 8/1/87.

[25] J. Fuster et. al, "The Online Software for the First and Second Level Trigger of DELPHI", DELPHI note in preparation.

[26] M.J. Bates, D. Phil. Thesis, University of Oxford, in preparation.

[27] C. Beeston, "Third Level Trigger for the DELPHI Barrel Muon Chambers", First Year Report, Oxford University.

[28] G. Delavallade, J.P. Vanuxem, "The LTD, a FASTBUS Time Digitizer for LEP Detectors", EP-Electronics Note 85-06.

[29] J. Buytaert et. al., "Fastbus Readout System for the DELPHI Muon Chambers, Time of Flight Counters and End Cap Scintillator Counters, DELPHI 88-92 DAS 90.

[30] C. Vander Velde, "Some Trigger Requirements for the $\mu^+\mu^-$Analysis", DELPHI 87-17 DAS 49.

[31] B. Nijjhar, D.W. Reid, "Trigger Efficiency Calculation for $e^+e^- \rightarrow \mu^+\mu^-$ in the Region $45^\circ < \theta < 135^\circ$", DELPHI 91 - 21, May 1991.

[32] P. Kluit, "Evaluation of the Trigger Efficiency for $Z^0 \rightarrow \mu^+\mu^-$ in 1991", DELPHI 92-34 PHYS 167, March 1992.

[33] J.N. Albert et al., "DELFARM 91 Part 1: Hardware and Software Overview", DELPHI 91-25 PROG 163.

[34] DELPHI Collaboration, "DELPHI Data Analysis Program (DELANA) User's Guide", DELPHI 89-44 PROG 137.

[35] D. Bertrand and L. Pape, "TANAGRA Track Analysis and Graphics Package User's Guide", DELPHI 87-95 PROG 98.

[36] Y. Saquin, "DELPHI DST Content", DELPHI 91-22 PROG 161 (Revised).

[37] J. Wickens, "DELANA Tags for 1991 Data", DELPHI 91-20 PHYS-91 - PROG 160.

[38] P. Dauncey, private communication.

[39] Particle Data Group,"Review of Particle Properties", Phys. Lett. **239B** (1990)

[40] DELPHI collaboration, "A Study of the Reaction $e^+e^- \rightarrow \mu^+\mu^-$around the Z^0pole", Phys. Lett. B. 260 (1991) 240.

[41] N. Crosland, P. Kluit, G. Wilkinson, "EMMASS Muon Identification in DELPHI", DELPHI 92-17 PHYS 157.

[42] Gerald Myatt, private communication.

[43] Trieste and Udine groups, "Measurement of the cosmic ray flux in pit No. 8 of LEP: experimental results", DELPHI 89-62 PHYS 50.

[44] DELPHI note 90-35, Monte Carlo event generator for two- photon physics, unpublished.

[45] F. James, M. Roos, "MINUIT function minimization and error analysis", CERN D506 MINUIT.

[46] Louis Lyons, "Parameter fitting and hypothesis testing and detailed examples of fitting procedures", Oxford University Nuclear Physics Lab. Ref 94/84.

[47] P. Renton, private communication of results for the DALLAS conference.

[48] See for example G. Altarelli, Proceedings of the International Symposium on Lepton and Photon Interactions at High Energies, Stanford University, August 7-12 1989, p.286.

DELPHI Collaboration "A study of the decays of τ leptons produced on the Z^0resonance at LEP", CERN-PPE 92-60, submitted to Z. Phys. C.

[49] OPAL Collaboration, "Measurement of the Z^0line shape parameters and the electroweak couplings of charged leptons", CERN-PPE 91-67, Submitted to Z. Phys. C.

ALEPH Collaboration, "Improved measurements of electroweak parameters from Z^0decays into fermion pairs", CERN PPE 91-105, submitted to Z. Phys. C.

L3 Collaboration, "Measurement of electroweak parameters from hadronic and leptonic decays of the Z^0", L3028, Z. Phys. C51 (1991) 179-203.

[50] F. Sauli, "Principles of Operation of Multiwire Proportional and Drift Chambers", CERN 77-09.

Appendix A

Third Level Trigger Information

This appendix contains brief descriptions of the numbering systems, look up tables, and output data format of the MUB LT3 algorithm.

A.1 Numbering Systems Used Within the Program

- **Room number** - the B side has number 1, the D side has number 2.
- **LTDs** are numbered from 1 to 7.
- **LTD Channels** are numbered from 0 to 47
- **Hit Latches** (6 per LTD channel, from the HLB) are numbered from 1 to 6.
- **Sectors** are numbered from 1 to 24 on both sides of the barrel, a sector being defined as for T2, with 31 chambers per sector - one inner and one outer module, plus the adjacent 5 chambers from 2 peripheral modules. Table A.1 gives the correspondence between the T3 sector number and the sector number of the inner and outer modules.

	Sector of inners and outers	
T3 Sector	B side	D side
1 - 12	13A - 24A	1A - 12A
12 - 24	13C - 24C	1C - 24C

Table A.1: T3 sector numbering

- **Chambers** are numbered from 1 to 700 on both sides of the barrel. Chambers within a sector are numbered consecutively, first the first layer of the inners, then the second, then the third, then the first and second layers of the outer module, and finally the peripheral chambers. The numbering of chambers within a layer is in the **software** convention, except for the peripherals, which are numbered as shown in fig A.1.
- **Signal type** - Anode signals have type 1, Near delay line signals have type 2, Far delay line signals have type 3.

D Side	
T3 Numbers	Chambers
1-7	Peripherals of 24A
8-343	Chambers in sectors 1-12A
344-350	Peripherals of 24C
351-686	Chambers in sectors 1C-12C
687-700	Leg chambers of sector 10
B Side	
T3 Numbers	Chambers
1-7	Peripherals of 12A
8-343	Chambers in sectors 13A-24A
344-350	Peripherals of 12C
351-686	Chambers in sectors 13C-24C
687-700	Leg chambers of sector 15

Table A.2: T3 chamber numbering

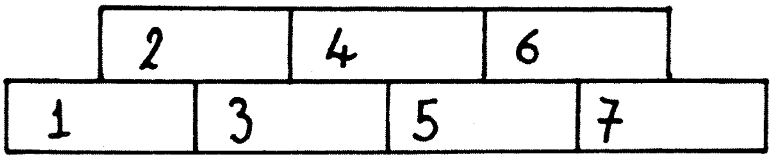

Looking at ‘near’ end of C sectors,
and ‘far’ end of A sectors.

Figure A.1: Numbering of peripheral chambers within a module for T3.

A.2 T3 Look-up-Tables

The MUB T3 algorithm uses the following look up tables, in order of appearance.

- **Demultiplexing table DEMULT[337][8]** - given an LTD number, LTD channel number and hit latch number, the chamber number and signal type are given in $DEMULT[DMLTD[LTD] + CHANNEL][LATCH]$, where $DMLTD[LTD] = (LTD - 1) \times 48$. Bits 0-15 of the word contain the chamber number, bits 16 and 17 contain the signal type.

- **Total delay line time DELTOT[701]** - given a chamber number, DELTOT gives the total delay line time.

- **Wire ϕ position WIRPHI[701]** - given a chamber number, WIRPHI gives the ϕ position of the chamber wire in mrad.

- **Delay line coefficients DELAY[701][3]** - given a chamber number, and the delay line time $t_d = (t_n - t_f)/2$ (in LTD time units), the Z position in local chamber coordinates in cm is given by $DELAY[CHAMBER][1] + DELAY[CHAMBER][2] * t_d/100$.

- **Z position of chamber centre CENPOS[701]** - given a chamber number, CENPOS gives the absolute value of the Z position of the centre of the chamber in cm.

- **Module corresponding to a chamber MODULE[701]** - given a chamber number, MODULE gives the module in which the chamber is situated - 1 for inners, 2 for outers, 3 for peripherals.

- **Sign of Z - ENDS[701]** - given a chamber, ENDS is 1 if the chamber is at the A end (negative Z), 2 if the chamber is at the C end (positive Z) and 3 if the chamber is in one of the modules between the magnet legs, so that it spans Z=0.

- **θ of a hit point THETA[4][3][129]** - given the MODULE and END for a chamber as above, and ZEDPOS, the absolute value of the hit position in Z in cm, in the DELPHI coordinate system (CENPOS-local Z), θ in mrad is given by: $THETA[MODULE][END][ZEDPOS/4 + 1]$.

A.3 T3 data format

Two blocklets are produced in the CPs, one for the B side and one for the D side. The structure of the blocklets is:

1. Word count
2. First identifier = $e18|(room << 16)$
3. Second identifier = $12c|(room << 24)|(algor << 16)$
4. Result word = $(event << 24)|(room << 16)|results$
5. Then two words for each reconstructed hit
6. Last word: word count

Side	T3 sector passing	bit set in result word
B	13A-18A	2
B	19A-24A	0
B	13C-18C	6
B	19C-24C	4
D	1A-6A	2
D	7A-12A	0
D	1C-6C	6
D	7C-12C	4

Table A.3: T3 result word format

algor is an algorithm flag - currently set to 0 (test algorithm).

The format of the first identifier is (E E E S D D T T), where each letter stands for one hexadecimal digit (4 bits).

- TT are the bits for the data type - bits 0 to 3 are 8 for T3 data, bits 4 to 7 are 1 for results data, 8 for start of run data. So TT is 18 for T3 results.
- DD are the bits for the detector identifier, which is 0e for MUB.
- S is the subdetector identifier - this is where the room number is packed.
- EE E is the error field.

So a MUB B side T3 results blocklet should have first identifier 00 01 0e 18.

The result word has event number in bits 24-31, room number in bits 16-23, and bits 0 to 7 are reserved for T3 bits. They are set as for the T1/2 level 1 decision 1 bits, which is the T2 result we decode for use in the T3 algorithm. (In fact although it is possible for there to be two first level and two second level decisions, in practice all the first and second level MUB decisions are identical at present.)

In addition to the result word, there are two words for each hit reconstructed by the third level trigger algorithm. The format of these two words is as follows.

- First word: $(\theta << 16)|\phi$, where the angles are in mrad.
- Second word: (doublet/triplet flag << 16) — Chamber number, where the doublet/triplet flag is 0 for a doublet, 1 for a triplet.

Appendix B

Contents of an Oxford micro-DST for Leptonic Analysis

In the micro-DST, all angles are given in degrees, distances are given in *cm*, energies are given in *GeV*, and momenta are given in *GeV/c*. For each event, the following information is stored.

General event information.

1) Run Number
2) Event number
3) LEP fill number
4) File sequence number
5) Centre of mass energy
6) Magnetic field
7) Number of charged tracks
8) Number of neutral tracks
9) Number of unassociated muon chamber TERs
10) Acolinearity (of two tracks with highest momentum)
11) Word containing B1 trigger bits
12) Word with Pythia trigger bits
13) Spare word
14) Spare word
15) Spare word
16) Number of data blocklets following (= number of charged tracks + number of neutral pas + 1 for extra muon hits

then 1 word per blocklet:
17 - 17+blocklets-1) blocklet identifier and wordcount, packed in 1 word

For the two tracks with greatest momentum:

1) Blocklet identifier - 50 for charged tracks
2) Quality flag - bits flagging useful points of information about the track
bit 1: ID used in track fit
bit 2: TPC used in track fit
bit 3: OD used in track fit
bit 4: FCA used in track fit
bit 5: FCB used in track fit
3) Momentum
4) Theta of the track at the perigee
5) Phi of the track at the perigee
6) Charge
7) $\delta(p)/p$
8) $\delta(\theta)$
9) $\delta(\phi)$
10) track length

11) χ^2 of the fitted track
12) Isolation angle
13) DELANA mass code assigned to the track
14) Impact parameter (signed) - closest approach in $R\phi$
15) Z at closest approach in $R\phi$
16) Time of flight from TOF
17) Error on time of flight
18) Word for outer detector timing information - not yet available
19) Total energy associated with the track by the Combined Calorimetry code
20) Total energy in the electromagnetic calorimeters associated with the track
21) Total energy in the hadron calorimeters associated with the track
22) Number of muon chamber hits associated with the track
23) TOF information (TDC+256*ADC) external
24) TOF extra blocklet word 8 (TDC+256*ADC) internal

Calorimeter information:

1) Blocklet identifier for Combined Calorimetry (CCA)
2) Total associated energy (E) in CCA
3) $\delta(E)$
4) x coordinate of the start of the shower
5) y coordinate of the start of the shower
6) z coordinate of the start of the shower
7) θ direction of the shower
8) ϕ direction of the shower
9) DELANA mass identifier of the shower
10) dummy words to make
11) cca blocklet
12) standard

13) Blocklet id for electromagnetic calorimetry
14) Total associated energy (E) in FEMC and HPC
15) $\delta(E)$
16) x coordinate of the start of the shower
17) y coordinate of the start of the shower
18) z coordinate of the start of the shower
19) θ direction of the shower
20) ϕ direction of the shower
21) DELANA mass identifier of the shower
22) Layer information: number of layers hit
23) Layer pattern - if layer n is hit then bit $n-1$ is set
24) Detector identifier, so that FEMC can be distinguished from HPC

25) Blocklet id for hadron calorimetry
26) Total associated energy (E) in HCAL
27) $\delta(E)$
28) x coordinate of the start of the shower
29) y coordinate of the start of the shower
30) z coordinate of the start of the shower
31) θ direction of the shower
32) ϕ direction of the shower
33) DELANA mass identifier of the shower
34) Layer information: number of layers hit
35) Layer pattern - if layer n is hit then bit $n-1$ is set
36) Detector identifier

Muon chamber information

1) Blocklet identifier = 52
2) Number of layers in muon chambers associated with the track by EMMASS
3) Global chi**2
4) Expected number of missed layers
5) Hit information - information for each TER associated (up to 7)
1) Detector id*10 + submodule id*1000 + and doublet/triplet flag*10000 + whether TER is active(1)/deactive(0) after EMMASS
2) layer chi**2

Other tracks (up to 6)

1) Blocklet identifier = 50
2) Quality word (as for first two tracks)
3) Momentum
4) θ
5) ϕ
6) Charge
7) $\delta(p)/p$ 8) $\delta(\theta)$
9) $delta(phi)$
10) Track length
11) χ^2 of the fitted track
12) Isolation angle
13) DELANA mass code
14) Impact param (signed) - closest approach in rphi.
15) Z at closest approach in $R\phi$
16) Time of flight from TOF, 9999 if there is no information
17) Error on TOF
18) Word for outer detector timing information (not yet available)
19) Total energy associated with the track by the Combined Calorimetry code
20) Total energy in the electromagnetic calorimeters associated with the track
21) Total energy in the hadron calorimeters associated with the track
22) Number of muon chamber hits associated with the track

Neutral tracks - up to 10

1) Blocklet identifier = 51
2) Detector identifier (bitted word - bit 1 CCA, bit 2 HPC/FEMC, bit 3 HCAL)
3) Shower energy in CCA)
4) shower energy in HPC/FEMC)if there is cca data then the emcal/hcal data
5) shower energy in HCAL)will have been used to produce it
6) x)
7) y)these values are for the first shower found on the dst -
8) z)MAKE_DST looks first at CCA, then at HPC/FEMC, then at HCAL
9) θ)
10) ϕ)
11) DELANA mass id

Unassociated muon chamber hits

1) Blocklet identifier = 52
2) Number of TERs for which information is recorded below
3) Total number of TERs that were present

Per TER
a) Submodule identifier

b) R
c) $R\phi$
d) z
e) x
f) y
g) θ
h) ϕ
i) Doublet/triplet flag

Simulation information (if any)

1) Blocklet identifier = 53
2) Number of charged particles for which information is recorded below (max 10)
3) Total number of charged particles that were present
4) Number of neutral particles for which information is recorded below (max 10)
5) Total number of neutral particles that were present

For each simulated particle - charged particles first then neutrals
1) Momentum
2) Energy
3) θ at production
4) ϕ at production
5) Charge
6) Mass identifier
7) Number of generations
8) Number of generations recorded (max 10, if word 7 ¿ 10 then the 10 earliest generations will be recorded)
9)....18) Mass ids of particles. The first one is the initial state particle, the last one will usually be the final state particle.

Information on the $l\bar{l}$ system - zero if not available
1) PX
2) PY
3) PZ
4) E
5) P
6) $\cos\theta$
7) PHI
8) Mass code 1
9) Mass code 2

Information on the VD refit

1) Blocklet identifier = 54
2) Number of charged tracks for which refit has been attempted (NCHVD)
3) Beamspot quality - 0 is good

For each track:
4 - 4+NCHVD-1) Number of vertex detector hits associated with the track

For each track, the track perigee parameters before and after the refit, with respect to the beamspot.
a) Signed impact parameter before refit
b) z before refit
c) θ before refit
d) ϕ before refit

e) $1/p$ (signed) before refit

a) Signed impact parameter after refit
b) z after refit
c) *theta* after refit
d) *phi* after refit
e) $1/p$ (signed) after refit

Appendix C

Monte Carlo Tuning Factors

The tuning factors to be applied to the Monte carlo were obtained by comparing detector response in the Monte Carlo $\mu^+\mu^-$samples with that for samples of $\mu^+\mu^-$events selectedfrom the data using hard identification criteria. Monte Carlo data was generated with two different representations of the detector status, one corresponding to the period before the HPC voltage drop and one to data taken after this.

The followng tuning factors were applied to the energy associated with each charged track in the calorimeters, so that $E_{corr} = T_f \times E_{gen}$, where E_{corr} is the corrected energy, T_f is the tuning factor and E_{gen} is the generated energy.

Detector	1990	1991
HPC	1.5	1.5
FEMC	1.0	1.0
Barrel HCAL	0.55	1.1
Forward HCAL	0.75	1.0

Table C.1: Monte Carlo tuning factors for associated energy in the calorimeters

Each muon chamber hit associated with a track in the Monte Carlo was kept with a probability of 0.983 for the barrel muon chambers, and 0.913 for the forward muon chambers [41].

Appendix D

Glossary

BCO - Beam CrossOver
Blocklet - a piece of DELPHI data, beginning and ending with a word count, and having two words set aside for identifiers and error flags
CEB - Crate Event Buffer
CP - Crate Processor
C1-C5 - cuts made on charged tracks in the $\mu^+\mu^-$ analysis
DELANA - the DELPHI software for event reconstruction
DELFARM - the cluster of workstations where the DELPHI data is processed
DELGRA - the DELPHI graphics package
DELPHI - the DEtector with Lepton, Photon and Hadron Identification
DST - Data Summary Tape
E_{cm} - centre of mass energy
E_{em} - the amount of energy in the electromagnetic calorimeters associated with a track
E_h - the amount of energy in the hadron calorimeters associated with a track
E'_h - E_h with its angular dependence removed
with a track
FCA - Forward Chamber A
FCB - Froward Chamber B
FEMC - Forward Electromagnetic Calorimeter
FIP - Fastbus Intersegment Processor
HCAL - Hadron Calorimeter
HLB - Hit Latch Buffer
HOF - Forward Hodoscope (scintillators)
HPC - High density Projection Chamber - the barrel electromagnetic calorimeter
IBA - Improved Born Approximation
ID - Inner Detector
LEP - the Large Electron Positron collider
LES - Local Event Supervisor
LTD - LEP Time Digitiser
LT3P - Local Third level trigger process
MIP - Minimum Ionising Particle
MSM - Minimal Standard Model
MUB - Barrel Muon Chambers
MUF - Forward Muon Chambers
MU1-MU3 - muon identification criteria for the $\mu^+\mu^-$ analysis
MWPC - MultiWire Proportional Chamber
N_{mux} - the number of hits in the muon chambers associated with a track
OD - Outer Detector
PS - Proton Synchrotron
PXDST - software which strips TANAGRA data down to DST data
RF - Radio Frequency
RICH - Ring Imaging CHerenkov detector
SAT - Small Angle Tagger - the luminosity monitor

SPS - Super Proton Synchrotron
TANAGRA - data structure for DELPHI data, containing information from all levels of the event reconstruction (TD to TV)
TB - Track bundle
TD - Track Data
TE - Track Element
TK - TracK
TV - Track Vertex
TOF - Time Of Flight scintillators
TPC - Time Projection Chamber
T1-4 - the first, second, third and fourth level triggers
VD - Vertex Detector